UC Berkeley
UC Berkeley Electronic Theses and Dissertations

Title

Regulatory Features of Substrate Degradation by the 26S Proteasome

Permalink

https://escholarship.org/uc/item/3vh450nj

Author

Greene, Eric Raymond

Publication Date

2020

Peer reviewed|Thesis/dissertation

Regulatory Features of Substrate Degradation by the 26S Proteasome

By

Eric R Greene

A dissertation submitted in partial satisfaction

of the requirements for the degree of

Doctor of Philosophy

in

Molecular & Cell Biology

in the

Graduate Division

of the

University of California, Berkeley

Committee in charge:
Professor Andreas Martin, Chair
Professor Jamie Cate
Professor Eva Nogales
Professor Ahmet Yildiz

Summer 2020

Abstract

Regulatory Features of Substrate Degradation by the 26S Proteasome

by

Eric R Greene

Doctor of Philosophy in Molecular & Cell Biology

University of California, Berkeley

Professor Andreas Martin, Chair

The 26S proteasome is essential for proteostasis and the regulation of vital processes through ATP-dependent degradation of ubiquitinated substrates. Proteasome substrate selection is paramount to maintaining the proteome. My graduate work has focused on the interplay between conformational properties of the proteasome and its substrates to coordinate commitment to the degradative process. To accomplish the multi-step degradation process, the proteasome's regulatory particle, consisting of lid and base subcomplexes, undergoes major conformational changes whose molecular determinants and regulation is unknown. Investigating the *S. cerevisiae* proteasome through *in vitro* biochemical and structural studies, I found that peripheral interactions between the lid subunit Rpn5 and the base AAA+-ATPase ring are important for stabilizing the substrate-engagement-competent state and coordinating the conformational switch to processing states upon substrate engagement. Disrupting these interactions perturbs the conformational equilibrium and interferes with degradation initiation, while later processing steps remain unaffected. Similar defects in early degradation steps are observed when eliminating hydrolysis in the ATPase subunit Rpt6, whose nucleotide state seems to control proteasome conformational transitions. We found that perturbed proteasome conformational distributions can make substrate engagement the rate limiting step in a substrate dependent manner. These results provide important insight into interaction networks that coordinate conformational changes with various stages of degradation, and how modulators of conformational equilibria may influence substrate turnover.

In addition to ubiquitin modification for substrate binding to the 26S proteasome, proteasome substrates require an initiation region of greater than 10 amino acids for engagement by the 19S AAA+ motor. While many substrates in the cell contain disordered regions, many substrates lack this requirement. The Marqusee lab found that ubiquitination of lysine residues within structured domains can confer a dramatic destabilization of the substrate proteins that is both substrate specific and dependent on the site of ubiquitination. In collaboration, we provided the first *in vitro* experimental evidence that ubiquitin mediated destabilization of substrates lacking disordered regions was sufficient to induce an unstructured region for proteasomal engagement. Degradation rates of these substrates were also sensitive to our previously characterized mutations to Rpn5 and Rpt6 in the proteasome, thus providing evidence that engagement, rather than mechanical unfolding, is the rate limiting step for degradation of these substrates that rely on spontaneous

partial unfolding to reveal unstructured initiation regions. All ubiquitin-mediated effects on substrate stability could further be modulated by deubiquitination, binding to ligand, or stabilizing mutations, leading us to conclude that substrate energetics and their modulation by ubiquitination is paramount to both substrate selection, and the rate of degradation by the proteasome.

Substrate thermodynamics play an important role in influencing degradation rate and efficiency, yet there is a dearth of evidence regarding which thermodynamic, topological, or kinetic factors contribute most to this defining role. I thus present an experimental approach based on single-molecule FRET and the determination of proteasome degradation rates that are comparable across various substrates to assess the detailed biophysical principles underlying proteasomal substrate processing. In principle, this approach is generalizable to multitudes of protein domains. Additionally, evidence of potential intermediary substrate protein structures is presented. Taken together, the studies described herein provide evidence for multiple different means of regulating the ubiquitin-proteasome system.

Table of Contents

Acknowledgements

Firstly, I want to thank Andreas Martin for allowing me to independently pursue many experimental lines of inquiry, for mentoring me through these projects, and for helping develop full mechanistic theories that explain *all* of the data. I would also like to thank my thesis committee; Professors Jaime Cate, Eva Nogales, and Ahmet Yildiz, whose input and expertise helped me overcome multiple experimental challenges.

I would like to thank all members of the Martin for guidance and assistance over the years. From helpful discussions about science to life, from help with experiments to reading drafts of everything, from literally laying the groundwork for any of these studies to have been accomplished to playing my jam in lab, from keeping all of the equipment running and keeping our data safe to critical discussions of Week 14 running back ranking; for each member of the Martin lab, past and present, for actions large and small, thank you.

I would like to thank Susan Marqusee and her lab members for introducing me to various research conferences, mega-crossword puzzles, celebrating my birthday in Tahoe, and for help using equipment whenever I was in a pinch. I am also grateful for conversations with Professor Michael Woodside regarding career pathways in academia as well as the course MCB295.

I am lucky to have been in the MCB program and want to thank the Graduate Affairs Office for always making sure we were paid on time and that all of the events that shape the culture of the MCB department could happen. I am grateful to the past and current organizers of Structure Supergroup and QB3 Postdoc Seminars for offering great platforms for practicing research presentation. Additionally, I would like to thank the doctors and professionals at the University Health Services that have helped me physically and mentally.

To my classmates, I want to thank you for being advocates, adventure buddies, and overall amazing people. I am very excited and hopeful to see our paths cross again.

I want to extend a special thanks to my family for their continued support. To my sister, Michelle, for being a role model and the first in our family to endure and succeed through a PhD and to pass on that wisdom. To my parents, for always doing every possible thing that they could to facilitate me following my passion, thank you. To my uncle and late grandfather, for helping encourage me and helping purchase my computer that got me through all 6 years.

Lastly, easily the best thing about graduate school was meeting you, Emma Carroll. There are not words, nor enough pages to cover everything that deserves to be said. Suffice it to say here, thank you for literally bringing color back into my life.

Chapter 1: An introduction to the 26S proteasome within the ubiquitin-proteasome system

A portion of the work presented in this chapter has been previously published as part of the following paper: Greene, E.R., Dong, K.C., Martin, A. Understanding the 26S proteasome molecular machine from a structural and conformational dynamics perspective. Curr. Opin. Struct. Biol. 2020.

Proteins are encoded products of the genome and are responsible for carrying out the majority of cellular functions in all domains of life. These include catalyzing chemical reactions, cell replication, and responding to a cell's environment. Proteins fold into complex geometric shapes encoded by their amino acid sequence to carry out their function. The thousands of different protein products, their concentration, and composition within space and time collectively constitute the proteome. Paramount to survival is maintenance of proteome homeostasis (proteostasis), which requires ensuring proper protein folding through the use of a chaperone network and the selective degradation of terminally-misfolded proteins whose existence is toxic to cells (Balchin et al., 2016; Sala et al., 2017). In addition to misfolded protein clearance, key signaling proteins that mediate vital cellular processes, including transcription and cell division, require degradation to regulate duration of a given cellular signal (Chao, 2014; Finley and Prado, 2020; Maki et al., 1996; Palombella et al., 1994). In some cases, cell differentiation requires the remodeling of the whole proteome, as evidenced by erythrocyte maturation into red blood cells that necessitates regulated protein degradation in order to establish a proteome of majority hemoglobin (Nguyen et al., 2017). Proteotoxic clearance, signal regulation, and cell differentiation are all essential processes to sustain multicellular life and dependent on the ubiquitin-proteasome system (UPS). In humans, malfunctioning of regulated protein turnover is the basis of neurodegenerative diseases characterized by accumulation of toxic misfolded proteins, and misregulation of the UPS plays a role in many cancers (Sala et al., 2017).

The ubiquitin-proteasome system

Selective protein degradation mechanisms appear in all domains of life and are highly conserved. In eukaryotes, this process is primarily carried out through the UPS (Figure 1.1A)(Goldberg, 2003; Opoku-Nsiah and Gestwicki, 2018). The first step of UPS-catalyzed protein degradation is the posttranslational attachment of the small, 8.5 kDa protein, ubiquitin, to a substrate protein. Ubiquitin's C-terminal carboxylic acid is covalently ligated by an enzymatic cascade to the epsilon amine group of substrate lysine residues (Figure 1.1B). The chemical energy derived from hydrolysis of ATP to AMP and pyrophosphate is required to activate ubiquitin's C-terminus through thioester-bond formation with the first enzyme of the cascade, E1. Subsequently, an E1 enzyme transfers the activated ubiquitin to E2 enzymes through a transthioesterification reaction. Ubiquitin-activated E2's can transfer their ubiquitin directly to substrates by forming a ternary complex with adaptor E3 ubiquitin ligases of the Really Interesting New Gene (RING) family and the substrate protein. Alternatively, E2's can pass ubiquitin through a second transthioesterification reaction directly to the Homology to E6AP C Terminus (HECT) or RING-between-RING (RBR) E3 ligase families.

HECT and RBR E3 ligases activated with ubiquitin can recognize substrate proteins and subsequently direct ubiquitin to substrate lysines (Figure 1B)(Chaugule and Walden, 2016; Komander and Rape, 2012; Rennie et al., 2020).
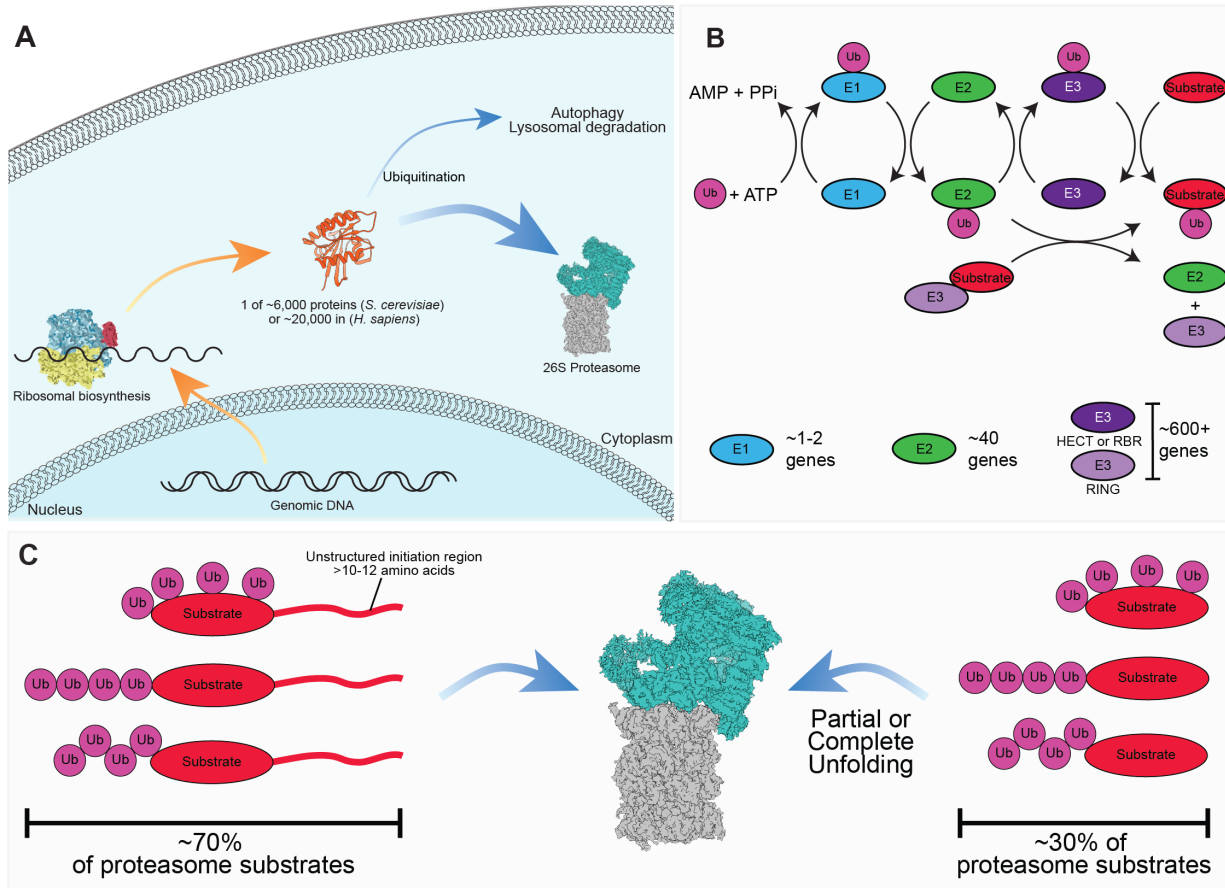

Figure 1.1: The pathway of substrate degradation by the ubiquitin-proteasome system. (A) Biosynthesis and degradation pathway for protein constitutes of the intracellular proteome. (B) Cartoon depiction of the ubiquitination enzymatic cascade (top) showing the activation of ubiquitin (magenta) by E1 (blue) using ATP hydrolysis chemical energy, followed by transfer to the E2 enzymes (green). Lastly, the E2 can directly transfer the ubiquitin to substrate (red) lysines through ternary complex formation with substrate recognizing RING class E3s (light purple), or, the E2 can transfer ubiquitin to HECT or RBR class E3s (dark purple) who subsequently bind to and transfer ubiquitin to substrate proteins. Below, the relative number of unique enzymes that constitute each of the three classes of ubiquitination enzymes. (C) Cartoon depiction of substrate requirements for successful degradation by the 26S proteasome and their relative intracellular population. Left, proteasome substrates that contain, or are predicted to contain, an unstructured region of sufficient length for proteasome engagement as well as the requisite ubiquitin modification of at least four ubiquitins that can be of differing topology. Right, proteasome substrates lacking a sufficient unstructured initiation region and whose successful clearance is dependent on partial or complete unfolding upstream of proteasome engagement.

Besides the attachment to a substrate, ubiquitin can be ligated to itself through any of its seven lysine residues, forming ubiquitin chains of different length and topology. Within a ubiquitin chain, the ubiquitin that has a free C-terminus or whose C-terminus is ligated to a substrate lysine residue is labeled the 'proximal' ubiquitin or proximal end, whereas the last ubiquitin moiety on the other side, with none of its lysines modified, is labeled the 'distal' ubiquitin or distal end. Ubiquitin chains can also possess branch points, making ubiquitination one of the most diverse posttranslational modifications (PTMs)(Komander and Rape, 2012). Though monoubiquitination of substrate proteins can be a sufficient molecular signal to condemn some proteins for degradation by the

2

proteasome (Livneh et al., 2017), most condemned substrates appear modified with ubiquitin chains of at least four ubiquitins (Komander and Rape, 2012). Additionally, different ubiquitin linkage types are associated with greater degradability by the proteasome, leading to the hypothesis that these linkage types constitute a "ubiquitin code". While current understanding of the ubiquitin code is incomplete (Martinez-Fonts et al., 2020), some general rules have been outlined. Chains containing ubiquitin attached to ubiquitin at lysine 48 or lysine 11 (K48 and K11 respectively) are canonically associated with degradation by the proteasome, while K63-linked ubiquitin chains are typically associated with non-degradative regulatory functions (Oh et al., 2018). Additionally, branched chains containing a K11 and K48 linkage on the proximal ubiquitin are strongly associated with degradation (Yau et al., 2017).

Which proteins are ubiquitinated is largely defined by binding specificity and expression of specific E3 enzymes. Indeed, E3s vastly outnumber both E1 and E2 enzymes in order to maintain this specificity (Chaugule and Walden, 2016; Zhou et al., 2018). Moreover, some E3's can harbor high promiscuity and are expressed during times of proteome remodeling or stress (Fang et al., 2014; Nguyen et al., 2017). In addition to an appropriate ubiquitin chain for targeting to proteasomal ubiquitin receptors, substrates require an unstructured initiation region for commitment to degradation (Tomita and Matouschek, 2019). This unstructured region must be at least 10-12 residues in length for efficient engagement by the proteasome (Prakash et al., 2004; Takeuchi et al., 2007; Tomita and Matouschek, 2019; Yu and Matouschek, 2017). Most known proteasome substrates contain an acceptable unstructured region (Hagai et al., 2011). However, a substantial fraction of known proteasome clients lack this region and must access a partially, or fully, unfolded state through alternative means (Hagai et al., 2011), which could include preprocessing unfoldases (Godderz et al., 2015; Olszewski et al., 2019; Tsuchiya et al., 2017) or the transient spontaneous full or partial unfolding due to destabilizing effects of attached ubiquitin modifications (Gavrilov et al., 2015; Hagai and Levy, 2010; Hagai et al., 2011). If these substrate prerequisites are met, degradation by the proteasome proceeds as the final step of the UPS.

Architecture of the 26S Proteasome

The 26S proteasome is a 2.5 MDa molecular machine that is the executor of the UPS, responsible for processing hundreds to thousands of chemically distinct protein substrates in a highly selective manner. Central to this high promiscuity and high selectivity of substrate degradation is the overall architecture of the proteasome. The minimal assembly of the 26S proteasome is comprised of 33 distinct subunits. The holoenzyme can be biochemically divided into the 20S core particle (14 distinct subunits) and 19S regulatory particle (19 distinct subunits). The 19S regulatory particle can be further separated into the base subcomplex and the lid subcomplex (Figure 2A), with one of the ubiquitin receptors, Rpn10, bridging and stabilizing the two (Buel et al., 2020; Glickman et al., 1998a). The 26S holoenzyme is capable of recognizing and engaging condemned, ubiquitinated substrates, subsequently deubiquitinating them for ubiquitin recycling in the cell, unfolding structured domains, and translocating of the unstructured polypeptide into a sequestered chamber for proteolysis.
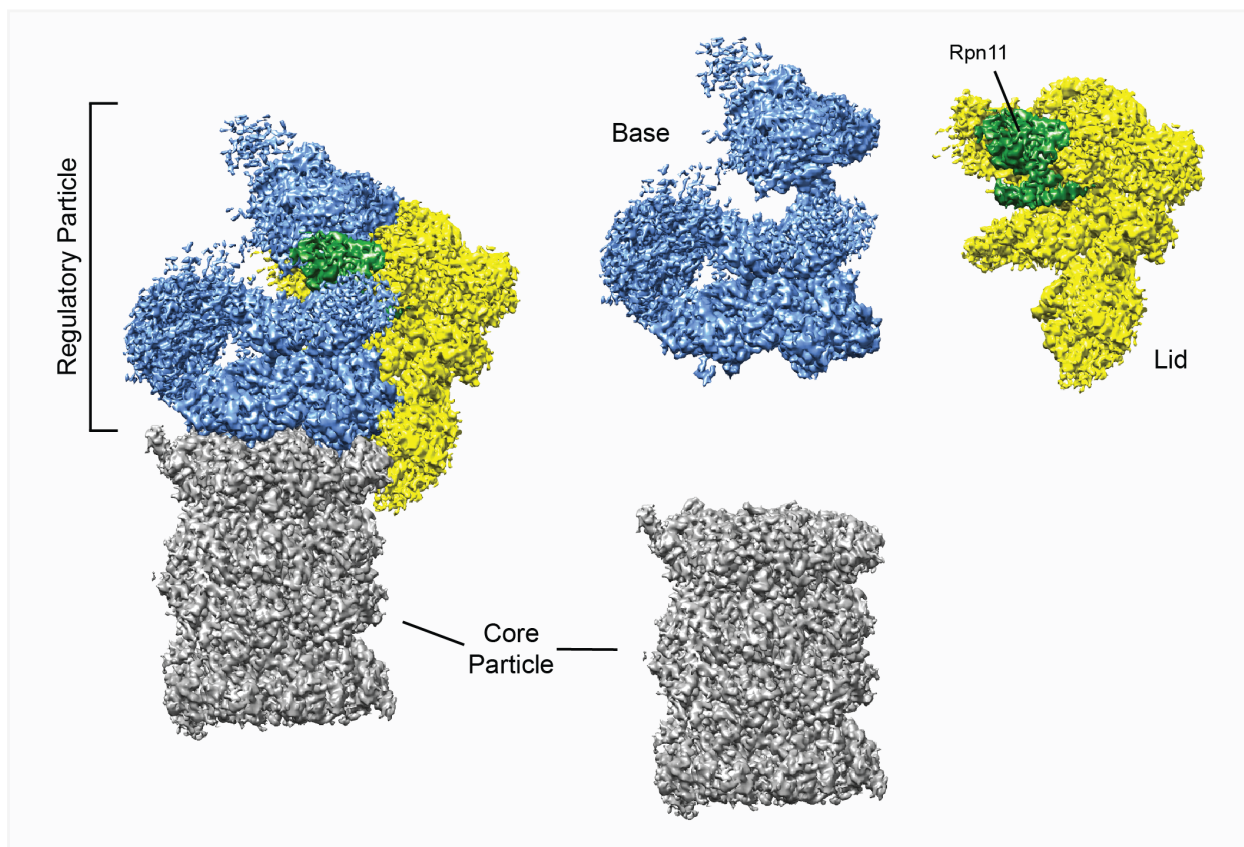
Figure 1.2: Overall architecture of the 26S proteasome. High-resolution 3D cryo-EM reconstruction of the *S. cerevisiae* 26S proteasome (EMD: 3534) with the core particle shown in gray and the regulatory particle in multi-color. The base is colored in blue, lid in yellow, and Rpn11, the essential deubiquitinase in the lid, shown in green.

The proteolytic activity responsible for hydrolysis of condemned substrates is harbored within the central cavity of the 20S core particle. The core particle contains 14 distinct subunits in two copies each that are divided into four stacked heptameric rings (in order, α1-7, β1-7, β1-7, α1-7) (Groll et al., 1997). The subunits β1, β2, and β5 harbor proteolytic activity with caspase-like, trypsin-like, and chymotrypsin-like cleavage specificities, respectively (Orlowski and Wilk, 2000). The final maturation step of 20S assembly requires active proteolytic sites at these subunits to cleave propeptide sequences and degrade assembly chaperones to thus ensure proper functioning (Murata et al., 2009; Saeki and Tanaka, 2012). The N-termini of the alpha subunits create a dense meshwork (the "α-gate") at the apical faces of the 20S core particle. These N-termini can be retracted, leading to gate opening, when regulatory proteins (including the regulatory particle) dock into hydrophobic pockets at the inter-alpha subunit interface (Groll et al., 1997, 2000; Opoku-Nsiah and Gestwicki, 2018; Rabl et al., 2008; Tian et al., 2011; Toste Rêgo and da Fonseca, 2019). Thus, the α-gate constitutes a regulated gateway for substrate entry into the 20S core particle for proteolysis. The 19S regulatory particle binds to one, or both, α-rings of the 20S core and is responsible for ubiquitinated substrate recognition, engagement, unfolding, deubiquitination, and translocation into the central cavity of the core particle.

The base subcomplex of the regulatory particle is composed of nine distinct subunits. At its center are six distinct AAA+ (ATPases associated with cellular activities) ATPase subunits that form a heterohexamer in the order Rpt1, Rpt2, Rpt6, Rpt3, Rpt4, and Rpt5 (Erales et al., 2012; Tomko and

Hochstrasser, 2011; Tomko et al., 2010). Their ATPase domains are highly conserved across all domains of life (Erzberger and Berger, 2006; Frickey and Lupas, 2004; Iyer et al., 2004; Volker and Lupas, 2002) and convert the chemical energy of ATP hydrolysis into mechanical force to unfold and propel protein substrates through a central pore of the hexameric ring. The heterohexameric ATPase is arranged as a trimer of dimers (Rpt1 & Rpt2; Rpt6 & Rpt3; Rpt4 & Rpt5) formed through the interaction of N-terminal coiled coil regions of each Rpt. Beyond its architectural role, the Rpt4 and Rpt5 coiled coil is also proposed to have a ubiquitin binding function from recent cryo-electron microscopy (cryo-EM) structures of substrate bound proteasome (Dong et al., 2019). In between the N-terminal coiled coil and the ATPase domain is an N-terminal globular domain with Oligonucleotide/Oligosaccharide Binding (OB) fold that in the hexamer forms an N-terminal domain ring (N-ring) above the ATPase ring. Pore loops project from every ATPase domain into the central channel, and conserved tyrosine residues in the so-called pore-1 loops interact with the polypeptide backbone of engaged substrates. ATP-hydrolysis-coupled conformational changes of ATPase domains transmit through to the pore loops and allow force generation for substrate translocation and unfolding. The C-terminal peptides of Rpt1, 2, 3, 5, and 6 harbor a conserved HbYX (Hydrophobic-Tyrosine-X) motif for docking to the alpha ring of the 20S core and triggering gate opening. The C-terminal regions of the ATPase domains are also the binding sites for specific chaperones (Nas2, Rpn14, Hsm3, and Nas6) that ensure proper assembly of subunits during base assembly and whose eviction is required for docking to the 20S core particle during 26S holoenzyme formation (Beckwith et al., 2013; Funakoshi et al., 2009). Nas6, which copurifies with both the base subcomplex (Beckwith et al., 2013) and the regulatory particle (Lu et al., 2017) is the final chaperone to be evicted upon assembly (Nemec et al., 2019). In addition to the ATPases Rpt1-6, the base subcomplex contains the non-ATPase subunits Rpn1, Rpn2, and Rpn13. While Rpn2 plays primarily structural roles, Rpn1 and Rpn13 serve as ubiquitin receptors for substrate recruitment to the proteasome (Husnjak et al., 2008; Shi et al., 2016).

The lid subcomplex is comprised of nine distinct subunits; Rpn3, Rpn5, Rpn6, Rpn7, Rpn8, Rpn9, Rpn11, Rpn12, and Sem1. Rpn11 is the essential deubiquitinase, responsible for the *en bloc* removal of ubiquitin modifications from committed substrates (Verma et al., 2002; Yao and Cohen, 2002). Rpn11 is located above the entrance to the central channel of the base ATPase ring, such that translocation of a substrate polypeptide guides attached ubiquitin moieties into Rpn11's catalytic groove. This translocation-coupled ubiquitin binding promotes a conformational switch of Rpn11's Insert-1 region from an inhibitory loop (Worden et al., 2014) to a hairpin that stabilizes ubiquitin in the active site and thus aides in deubiquitination (Worden et al., 2017). The remaining lid subunits are non-enzymatic and serve architectural functions, making extensive contacts with the base and also contacting the core particle. Assembly of lid subunits is directed through C-terminal helices that form an intricate helical bundle (Estrin et al., 2013) whose maturation is completed with Rpn12 incorporation (Tomko Jr. and Hochstrasser, 2011; Tomko et al., 2015). Free, unincorporated lid subcomplex, is characterized by an autoinhibited Rpn11 that undergoes a dramatic conformational change upon incorporation in the 26S proteasome to allow exposure of Rpn11's active-site (Dambacher et al., 2016). Rpn5 is responsible for shielding Rpn11's active in the isolated lid (Dambacher et al., 2016) and is also responsible for the final eviction of Nas6 upon assembly of 26S proteasome (Nemec et al., 2019). The ubiquitin receptor Rpn10 bridges the lid and base subcomplexes, making contacts with the Rpt4 and Rpt5 coiled coil in the base and Rpn9, Rpn8, and Rpn11 in the lid, and therefore stabilizes the 19S regulatory particle as well as the 26S proteasome as a whole (Lander et al., 2012).

Mechanism of the 26S Proteasome Mediated Substrate Degradation

The degradation process follows a complex kinetic mechanism with many intermediate steps. Ubiquitin chains appended to a substrate must first be recognized by ubiquitin receptors on the proteasome. The proteasome's ubiquitin receptors Rpn1, Rpn10, and Rpn13 occupy key peripheral positions around the regulatory particle to facilitate interaction and high local concentration around the central pore (Figure 1.3A). Additionally, shuttling factors have been described to bind condemned substrates and mediate delivery to the 26S proteasome (Chen and Madura, 2002; Elsasser et al., 2004; Kim et al., 2004; Schauber et al., 1998). The obligate unstructured region of the substrate then must passively diffuse into the central pore of the AAA+ ATPase to be engaged by the base pore loops. Substrate engagement triggers a global conformational switching of the regulatory particle (Bard et al., 2019) from a predominant ground state conformation (Beck et al., 2012; Chen et al., 2016; Ding et al., 2017, 2019; Eisele et al., 2018; Da Fonseca et al., 2012; Greene et al., 2019; Haselbach et al., 2017; Huang et al., 2016; Lander et al., 2012; Lasker et al., 2012; Luan et al., 2016; Schweitzer et al., 2016; Śledź et al., 2013; Unverdorben et al., 2014; Wehmer et al., 2017; Zhu et al., 2018) into a set of substrate-bound conformations (Dong et al., 2019; De la Peña et al., 2018; Matyskiela et al., 2013). In substrate-bound conformations, Rpn11's active site is optimally positioned directly above the central pore of the base ATPase ring to remove ubiquitin chains from translocating substrates. Unfolding of structured domains presents a common rate-limiting step for the degradation of many model substrates (Bard et al., 2019; Carroll et al., 2020; Greene et al., 2019), and this rate is dependent on substrate topology and thermodynamic stability, in particular the local stability of secondary structures adjacent to the flexible initiation region where the proteasome starts pulling (Cordova et al., 2014; Kenniston et al., 2004; Koodithangal et al., 2009; Lee et al., 2001; Mallik and Kundu, 2018; Martin et al., 2008; Nager et al., 2011; Sen et al., 2013). Translocation of the fully unstructured substrate polypeptide into the core particle and proteolysis in the internal chamber of the 20S core constitute the common final steps of degradation.
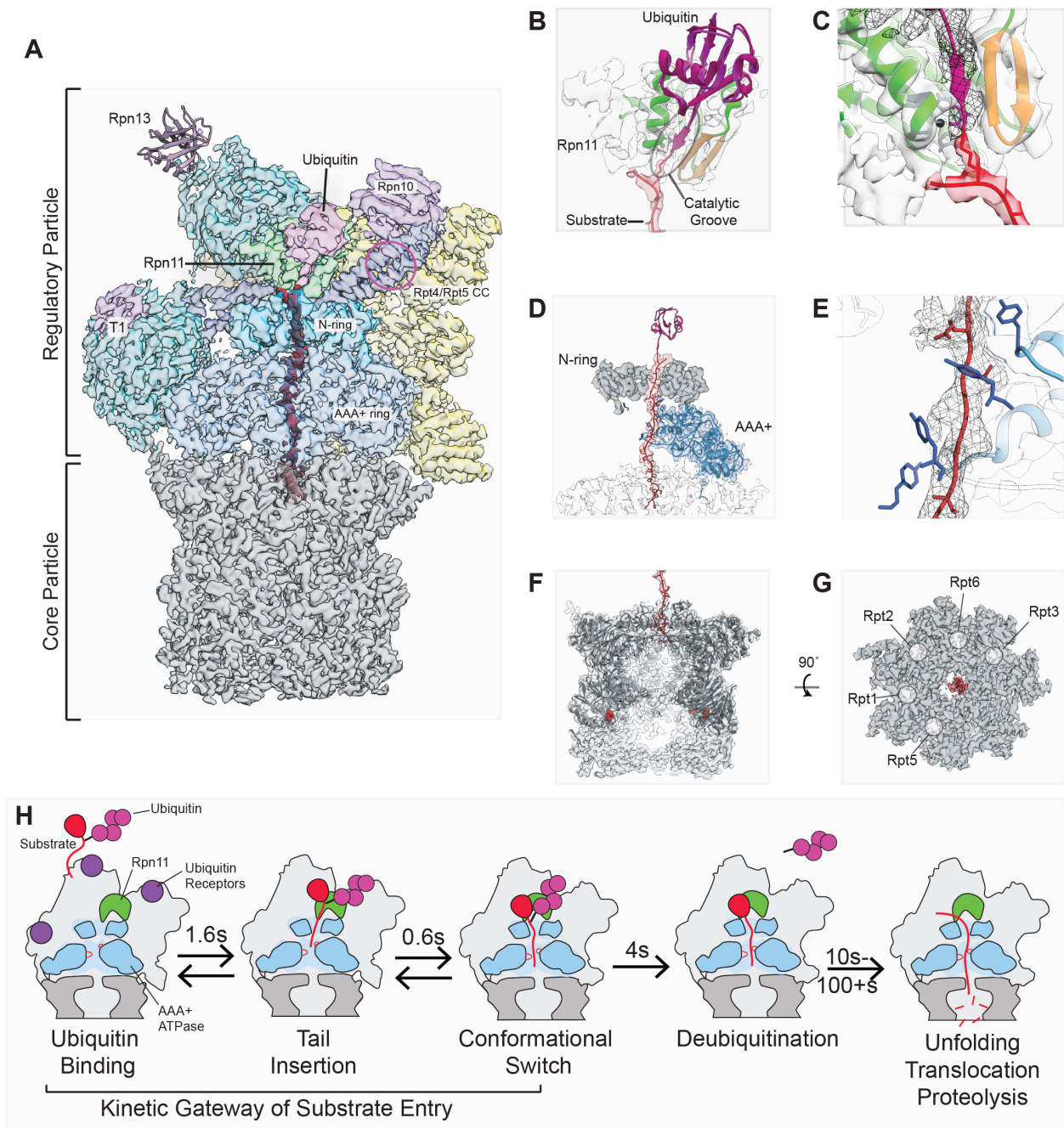
Figure 1.3: Mechanism of substrate degradation by the 26S proteasome. (A) Architecture of the substrate-bound proteasome (EMD: 9045), displaying the core particle in gray and the regulatory particle in multi-color, with substrate in red and ubiquitin in magenta. Ubiquitin receptors Rpn13 (PDB: 6FVW), Rpn10, and the T1 site on Rpn1, as well as a potential binding site on the Rpt4/Rpt5 coiled-coil (CC) are presented in purple. The hexameric AAA+ ATPase motor consists of three N-terminal coiled-coils (navy blue) and a ring formed by the size N-domains (N-ring, sky blue) atop the ring of the AAA+ domains (cornflower blue). Rpn1 and Rpn2 are presented in dark cyan, and the Rpn11 deubiquitinase in green. Lid subunits are shown in yellow. (B) X-ray structure of Rpn11-bound ubiquitin (PDB: 5U4P; Rpn11 in green, Ins-1 loop in orange, active-site residues and catalytic zinc in dark gray, ubiquitin in magenta) docked into the cryo-EM density of substrate-bound proteasome (EMD:9045; regulatory particle in gray, substrate in red) and overlaid with the atomic model for the substrate-bound proteasome (PDB: 6EF3; ubiquitin in violet red, substrate in red). The catalytic groove formed by active Rpn11 is highlighted. (C) Zoomed-in representation of (B), omitting the ubiquitin model from the crystal structure and including density for ubiquitin from the cryo-EM reconstruction (EMD: 9045), displayed in dark gray mesh. (D) Cutaway view of the cryo-EM density (EMD: 9045) and atomic model (PDB: 6EF3) for the AAA+-motor engaged substrate, with substrate in red, ubiquitin in violet, Rpt1 in blue, and the pore-loop tyrosine residues of all six Rpts shown in dark blue. The substrate traverses through the N-domain ring (dark gray), makes contact with five of the six Rpts (Rpt1

7

density and atomic model shown in cornflower blue), and reaches into the core particle (light gray). (E) Zoomed-in representation of (D) with substrate density (EMD: 9045) shown in dark gray mesh and four of the five engaged pore loops in in dark blue. (F) Cut-away density (EMD: 9045; PDB: 6EF3) of the substrate (red) entering through the gate of the core particle (gray). The atomic model (PDB: 6EF3) for the core particle is displayed in dark gray, with the proteolytic active site residues highlighted as red spheres and the atomic model for substrate shown in red. (G) Representation of core particle density (EMD: 9045) from the top-down, with the gate shown fully open and occupied with substrate (red; PDB: 6EF3). The docking sites for Rpts' C-terminal HbYX motifs are circled and labeled with the respective Rpt binding partner. (H) Cartoon representation of the substrate-degradation pathway with time constants derived from (Bard *et al.* 2019). A substrate (red) containing an unstructured initiation region and an ubiquitin modification (magenta) is recruited to the proteasome via intrinsic proteasome receptors (dark purple). The substrate's unstructured region can passively diffuse into the central channel before being gripped by the pore loops (dark red) of the AAA+ ATPase (blue). This substrate engagement drives a major conformational switch, committing a substrate to degradation via a kinetic gateway and placing Rpn11 into a coaxially aligned position with the AAA+ motor for co-translocational deubiquitination. Substrates are then unfolded and translocated into the core particle for proteolytic cleavage. Unfolding appears to be the rate-limiting step of degradation for substrates of this architecture, with time constants depending on a substrate's thermodynamic stability.

Conformations of the 26S Proteasome

Recent technological advancements in cryo-EM have enabled detailed structural studies of macromolecular complexes, like the proteasome, in near-atomic detail. The ability to extensively subclassify individual particles ideally poises cryo-EM to quantitatively discern the conformational distribution of macromolecular complexes under controllable conditions. Indeed, cryo-EM studies have uncovered numerous conformations of the proteasome, describing no fewer than 7 distinct conformations and upwards of 15 in total, depending on what is defined as a unique state (Aufderheide et al., 2015; Bashore et al., 2015; Beck et al., 2012; Chen et al., 2016; Ding et al., 2017, 2019; Dong et al., 2019; Eisele et al., 2018; Da Fonseca et al., 2012; Greene et al., 2019; Haselbach et al., 2017; Huang et al., 2016; De la Peña et al., 2018; Lander et al., 2012; Lasker et al., 2012; Luan et al., 2016; Matyskiela et al., 2013; Schweitzer et al., 2016; Śledź et al., 2013; Unverdorben et al., 2014; Wehmer et al., 2017; Zhu et al., 2018). These conformations can be broadly categorized into two groups: the substrate-free ground state s1 and the non-s1 states, the latter of which are highly similar, primarily reflect the Rpt motor at different stages of the ATP-hydrolysis cycle, and require a major conformational transition from s1 (Greene et al., 2020). During this transition from the s1 to any non-s1 conformation, the lid subcomplex rotates ~ 30° relative to the base, leading to a ~ 30 Å shift for some of the peripheral lid subunits (Figure 1.4A).
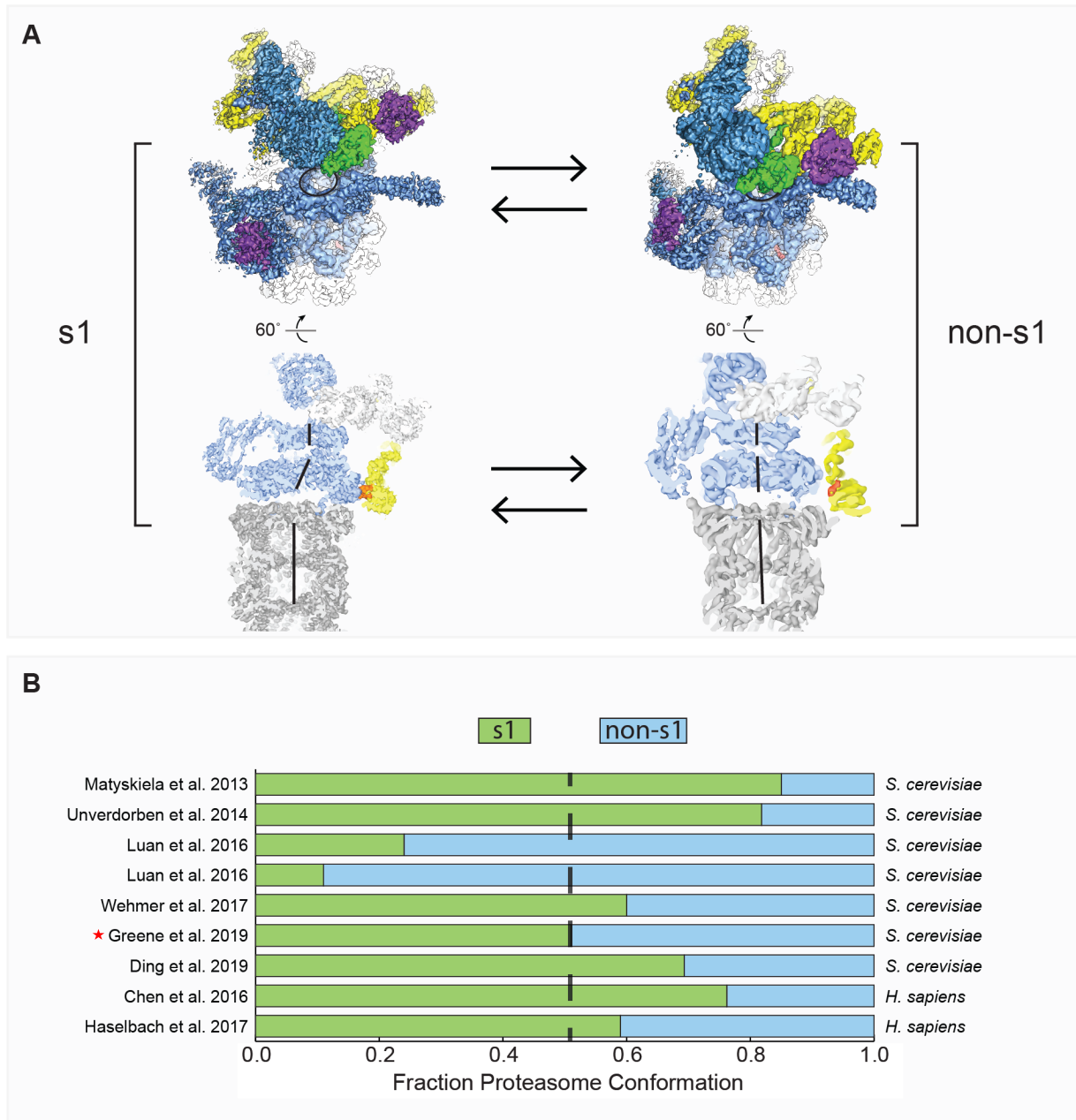
Figure 1.4: Ground-state conformational equilibrium of the 26S proteasome. (A) Top: Cryo-EM densities of the 26S proteasome in the s1 (EMD: 3534, left) and s2 (EMD:3535, right) conformations, with Rpn11 (green) offset or coaxially aligned with the pore of the AAA+ motor (dark blue). Ubiquitin receptors are in purple, lid subunits in yellow, and Rpn1 and Rpn2 are in dark blue. Bottom: cryo-EM densities of the 26S proteasome in the s1 (EMD: 3534, left) and s3 (EMD:3536, right) conformations, highlighting the s1-specific contacts (orange) between the lid subunit Rpn5 (yellow), the AAA+ motor (cornflower blue), and the coaxial alignment of the AAA+ motor with the core particle (gray) in the s3 conformation. Other lid subunits are in light gray. (B) Bar graph of the fraction of proteasomes in s1 (green) or non-s1 (blue) conformations observed in *in vitro* cryo-EM or negative stain-EM (highlighted with a red star) with a dashed line indicating 50%. All datasets were collected of proteasomes under similar conditions with ATP as the principle nucleotide, without substrate present, and without the addition of effector proteins that could bias the conformational landscape. Under these conditions, the predominant non-s1 conformation is the s2 conformation in all studies except Luan et al. 2016 for which an s3 state is described (Bard et al 2018). Left, are the studies from which data were derived. Right, are the species from which the proteasome distribution describes.

9

The s1 state is typically predominant in the absence of substrate (Fig 1.4B), whereas substrate-engaged proteasomes nearly exclusively display non-s1 states, indicating that substrate engagement with the AAA+ motor induces the conformational switch. The non-s1 states are conserved between yeast and human proteasomes and share common global characteristics. These include the positioning of Rpn11 directly above the central pore of the ATPase motor, a coaxial alignment of the N-ring, ATPase ring, and the α-gate of the core particle, and a large, 30° rotation of the lid compared to the s1 conformation (Figure 1.4A). The proteasome conformational landscape and the distribution between s1 and non-s1 states are influenced by multiple factors, including non-hydrolyzable nucleotide analogs, substrate binding, the interaction with proteasome-associated proteins, and even unanchored ubiquitin-chain binding (reviewed in Bard et al., 2018; Greene et al., 2020). In all cases to date, these conformational effectors tend to promote non-s1 conformations of the proteasome.

In the absence of substrate or other effectors, the ATP-bound proteasome is found in an equilibrium between two major conformations, s1 and s2 (Figure 1.4B). This equilibrium distribution varies from study to study (Figure 1.4B), however, the s1 conformation is typically predominant. Indeed, *in situ* cryo-electron tomography studies of the proteasome in mammalian cells have also described the s1 state as the predominant conformation, constituting 60-80% of conformationally quantifiable species (Albert et al., 2017; Asano et al., 2015; Guo et al., 2018). The s2 conformation shows Rpn11 poised directly above the central channel of the AAA+ ATPase motor, similar to the broader non-s1 conformations. This positioning severely obstructs access to the central pore for incoming substrates (Figure 1.4A) and may hinder the degradation process. Addition of non-hydrolyzable ATP analogs is known to induce non-s1 conformations and inhibit substrate degradation. But besides leading to potential steric interference with substrate insertion in the central pore (Bard et al., 2019), eliminating ATP hydrolysis also shuts down the motor and prevents any translocation, and substrate engagement, leaving several key questions unanswered: What is the functional importance of the conformational equilibrium between s1 and non-s1 states? What role does the lid play in regulating proteasome conformations? Can we selectively perturb this conformational equilibrium to study function without inhibiting the AAA+ motor? What steps in the degradation process are primarily influenced by the conformational equilibrium?

In the following chapters, I will present evidence for the lid subcomplex playing a role in determining proteasome conformation, that non-s1 conformations hinder substrate engagement, and that the dynamics of proteasome conformational switching appear crucial to overall degradation success. I will also answer the question of whether ubiquitination can alter the thermodynamics of an otherwise well-folded substrate protein to influence the degradation process? Taken together, I will present data that begin to illuminate how these factors influence proteasomal degradation and are a means of regulating the paramount process of selective protein degradation.

Chapter 2: Specific lid-base contacts in the 26s proteasome control the conformational switching required for substrate degradation

Abstract

The 26S proteasome is essential for proteostasis and the regulation of vital processes through ATP-dependent degradation of ubiquitinated substrates. To accomplish the multi-step degradation process, the proteasome's regulatory particle, consisting of lid and base subcomplexes, undergoes major conformational changes whose origin is unknown. Investigating the *Saccharomyces cerevisiae* proteasome, we found that peripheral interactions between the lid subunit Rpn5 and the base AAA+ ATPase ring are important for stabilizing the substrate-engagement-competent state and coordinating the conformational switch to processing states upon substrate engagement. Disrupting these interactions perturbs the conformational equilibrium and interferes with degradation initiation, while later processing steps remain unaffected. Similar defects in early degradation steps are observed when eliminating hydrolysis in the ATPase subunit Rpt6, whose nucleotide state seems to control proteasome conformational transitions. These results provide important insight into interaction networks that coordinate conformational changes with various stages of degradation, and how modulators of conformational equilibria may influence substrate turnover.

Introduction

The 26S proteasome is the principal ATP-dependent protease in eukaryotic cells and responsible for the majority of targeted protein turnover, both through the degradation of short-lived regulatory proteins and the clearance of damaged or misfolded polypeptides for protein-quality control (Hersko and Ciechanover, 1998). Ubiquitin ligases mark obsolete proteins with poly-ubiquitin chains and thereby target them to ubiquitin receptors on the 26S proteasome, which represents the last component of the ubiquitin-proteasome system and mechanically unfolds, deubiquitinates, and

translocates protein substrates into an internal chamber for proteolytic cleavage (Bard et al., 2018). To accomplish these various tasks of substrate processing, the 26S proteasome undergoes significant conformational rearrangements whose origin and control still remain largely elusive.

At the center of the 26S proteasome is a barrel-shaped core peptidase with sequestered proteolytic active sites (Groll et al., 1997). This core is capped on one or both ends by a regulatory particle that consists of two subcomplexes, referred to as the "lid" and the "base", and is responsible for the recognition, unfolding, and transfer of protein substrates into the core (Bard et al., 2018; Glickman et al., 1998b). The base contains 10 subunits, including three ubiquitin receptors, Rpn1, Rpn10, and Rpn13, the large scaffolding subunit Rpn2, and six distinct ATPases that form a ring-shaped, heterohexameric AAA+ (ATPase Associated with various cellular Activities) motor in the order Rpt1-Rpt2-Rpt6-Rpt3-Rpt4-Rpt5 (Tomko et al., 2010). These ATPases dock on top of the core peptidase to open its gate for substrate transfer (Smith et al., 2007). As in other protein unfoldases of the AAA+ family, the six Rpt subunits in the proteasome base use loops with conserved aromatic residues projecting into the central pore of the hexamer to interact with the substrate polypeptide, mechanically pull on it, and drive its translocation into the 20S core in an ATP hydrolysis-dependent manner. These loops lie deep in the pore, such that appropriate substrates require not only a ubiquitin modification for binding to a proteasomal receptor, but also a flexible initiation region of 20–25 residues to reach and engage with this AAA+ translocation machinery (Bard et al., 2019; Prakash et al., 2004).

The nine-subunit lid binds to one side of the base and thus further expands the regulatory particle's asymmetry contributed by the heterohexameric ATPase ring. The lid includes the Zn^{2+}-dependent deubiquitinase (DUB) Rpn11 (Glickman et al., 1998c; Verma et al., 2002; Yao and Cohen, 2002) in a hetero-dimeric complex with another MPN-domain containing subunit, Rpn8 (Worden et al., 2014), as well as six scaffolding subunits, Rpn3, 5, 6, 7, 9, and 12. In addition to lid contacts with Rpn2 and the N-terminal regions of Rpt3 and Rpt6, the subunits Rpn5, Rpn6, and Rpn7 use their N-terminal TPR domains to specifically interact with the ATPase domains of Rpt4, Rpt3, and Rpt6, respectively (Lander et al., 2012; Lasker et al., 2012). Rpn5 and Rpn6 also contact the core peptidase and thus appear to form an external scaffold bridging the lid, base, and core subcomplexes within the proteasome holoenzyme (Lander et al., 2012; Matyskiela et al., 2013).

Previous cryo-electron microscopy studies identified multiple proteasome conformations with distinct relative orientations and contacts of base, lid, and core that are structurally conserved between yeast and human proteasomes (Ding et al., 2017; Dong et al., 2019; Eisele et al., 2018; De la Peña et al., 2018; Matyskiela et al., 2013; Śledź et al., 2013; Unverdorben et al., 2014; Wehmer et al., 2017). In the absence of substrate, the proteasome exists in two conformations, s1 and s2, in which Rpt1-Rpt6 form a spiral staircase arrangement with Rpt3 in the top position. In the s1 state, the ATPase ring is not coaxially aligned with the core peptidase, and Rpn11 is offset from the central processing channel, allowing substrate access to the pore entrance. In contrast, the s2 state is characterized by a rotated lid position relative to the base and a coaxial alignment of Rpn11, the ATPase ring, and the core peptidase (Unverdorben et al., 2014). Substrate engagement induces conformations that are overall very similar to s2, with a continuous central channel for efficient substrate translocation and a centrally aligned Rpn11 that leaves only a small gap to the subjacent Rpts for substrate to be pulled through, facilitating co-translocational deubiquitination (Dong et al., 2019; De la Peña et al., 2018; Matyskiela et al., 2013). These substrate-processing states, named s3-s6 (Matyskiela et al., 2013; Unverdorben et al., 2014; Wehmer et al., 2017; Eisele et al., 2018; de la Peña

et al., 2018; Dong et al., 2019), show AAA+ motor conformations in which various Rpts adopt the individual vertical position in the spiral staircase, depending on the progression of the ATP-hydrolysis cycle in the hexamer. The s5 state thereby resembles s2, with the exception of the core gate that is open in s5 and closed in s2 (Eisele et al., 2018). Similar suites of substrate-engaged-like conformations can also be induced by incubating the proteasome with non-hydrolyzable ATP analogs (Śledź et al., 2013; Wehmer et al., 2017; Ding et al., 2017) or introducing Walker-B mutations (Eisele et al., 2018), both of which trap Rpts in the ATP-bound state and stabilize their interface to neighboring ATPase subunits in the hexamer. Our recent studies on the coordination of proteasomal degradation steps suggested that substrate engagement depends on the s1 state, in which the entrance to the central pore is accessible and the initiation region of a ubiquitin-receptor-bound substrate would be able to enter the AAA+ motor (Bard et al., 2019). Premature switching to substrate-processing states seemed to prevent this substrate engagement, potentially due to Rpn11 obstructing the central pore. Yet alternative models could not be completely ruled out, because the substrate-processing states in those studies were induced by the addition of ATPγS (Bard et al., 2019), which abolishes translocation and may also interfere with substrate engagement.

Mutational studies, in which nucleotide binding or hydrolysis of single ATPase subunits were disrupted by substitutions in the Walker-A or Walker-B motifs demonstrated the functional asymmetry of the proteasomal AAA+ motor, as the same mutations in different Rpts caused varied effects on cell viability and the degradation of ubiquitinated substrates (Beckwith et al., 2013; Eisele et al., 2018; Rubin et al., 1998; Wendler et al., 2012). However, it remains unclear to what extent these differences in proteasomal activity originate from individual Rpt subunits playing unequal roles in mechanical substrate processing, or from these mutations differentially affecting the overall conformational switching of the proteasome.

Here, we investigate how interactions between the lid and base subcomplexes influence the conformational transitions and thus substrate processing by the *Saccharomyces cerevisiae* 26S proteasome. Previous structural studies showed that the contacts between Rpn5's TPR domain and the small AAA+ subdomain of Rpt3 are broken during the regulatory particle's transition from the substrate-free s1 state to any other state (Matyskiela et al., 2013; Unverdorben et al., 2014; Wehmer et al., 2017; Eisele et al., 2018; Ding et al., 2017; de la Peña et al., 2018; Dong et al., 2019). Through mutations of the involved residues in Rpn5, we found that loss of these interactions perturbs the conformational landscape and allows the proteasome to more strongly populate substrate-engaged-like conformations even in the absence of substrate. Walker-B mutations that prevent ATP hydrolysis in individual subunits of the AAA+ motor similarly disrupt the conformational equilibrium. In both cases, perturbing the coordination between substrate-processing steps and conformational transitions of the proteasome's regulatory particle leads to decreased degradation rates, primarily by affecting the initiation of processing and shifting the rate-limiting step from substrate unfolding to engagement. Our data thus reveal how the proteasome uses the peripheral interactions with the lid subunits to orchestrate the conformational transitions required for the various stages of ubiquitin-dependent substrate degradation.

<u>Results</u>

The lid is required for proteasome function independent of deubiquitination

Structural rearrangements, specifically the rotation of the lid relative to the base observed in response to substrate processing or binding of ATP analogs to the AAA+ motor, suggest that the lid may be directly involved in determining the proteasome conformational states (Matyskiela et al., 2013; Unverdorben et al., 2014; Wehmer et al., 2017; Eisele et al., 2018; Ding et al., 2017; de la Peña et al., 2018; Dong et al., 2019). However, the lid's structural importance for degradation cannot simply be tested by eliminating this subcomplex from the holoenzyme, as it contains the essential DUB Rpn11 and is indispensable for efficient ubiquitin-dependent substrate turnover (Verma et al., 2002). We therefore used our previously established ubiquitin-independent substrate-delivery system, in which the bacterial SspB adaptor fused to Rpt2 allows the recruitment of model substrates containing the ssrA recognition motif (Bashore et al., 2015). Degradation was monitored through the decrease in anisotropy of a titin-I27^{V15P} model substrate that contained a destabilizing V15P mutation, fluorescein conjugated to the N-terminus, and a C-terminal 35 amino-acid initiation region derived from cyclin B that also included the ssrA recognition motif (FAM-titin-I27^{V15P}). Even though we eliminated the dependence on Rpn11-mediated deubiquitination, presence of the lid was still required for efficient ATP-dependent degradation (Figure 2.1A; Figure s2.1A and B). In contrast to other compartmental proteases, the proteasomal AAA+ motor and the 20S core peptidase together are not sufficient to catalyze ATP-dependent protein unfolding and degradation.
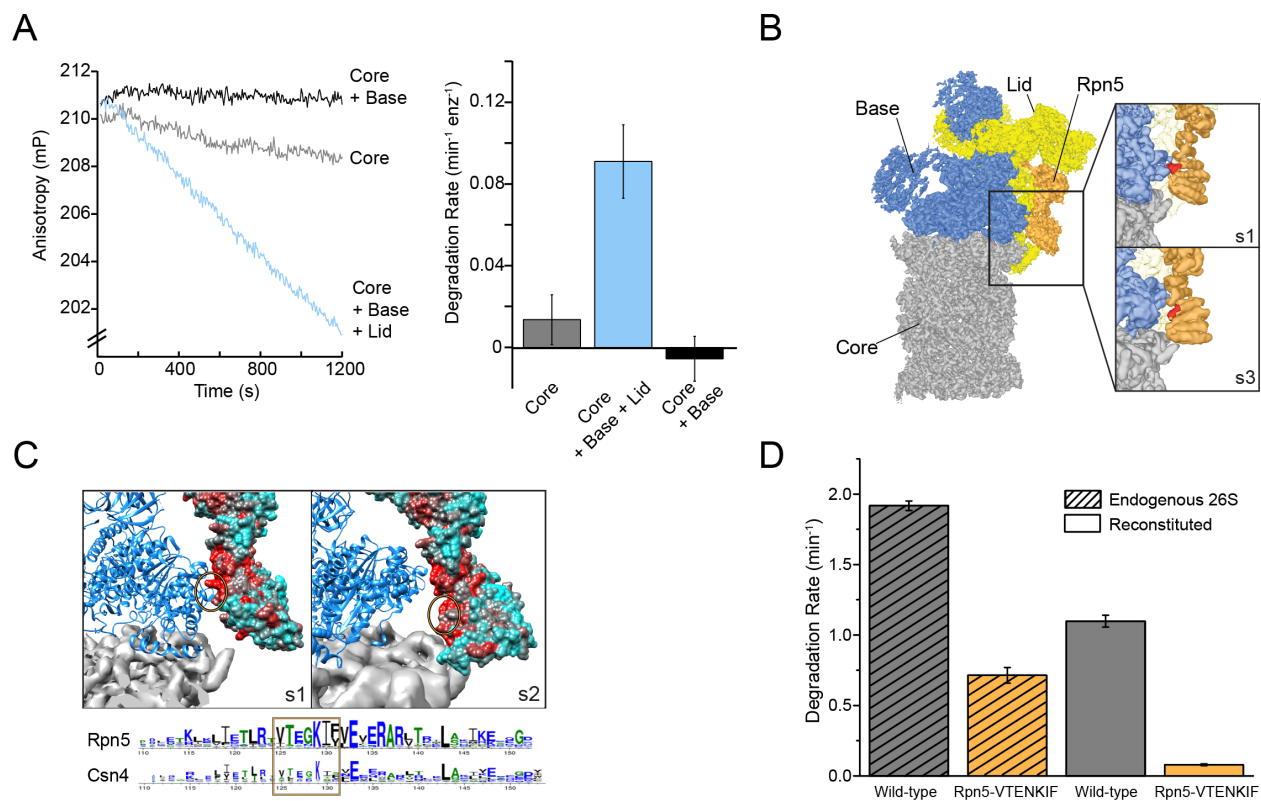
Figure 2.1. The proteasome lid subcomplex is required for proteasome function through direct contacts with the AAA+-motor.

(**A**) Ubiquitin-independent degradation of fluorescein-labeled, ssrA-tagged FAM-titin-I27^{V15P} substrate by in-vitro reconstituted 26S proteasomes with recombinantly produced SspB-fused base in the absence and presence of recombinantly produced lid subcomplex was monitored through fluorescence anisotropy under multiple-turnover conditions. Shown on the left are representative traces of changes in anisotropy, and shown on the right are the rates of degradation calculated from these data (N = 3, technical replicates, error bars plotted are SEM). (**B**) Cryo-EM structure of the 26S proteasome from S. cerevisiae (EMDB code: 3534) highlights contacts between the lid (yellow and orange), base (blue), and core (grey). The lid subunit Rpn5 (orange) uses a VTENKIF-sequence-containing loop (red) to interact with the small AAA+ subdomain of the base subunit Rpt3 in the substrate-free s1 conformation, but not in any other conformation, like s3 shown here (EMDB: 4321). (**C**) The Rpn5 interface with the AAA+ ATPase is conserved within proteasome specific sequences. Red surface represent highly conserved residues and cyan surface represents non-conserved residues. Conservation was determined through collecting reciprocal BLAST hits from the InParanoid8 data set (Sonnhammer and Östlund, 2015) for Rpn5 and its homolog Csn4 in the Cop9 signalosome before performing a multiple sequence alignment in GREMLIN (Ovchinnikov et al., 2014). Blue ribbon represents the base ATPase subunits and gray density represents the core particle of the s1 conformation (left, PDB 5MPD, EMD 3534) and s2 conformation (right, PDB 5MPC, EMD 3536). (**D**) Rates for the single-turnover degradation of a ubiquitinated, TAMRA-labeled G3P substrate with 54 amino acid tail derived from cyclin-b sequence (TAMRA-G3P) by wild-type and Rpn5-VTENKIF mutant proteasomes that were purified from S. cerevisiae (shaded) or in-vitro reconstituted using recombinant lid and base (solid) (N = 3, technical replicates, error bars plotted are SEM).

Interactions between the lid and the AAA+ motor have been found to change in the various proteasome conformations, and these changes of contact points thus represent a possible mechanism by which the lid could act allosterically with the base to influence the regulatory particle's conformational switching during substrate processing. Of particular interest was the contact between Rpn5's TPR domain and Rpt3's small AAA+ subdomain that is present only in the substrate-free s1 state (Figure 2.1B and C; Matyskiela et al., 2013; Unverdorben et al., 2014; Wehmer et al., 2017; Eisele et al., 2018). Mutating all highly conserved residues in the Rpt3-contacting loop of Rpn5 (V125 - F131) to alanine (mutant denoted Rpn5-VTENKIF) decreased the rate of both, ubiquitin-dependent (Figure 2.1C, Figure s2.1B and C) and ubiquitin-independent degradation (Figure s2.1—s2.1 A and B). Importantly, this loss of degradation activity is not primarily caused by

defects in proteasome assembly, which was found by native PAGE to be only slightly less efficient for the mutant compared to the wild-type enzyme (Figure s2.2). Furthermore, using the response of the base ATPase activity to lid binding during holoenzyme assembly, we determined similar affinities for wild-type and Rpn5-VTENKIF mutant lid (Figure s2.1D). Despite their lower degradation activity, Rpn5-VTENKIF mutant proteasomes show an elevated ATPase rate in the absence of substrate that increases in response to substrate processing, albeit to a lesser extent than for wild type (Figure s2.1D). In agreement with recent findings (Nemec et al., 2019), proteasomes containing the Rpn5-VTENKIF mutation more strongly retained the Nas6 assembly chaperone during holoenzyme reconstitution (Figure s2.1E). However, this presence of Nas6 is not the main cause for the observed decrease in degradation rate, as purified endogenous proteasomes from *S. cerevisiae* carrying the same Rpn5 mutations also exhibit major deficiencies in single-turnover degradation reactions (Figure 2.1C), despite containing only negligible amounts of Nas6 (Figure s2.1F). Moreover, we found that substrate processing efficiently evicts most Nas6 from nascent Rpn5-VTENKIF mutant proteasomes (Figure s2.1E), indicating that the initial Nas6 retention is not responsible for the steady-state substrate processing defect of the Rpn5-VTENKIF mutant. Overall, the observed decrease in degradation activity appears to principally be caused by intrinsically compromised substrate processing, rather than the observed minor defects in the assembly or composition of proteasome holoenzymes (Figure s2.1 and s2.2).

Lid-base contacts influence proteasome conformation

We employed negative-stain electron microscopy to assess the conformational states of the proteasome and whether the Rpn5-VTENKIF mutation affects their distribution. Because the 20S core can be singly- or doubly-capped by regulatory particles, proteasome particles were half-masked to treat each regulatory particle independently for data processing (Figure s2.3 and s2.4). Consistent with previous observations, ATP-bound wild-type proteasomes in the absence of substrate were observed in two conformations, s1 and s2 (Figure 2.2A; Figure s2.5; Bard et al., 2018). Despite the limited resolution of negative-stain electron microscopy, these conformations could be distinguished from each other and from the substrate-bound states, in which the lid is even more rotated relative to the base, as obvious from the positioning of the horse-shoe shaped structure formed by the 6 PCI (Proteasome/Cyclosome/eIF3)-domain-containing lid subunits (Figure 2.2B, Figure s2.6). In contrast to wild-type proteasomes with nearly equal distribution of s1 and s2 conformations, Rpn5-VTENKIF mutant proteasomes showed only 37% of particles in the s1 state, while also populating substrate-engaged-like states (s3/s4/s6) that are absent from wild-type samples in the presence of ATP (Figure 2.2A, s2.5, s2.7, s2.8). Interestingly, the Rpn5-VTENKIF mutant displayed predominantly s2 or s5 conformations, which similar to s3, s4, and s6 are characterized by Rpn11 obstructing the central pore. The lower population of the s1 state resembles the scenario for Walker-B mutant proteasomes that in recent structural studies were found to have perturbed conformational landscapes as well (Eisele et al., 2018). Importantly, however, with bound ATPγS the Rpn5-VTENKIF mutant proteasomes behaved similar to wild-type in shifting to a conformational distribution that is dominated by substrate engaged-like states, which demonstrates their retained ability to conformationally respond when Rpt subunits are trapped in an ATP-bound state.
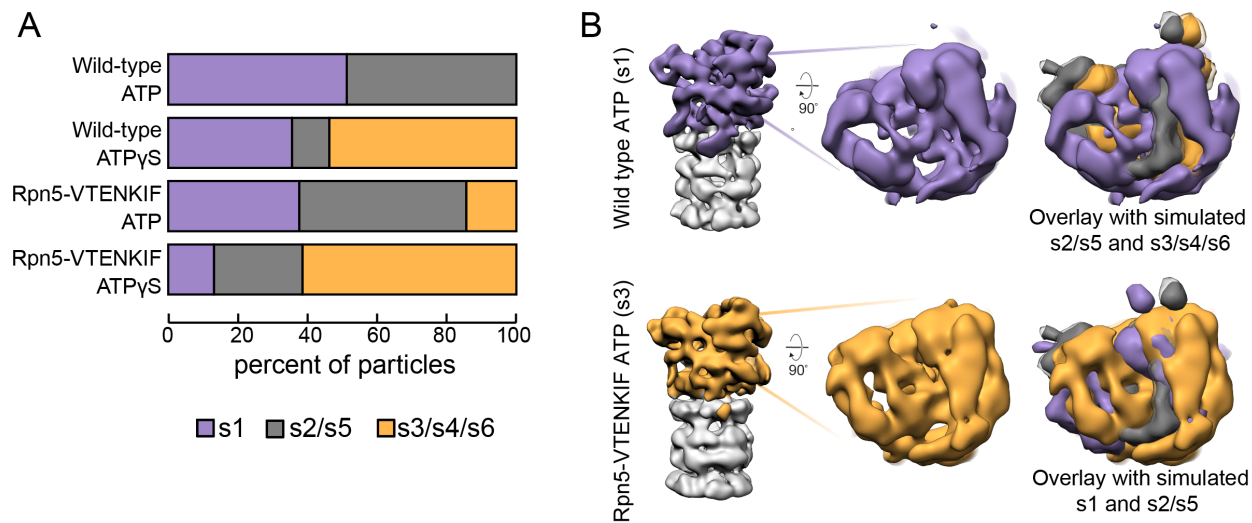
Figure 2.2. Rpn5 interactions with the AAA+ ring are required for maintenance of the s1 state.
(**A**) Proportion of each proteasome conformation observed by negative-stain electron microscopy for wild-type or Rpn5-VTENKIF proteasome in the presence of ATP or ATPγS. Designation of substrate-free and engaged-like conformations (s1, s2/s5, s3/s4/s6) was based on best fit to the atomic models provided in Eisele et al. (2018) and more details of the classification are provided in Figure 2—figure supplement 1–6. (**B**) Representative densities for wild-type proteasome in the s1 conformation (top, purple) and Rpn5-VTENKIF mutant proteasome in the s3/s4/s6 conformation (bottom, orange), overlaid with low-resolution envelopes generated from the atomic models for the given state in Eisele et al. (2018) aligned by their core particles (grey). In the overlay s2/s5 is shown in grey, s3/s4/s6 is shown in orange, and s1 is shown in purple.

The nucleotide states of Rpt6 and Rpt4 affect proteasome conformational switching

Binding of non-hydrolyzable ATP analogs to the proteasomal AAA+ motor triggers similar conformational changes as substrate engagement, suggesting that stabilizing Rpt subunits in an ATP-bound state or coordinating nucleotide binding and hydrolysis in several substrate-interacting Rpt subunits provides a common driving force for conformational transitions. To assess in more detail how perturbations in ATP-hydrolysis affect the conformational states of the proteasome, we placed Walker-B mutations (Glu to Gln) in individual Rpts. Consistent with previous in vitro and in vivo studies that revealed unequal contributions of Rpts to proteasomal degradation activity (Eisele et al., 2018; Beckwith et al., 2013), we observed differentially reduced rates of substrate turnover for these variants (Figure s2.9A), with the strongest defects seen in Rpt subunits that make contacts with TPR domains of lid (Rpt3, Rpt6, and Rpt4, Figure 2.3A). As a readout for their conformational state, we analyzed how Walker-B mutants responded in their ATPase activity to the interaction with ubiquitin-bound Ubp6. Ubp6 is a non-essential, proteasome-interacting DUB that in its ubiquitin-bound form biases the proteasome's conformational equilibrium away from the s1 state and thereby stimulates the ATPase activity similar to substrate processing (Aufderheide et al., 2015; Bashore et al., 2015; Peth et al., 2013). Despite significantly different basal ATPase rates, proteasome variants with a Walker-B mutation in Rpt1, Rpt2, Rpt3, or Rpt5 still maintain some Ubp6-mediated stimulation of ATP hydrolysis (Figure 2.3B, Figure s2.9B). However, two mutants with severe degradation defects, Rpt6-EQ and Rpt4-EQ, did not respond to ubiquitin-bound Ubp6 (Figure 2.3B, Figure s2.9B), suggesting that a considerable fraction of those proteasomes adopt non-s1 states already in the absence of ubiquitin-bound Ubp6. Additionally, this failure to respond to ubiquitin-bound Ubp6 does not originate from compromised holoenzyme assembly (Figure s2.2, s2.10).
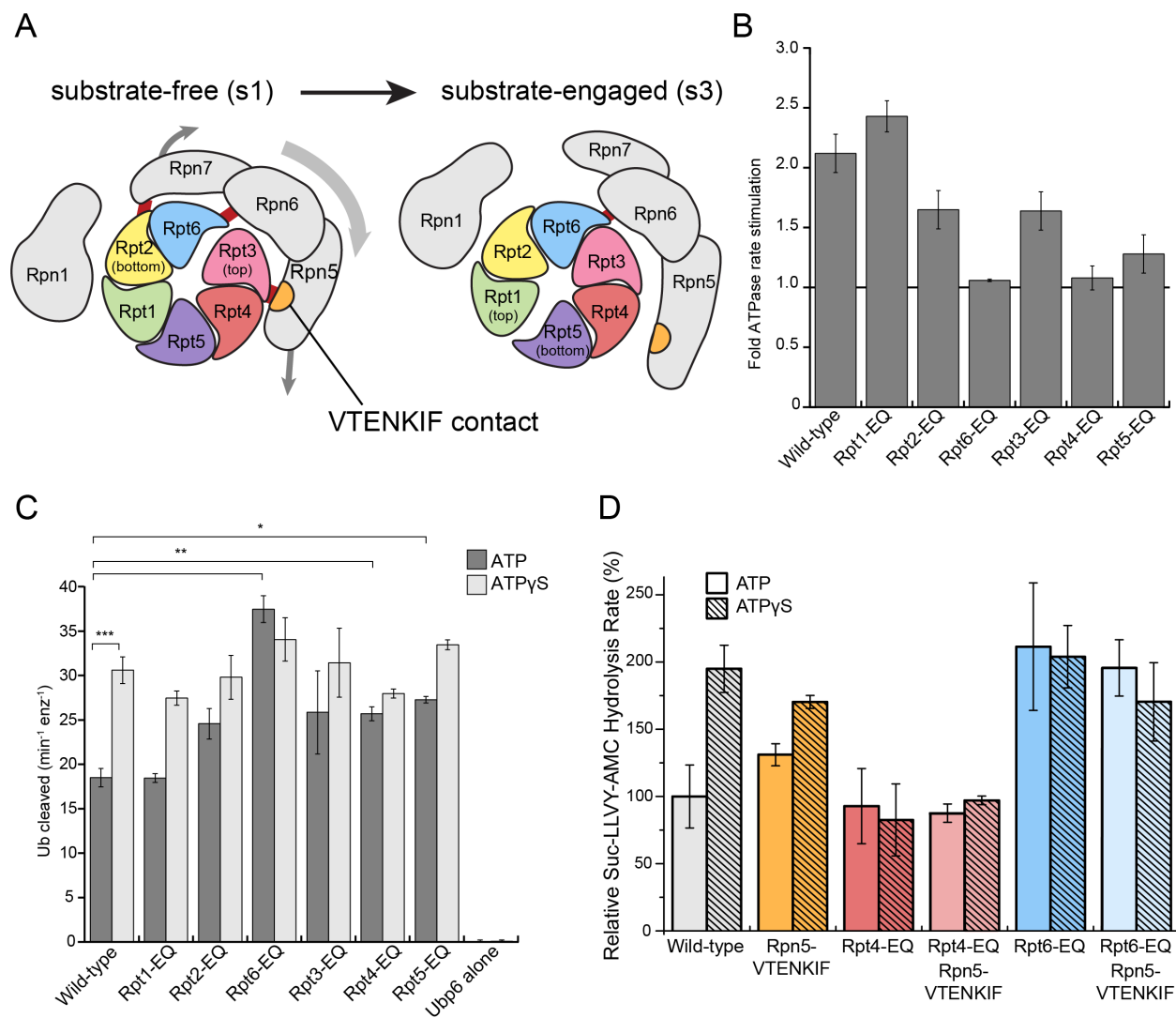
Figure 2.3. Walker-B mutations in Rpt6 and Rpt4 influence proteasome conformational switching and are dominant over Rpn5-VTENKIF mutation.

(**A**) Cartoon of the proteasome heterohexameric AAA+-motor and interacting lid subunit as viewed from the top, with the core particle underneath. The base subunit Rpn1 and lid subunits are shown in grey, with red bars indicating the interactions between the VTENKIF region of Rpn5 (orange) and the AAA+ domain of Rpt3 (pink), as well as the Rpn6-Rpt6 and Rpn7-Rpn2 contacts. The ATPase subunits Rpt1, Rpt2, Rpt6, Rpt3, Rpt4, and Rpt5, depicted in rainbow colors, are forming a vertical spiral staircase. In the substrate-free s1 state, Rpt3 is at the top of this staircase, Rpt2 at the bottom, and Rpt6 represents the seam subunit with an open ATPase interface to its neighbor Rpt3. In the substrate-engaged s3 state, Rpt1 is at the top and Rpt5 at the bottom, with an open seam between the two. As the ATPase ring transitions through the various engaged states during ATP hydrolysis, the staircase and the open seam are expected to progress in a counterclockwise manner around the ring (de la Peña et al., 2018). (**B**) Proteasome ATPase stimulation by ubiquitin-bound Ubp6, with no stimulation indicated by a solid black line (N ≥ 3, technical replicates, error bars plotted are SEM). (**C**) Ub-AMC cleavage activities of Ubp6 in the context of wild-type or Walker-B mutant proteasomes with ATP or ATPγS (N ≥ 3, technical replicates, error bars plotted are SEM, p values shown for a Student's T-test). (**D**) Core gate-opening measured through cleavage of the fluorogenic Suc-LLVY-AMC substrate. Cleavage rates were determined by linear fitting of the AMC-fluorescence increase, normalized to wild-type proteasome in ATP, and plotted as averages with standard deviations (N ≥ 3, technical replicates).

Notably, there is a reciprocal crosstalk between the proteasome and Ubp6, in which Ubp6's DUB activity depends on the proteasome conformation, and the highest activity is observed when the catalytic USP domain of Ubp6 interacts with the AAA+ motor in non-s1 states (Bashore et al.,

2015). All Walker-B mutants except Rpt1-EQ showed increased Ubp6 DUB activity in the presence ATP, but resembled the wild-type enzyme when in ATPγS (Figure 2.3C), confirming their normal conformational response to nucleotide. That Rpt6-EQ and Rpt4-EQ-mutant proteasomes show increased Ubp6 DUB activity in ATP is consistent with their lack of Ubp6-mediated ATPase stimulation and further suggests that trapping Rpt4 or Rpt6 in permanent ATP-bound states populates non-s1 conformations, even in the absence of substrate or ATPγS (Figure 2.3C).

Rpt4-EQ and Rpt6-EQ mutant proteasomes showed strong degradation defects and were consistent in both, Ubp6-mediated ATPase stimulation and Ubp6 DUB activation, indicating a conformational bias away from the engagement-competent s1 state. We therefore tested their core gate-opening activities through fluorogenic peptide hydrolysis in the presence of ATP or ATPγS. Complete opening of the core particle gate requires the docking of five Rpt C-terminal tails: Rpt2, Rpt3, Rpt5, Rpt1, and Rpt6, with the latter two only found fully-docked in substrate engaged-like conformations - that is, during degradation or in the presence of non-hydrolyzable ATP analogs (Eisele et al., 2018; de la Peña et al., 2018; Dong et al., 2019; Zhu et al., 2018). The Rpt6-EQ mutant showed elevated gate opening in the presence of ATP that resembled the ATPγS-bound wild-type proteasome and did not further increase upon ATPγS addition (Figure 2.3D), which is consistent with this variant being biased towards an engaged-like conformation due to trapping Rpt6 in a permanent ATP-bound state. Consistently, the Rpn5-VTENKIF mutant proteasome, whose conformational distribution appeared partially shifted in our EM analyses, exhibited moderately increased core gate-opening and peptide-hydrolysis activity that still responded to ATPγS. Proteasomes containing the combined Rpn5-VTENKIF and Rpt6-EQ mutations behaved largely similar to the Rpt6-EQ mutant proteasome, indicating that preventing ATP hydrolysis in Rpt6 and thus stabilizing the interface with Rpt3 has a dominant effect on determining the conformational state, at least with respect to core-particle docking and gate-opening.

Although Rpt4-EQ mutant proteasomes also appeared to be biased towards engaged-like, non-s1 conformations based on their crosstalk with Ubp6, their core-gate opening resembled the ATP-bound wild-type holoenzyme and was not responsive to ATPγS binding (Figure 2.3D). These proteasomes displayed decreased assembly under non-equilibrium conditions in native-PAGE analyses, which could explain some, yet not all of the gate-opening defects, as holoenzyme is clearly formed (Figure s2.2). Moreover, the gate-opening activity of the Rpt4-EQ mutant was insensitive to increased base concentrations (Figure s2.10), arguing against an assembly defect as the main reason for the functional deficiencies and suggesting that a biased conformational landscape of assembled proteasome is largely responsible for the observed effects. The Rpt4-EQ mutation thus seems to induce a partially distorted conformation that interacts with ubiquitin-bound Ubp6 similar to an engaged-state proteasome, but fails to properly dock with core particle for complete gate opening. Like the Rpt6-EQ mutation, the Rpt4-EQ mutation is dominant in determining the conformational state and therefore masks the stimulating gate-opening effects of the Rpn5-VTENKIF mutation in the combined mutant (Figure 2.3D). Compromising the lid-base interface through Rpn5-VTENKIF mutations thus appears to partially shift the conformational equilibrium of the proteasome, while trapping Rpt6 or Rpt4 in ATP-bound states overrules those changes and further shifts the equilibrium towards either a fully engaged-like or a distorted, potentially off-pathway conformation.

Proteasomes with biased conformational landscapes display various degradation defects

To understand how these conformation-influencing mutations affect substrate degradation, we first performed Michaelis-Menten kinetic analyses using our ubiquitinated FAM-titin-I27^{V15P} model substrate with a C-terminal 35 amino-acid initiation region that contained a single lysine-attached ubiquitin chain next to the titin folded domain. Rpt4-EQ mutant proteasome showed no discernable degradation activity at any substrate concentrations tested (Figure 2.4A), and further measurements under single-turnover conditions revealed only a small change in anisotropy that we could attribute solely to substrate deubiquitination (Figure 2.4B), as no peptide products were detected in an end-point analysis by SDS-PAGE (Figure 2.4C). These results were confirmed using an additional model substrate, ubiquitinated TAMRA-G3P (Figure s2.11B), for which the small amounts of produced peptides could be attributed to nonspecific proteolysis of the unstructured region by the core particle, as previously observed (Bard et al., 2019; Myers et al., 2018; Wenzel and Baumesiter, 1995). Furthermore, free Rpt4-EQ-containing regulatory particle, a prominent species in the native-PAGE analysis (Figure s2.2), harbored little deubiquitination activity compared to wild-type, Rpn5-VTENKIF, and Rpt6-EQ mutant RPs (Figure s2.11A–D). For all wild-type and mutant proteasomes tested, the addition of excess regulatory particle did not change the rate of substrate processing, that is degradation or deubiquitination that would lead to changes in anisotropy (Figure s2.11A,E). Interestingly, the deubiquitination activity of the Rpt4-EQ containing regulatory particle increases in a core-dependent manner (Figure s2.11A), suggesting that docking to the core particle positions Rpn11 in a more active conformation than in the free mutant RP (Dambacher et al., 2016). However, the Rpt4-EQ mutant proteasome lacks substrate engagement or translocation activities, and thus appears degradation-incompetent.

	K_M (μM)	k_{cat} (enz^{-1} min^{-1})
■ Wild-type:	0.31 ± 0.07	0.26 ± 0.02
● Rpn5-VTENKIF:	0.40 ± 0.05	0.042 ± 0.002
▲ Rpt6 EQ:	0.18 ± 0.03	0.046 ± 0.002
▼ Rpt4 EQ:	ND	ND
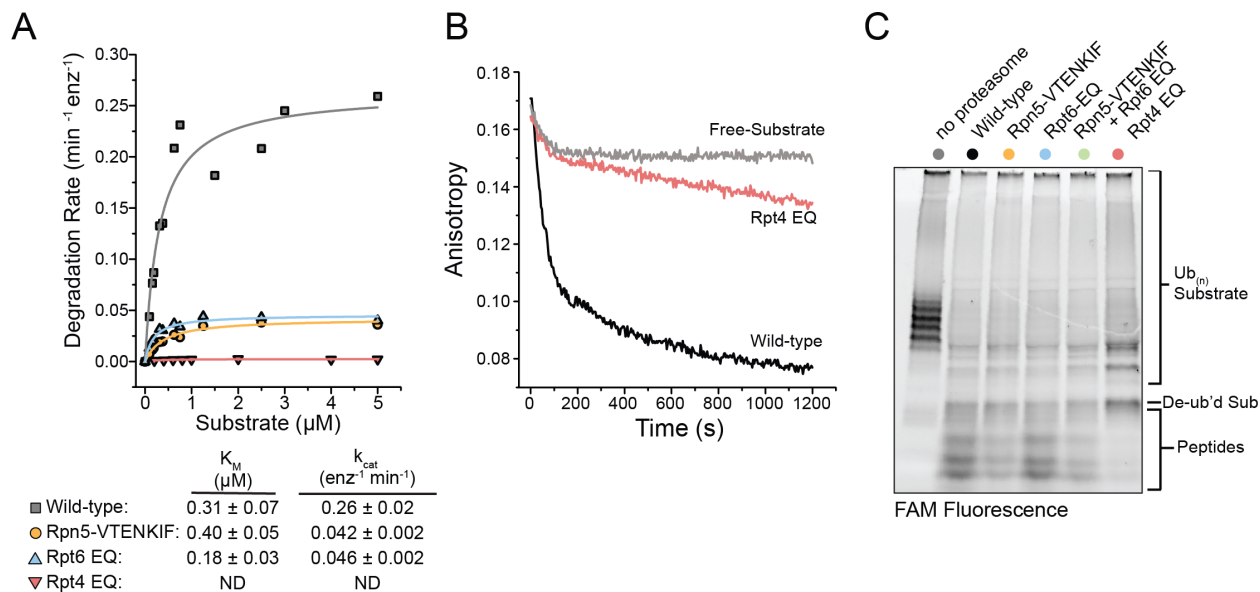
Figure 2.4. Proteasomes with impaired conformational switching display various degradation defects.
(**A**) Michaelis-Menten analysis based on initial rates for ubiquitin-dependent degradation of FAM-titin-I27^{V15P} under multiple-turnover conditions. K_m and k_{cat} values are shown below with errors representing SEM from the fit. Rpt4-EQ had too low activity to be fit. (**B**) Representative anisotropy traces for the single-turnover degradation of ubiquitinated FAM-titin-I27^{V15P} by wild-type and Rpt4-EQ mutant proteasomes (**C**) SDS-PAGE analysis of end-point samples from single-turnover degradation reactions, visualizing fluorescence of the FAM-titin-I27^{V15P} model substrate in its ubiquitinated, de-ubiquitinated, and degraded form.

The Rpt6-EQ and Rpn5-VTENKIF mutations decreased the k_{cat} for substrate degradation about 6-fold, with only minimal effects on K_m (Figure 2.4A). This behavior is expected, if these mutations primarily shift the conformational equilibrium and thereby reduce the fraction of engagement-competent s1-state proteasomes. We previously identified tail engagement to be a major determinant of K_m (Bard et al., 2019). Based on the lack of major K_m changes, we can thus conclude that the Rpt6-EQ and Rpn5-VTENKIF mutations do not considerably affect substrate engagement of proteasomes in the s1 state (Bard et al., 2019). It is assumed that non-s1 states that are not yet substrate-engaged do not significantly contribute to substrate processing, because their coaxially aligned position of Rpn11 right above the entrance to the pore interferes with substrate-tail insertion for degradation and also limits access to the DUB active site for potential translocation-independent deubiquitination. Accordingly, we did not detect deubiquitination and release of unmodified substrate from Rpn5-VTENKIF mutant proteasomes (Figure 2.4C; Figure s2.11), which is consistent with our previous findings that non-s1-state proteasomes with bound ATPγS show only low deubiquitination activity towards unengaged protein substrates (Worden et al., 2017). It is conceivable that the Rpn5-VTENKIF mutation reduces k_{cat} more strongly than the EM-observed shift in the conformational equilibrium would suggest, if weakening the lid-base interactions increases the dynamics of conformational transitions, and the life time of the engagement-competent s1 state in the mutant proteasomes is shorter than the time constant for substrate-tail insertion ($\tau = 1.6$ s; Bard et al., 2019). The Rpt6-EQ mutant proteasome were previously found to exhibit a similar distribution of s1 and non-s1 states as the Rpn5-VTENKIF mutant here (Eisele et al., 2018), and its rates of switching out of and back to the engagement-competent s1 state are expected to be determined by ATP binding and release of the hydrolysis-dead Rpt6 subunit. A 6-fold reduction in k_{cat} compared to wild-type proteasome can thus also be explained by compromised conformational switching and a shorter life time of the s1 state in the presence of the Rpt6-EQ mutation.

Disrupting the proteasome conformational equilibrium affects degradation initiation

We recently discovered that the engagement of a substrate's unstructured initiation region by the AAA+ motor triggers the major conformational change away from the s1 state, during which the contacts between the base and the VTENKIF-containing loop in Rpn5 are broken (Bard et al., 2019). We therefore aimed to investigate how the Rpn5-VTENKIF mutation with its effects on the conformational equilibrium influences this critical step of substrate processing. Using our previously established assay to monitor FRET between a fluorescence donor placed near the central channel of the base and an acceptor fluorophore attached to the substrate, we measured the kinetics of inserting the substrate's flexible tail into the pore (Bard et al., 2019). Inhibiting deubiquitination by Rpn11 with the Zn^{2+}-chelator ortho-phenanthroline (o-PA) stalls further translocation in these experiments and leads to the accumulation of stably engaged substrate in a high-FRET state. Our measurements revealed that tail insertion takes about twice as long for the Rpn5-VTENKIF mutant proteasome compared to wild type (Figure 2.5A, s2.12A). We assume that this rate represents a convolution of fast tail insertion for engagement-competent s1-state proteasomes and delayed tail insertion for proteasomes that first have to switch back to the s1 state. The Rpt6-EQ mutant proteasome displayed comparable tail-insertion defects (Figure s2.12B), indicating that initial substrate engagement is similarly compromised for both variants, likely due to changes in their conformational landscapes. In agreement with previous findings (Bard et al., 2019), very minimal, negligible tail insertion was observed with either proteasome variant in ATPγS or in the absence of core and lid (Figure 2.5A; Figure s2.12A).
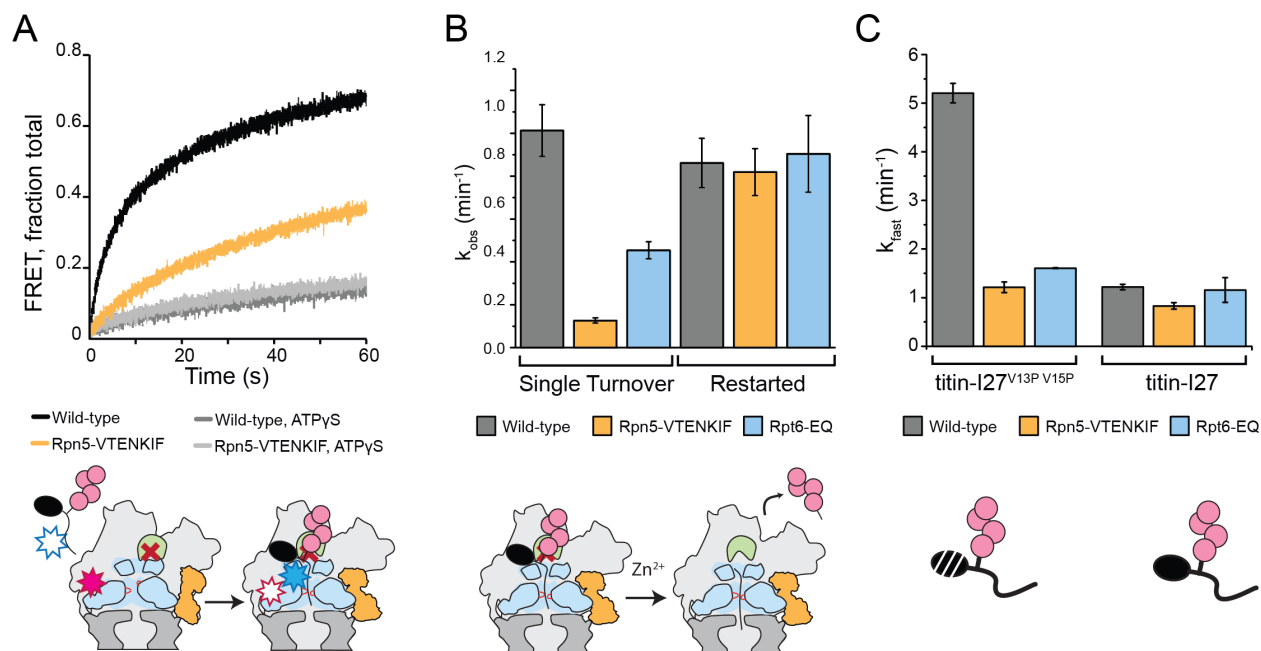
21

Figure 2.5. Disrupting the conformational equilibrium inhibits substrate tail insertion but not later steps of degradation.
(**A**) Representative traces for the increase in acceptor fluorescence/FRET upon insertion of the ubiquitinated FAM-titin-I27^{V15P}-Cy5 substrate's flexible initiation into the central pore of wild-type and Rpn5-VTENKIF mutant proteasomes with o-PA inhibited Rpn11, in the presence of ATP or ATPγS. The schematic below depicts the experimental setup, where FRET occurs when a substrate's flexible initiation region labeled with an acceptor dye (blue star) enters and then stalls in the central pore of a proteasome containing inhibited Rpn11 (red cross) and a donor dye (red star) near the processing channel. The substrate's ubiquitin modification is represented in pink, the Rpt ring is shown in light blue, the core particle in dark grey, and Rpn5 in orange. (**B**) Rate constants for the single-turnover, ubiquitin-dependent degradation of ubiquitinated G3P model substrate, either without stalling the proteasome (left) or after stalling translocation for 3 min with o-PA inhibited Rpn11 and restarting by the addition of Zn^{2+} (right). Rates were determined from single-exponential fits of the appearance of fluorescently tagged peptide products on SDS PAGE gels. Error bars represent SEM for the fit, $N \geq 3$, technical replicates. (**C**) Ubiquitin-dependent degradation rates for wild-type, Rpn5-VTENKIF and Rpt6-EQ mutant proteasomes degrading the destabilized FAM-titin-I27$^{V13P/V15P}$-35mer tail or the non-destabilized FAM-titin-I27-35mer tail substrate under single-turnover conditions. Shown are the rate constants for the dominant fast phase derived from a double-exponential fit of the degradation kinetics ($N = 3$, technical replicates, error bars represent SD).

To determine whether the degradation defects of Rpn5-VTENKIF and Rpt6-EQ mutant proteasomes originate primarily from delayed tail insertion when particles reside in the wrong state or from impaired subsequent processing steps as well, we performed degradation-restart experiments after stalling and accumulating engaged proteasomes through reversible o-PA-inhibition of substrate deubiquitination by Rpn11 (Worden et al., 2017). Upon release from the stall through the addition of excess Zn^{2+}, we monitored the depletion of ubiquitinated TAMRA-G3P substrate as well as the accumulation of peptides products by SDS-PAGE, both of which showed single-exponential behavior (Figure s2.13A). As expected, wild-type proteasomes displayed degradation kinetics in the restart experiments that resembled those under non-stalled, single-turnover conditions, because the processing steps preceding the stall, that is tail insertion and the conformational switch upon substrate engagement, are not rate limiting for degradation (Figure 5B; Bard et al., 2019; Worden et al., 2017). Importantly, Rpn5-VTENKIF and Rpt6-EQ mutant proteasomes that showed significant degradation defects under non-stalled, yet otherwise identical conditions, fully regained wild-type degradation rates when restarted after the o-PA-induced deubiquitination stall (Figure 2.5B). These data indicate that tail insertion and engagement, but not the subsequent deubiquitination, unfolding, and translocation, are compromised by these mutations, likely through perturbations of the conformational equilibrium and reducing the fraction of

proteasomes in the substrate-engagement competent s1 state. The early initiation and commitment steps of degradation are thus strongly dependent on the conformational bias and dynamics of the substrate-free proteasome.

In addition to restart conditions, an increase in reaction temperature (from 20ºC to >25ºC) was able to rescue the defect in single-turnover degradation of the TAMRA-G3P substrate for the Rpt6-EQ proteasome (s2.12C), but not for the Rpn5-VTENKIF mutant (data not shown). Because a major kinetic deficit for the Rpn5-VTENKIF and Rpt6-EQ mutant proteasomes is incurred at substrate-tail insertion and engagement, degradation by these mutants is likely no longer rate-limited by mechanical unfolding and translocation, in contrast to what is observed for the wild-type proteasome (Bard et al., 2019). To address this aspect in more detail, we characterized the ubiquitin-dependent degradation of titin substrates with various thermodynamic stabilities. While wild-type proteasomes degraded the strongly destabilized FAM-titin-I27$^{V13P/V15P}$ variant significantly faster than the non-destabilized FAM-titin-I27, Rpn5-VTENKIF and Rpt6-EQ mutant proteasomes both showed only small differences in degradation for these two substrates (Figure 2.5C). These data indicate that unfolding does not represent the rate-determining step for degradation of the destabilized titin variants by the mutant proteasomes. Interestingly, the non-destabilized FAM-titin-I27 is degraded by wild-type, Rpn5-VTENKIF, and Rpt6-EQ-mutant proteasomes with comparable rates (Figure 2.5C), suggesting that thermodynamic stability of this substrate is high enough to make mechanical unfolding the common rate-limiting step for all proteasomes. Kinetic SDS-PAGE analysis of the non-destabilized FAM-titin-I27 degradation reaction showed that the decay of ubiquitinated substrate and the appearance of peptide products were anticorrelated, confirming that the observed rates for FAM-titin-I27 processing reflect true degradation and not an aberrant deubiquitination and release process (Figure s2.13B). For the Rpn5-VTENKIF and Rpt6-EQ mutant proteasomes this means that the rate-limiting step in degradation changed from initial engagement for more labile substrates to mechanical unfolding for substrates with higher thermodynamic stability. Again, these findings suggest that compromising the conformational equilibrium of the proteasome primarily affects the early steps of degradation, with no major influence on mechanical unfolding and translocation.

Discussion

Numerous structural studies of the 26S proteasome have established a suite of conformations that showed various distributions under different conditions (Matyskiela et al., 2013; Unverdorben et al., 2014; Wehmer et al., 2017; Eisele et al., 2018; Ding et al., 2017; de la Peña et al., 2018; Dong et al., 2019). Based on those studies, the conformational landscape of the proteasome can be biased by the nucleotide occupancy of the AAA+ motor (Śledź et al., 2013; Unverdorben et al., 2014; Wehmer et al., 2017; Eisele et al., 2018; Ding et al., 2017; Zhu et al., 2018) and the engagement of protein substrates (Matyskiela et al., 2013; de la Peña et al., 2018; Dong et al., 2019), but how the network of contacts within the regulatory particle, and in particular between the lid and base subcomplexes, affects conformational changes and equilibria remained unknown.

Here we report that the lid subcomplex is required for substrate processing independent of the deubiquitination activity contributed by its Rpn11 DUB. The lid subunit Rpn5, whose contact with the base ATPase ring changes dramatically during proteasome conformational changes, plays a

critical role in stabilizing the engagement-competent s1 state and coordinating the conformational switch upon substrate engagement by the AAA+ motor. The changes in the conformational landscape caused by the Rpn5-VTENKIF mutation are reminiscent of those incurred by Walker-B mutations in certain Rpt subunits (Eisele et al., 2018), for which a significant population of proteasome particles still adopt the s1 conformation, but additional substrate-engaged-like states are accessed as well. Unique to the Rpn5-VTENKIF mutant, however, is the predominance of the s2- or s5-like states, which feature a similar spiral-staircase orientation of the AAA+ motor as the engagement-competent s1 state, but have the ATPase ring and core peptidase coaxially aligned, lack the interaction between the Rpn5-VTENKIF region and Rpt3, and show the lid rotated relative to the base, with Rpn11 obstructing access to the central pore (Unverdorben et al., 2014; Eisele et al., 2018). ATP-bound wild-type proteasomes also have a fraction of molecules in the s2 conformation (Bard et al., 2018), which is likely adopted through the spontaneous release of lid-base contacts, without rearranging the AAA+ motor staircase. In contrast, the substrate-engaged proteasome conformations are characterized by a multitude of Rpt-staircase arrangements, in addition to having the base coaxially aligned with the core and the lid in a rotated position. This observation suggests that breaking the interactions between Rpn5-VTENKIF and Rpt3, and consequently rotating the lid relative to the base, are likely the first steps in the transition from s1 to substrate-processing states and prerequisites for the staircase re-arrangements of the AAA+ motor. It is conceivable that these peripheral lid-base interactions are disrupted, when several Rpt subunits grab a substrate with their pore loops during engagement and thus become more coordinated in their ATPase cycles, leading to the various spiral-staircase arrangements observed for the substrate-engaged proteasome.

We found that disrupting lid-base interactions and thereby perturbing the conformational landscape of the proteasome leads to significant degradation defects, illustrating the critical importance of the s1 state for substrate-tail insertion and degradation initiation. Previously, we assessed the dependence of substrate engagement on the s1 state by inducing engaged-like conformations through the addition of ATPγS (Bard et al., 2019). However, in these studies it could not be completely ruled that, in addition to the conformational bias, shutting down the ATPase motor with the non-hydrolyzable ATP analog also played a role in causing the observed tail-insertion defects. The Rpn5-VTENKIF mutant proteasome characterized here contains a completely unmodified ATPase ring and mutations in Rpn5 that are relevant for subunit interactions exclusively in the s1 state. That this mutant shows strongly compromised degradation initiation therefore provides important new evidence for the s1-state requirement of substrate engagement and the critical role of proteasome conformational changes in coordinating the individual steps of substrate processing. While our EM snapshot of the conformational distribution revealed that Rpn5-VTENKIF mutant proteasomes still retain a considerable fraction of particles in the s1 state, weakening the lid-base interactions may strongly affect the dynamics of conformational switching and shorten the time proteasomes spend in the s1 state. Recent work established a kinetic-gateway model for substrate entry into the proteasome, in which only sufficiently long and complex tails on a substrate are able to enter the central pore of s1-state proteasomes and trigger the conformational switch to substrate-processing states for degradation (Bard et al., 2019). Shortening the life time of the s1 conformer would therefore disrupt this substrate-selection mechanism, interfere with degradation initiation, and lead to major degradation defects, as we observed here. This model does not only apply to the disruption of lid-base contacts, but also to the stabilization of substrate-processing states, for instance by trapping Rpt subunits with bound ATP or ATPγS, which may thus explain the differential degradation defects previously reported for the various Walker-B mutants (Eisele et al., 2018; Beckwith et al., 2013). In both the s1 and s2 states of substrate-free proteasomes, the ATP-

binding pocket of Rpt6 is open and ADP-bound, and the Rpt6-Rpt3 interface acts as the seam in the spiral-staircase arrangement of ATPase subunits, with Rpt3 at the top and Rpt2 at the bottom (Figure 2.3A). In the substrate-processing conformations, however, the Rpt6 pocket is ATP-bound and closed, and may only transiently open up for nucleotide exchange during processive ATP hydrolysis and substrate translocation, similar to all other ATPase subunits in the hexamer (Figure 2.3A). Eliminating ATP hydrolysis in Rpt6 therefore biases the proteasome away from the s1 and s2/s5 states, towards substrate-engaged like conformations (Eisele et al., 2018), and is expected to inhibit the progression of the hexamer's sequential ATPases cycle at a stage when the neighboring Rpt3 subunit is in the bottom position of the spiral staircase (Figure 2.6). That trapping Rpt4 with bound ATP also shifts the conformational equilibrium away from the engagement-competent s1 state is somewhat surprising, given that Rpt4's ATPase pocket at the interface with Rpt5 is already closed and ATP-bound in the substrate-free s1 state. Despite their correct assembly into 26S holoenzymes with robust peptidase, ATPase, and deubiquitination activities, Rpt4-EQ mutant proteasomes are degradation-incompetent, which explains the previously described lethality of this mutant in yeast (Eisele et al., 2018) and highlights the importance of the Rpt4 ATPase pocket for proteasome function. It remains unclear whether the degradation defects of the Rpt4-EQ mutant primarily originate from a perturbed conformational equilibrium that may be more completely or irreversibly shifted to engagement-incompetent non-s1 states, or whether other degradation steps besides initiation are compromised as well.
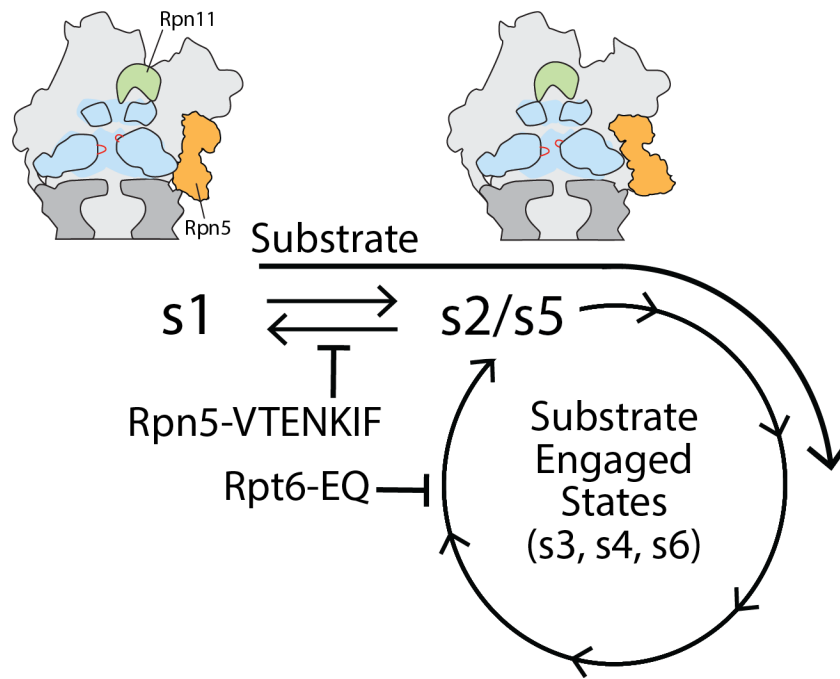

Figure 2.6. Model for coupling between proteasome conformations and substrate degradation.
In the s1 conformation, Rpn11 is offset from the central pore, which is therefore accessible for substrate entry and engagement by the AAA+ motor. In the s2/s5 and substrate-engaged states of the proteasome, Rpn11 is coaxially aligned with the continuous processing channel and obstructs the entrance to the AAA+ motor, inhibiting access for substrates that are not yet engaged. Insertion of a substrate's flexible initiation region in the s1 state induces the transition to substrate-engaged conformations. Rpn5-VTENKIF and Rpt6-EQ mutations bias the conformational landscape away from the s1 state, either by destabilizing s1 or trapping substrate-engaged-like states through ATPase inhibition, and therefore interfere with substrate engagement.

For the Rpt6-EQ mutant we observed full rescue of degradation defects when proteasomes were restarted after stalling them prior to substrate deubiquitination, indicating that only substrate-tail insertion and engagement by the AAA+ motor were affected by the mutation. The Rpt6-EQ mutant proteasome was previously shown by cryo-EM to adopt substrate-engaged like conformations in the absence of substrate (Eisele et al., 2018), which is further supported by their elevated, ATPγS-insensitive core gate-opening activity, their stimulated ATPases rates that are non-responsive to ubiquitin-bound Ubp6, and their increased Ubp6-DUB activity. In agreement with the idea that conformational switching is primarily driven by the nucleotide states and hydrolysis in the motor, the core gate-opening effects contributed by Rpt4-EQ and Rpt6-EQ mutations were unaffected by the addition of the Rpn5-VTENKIF mutation in lid. Conversely, the Rpn5-VTENKIF mutation at the lid-base interface was dominating the degradation defects when combined with Rpt6-EQ, which can be explained if these two mutants have intrinsically different dynamics of conformational switching. This hypothesis could also explain the temperature-dependent phenotype that is presented by Rpt6-EQ mutant proteasome, but not the Rpn5-VTENKIF variant (Figure s2.12C). It is possible that the Rpt6-EQ mutant has reduced conformational switching dynamics in the absence of substrate, because accessing the s1 conformation would require expulsion of unhydrolyzed ATP from the Walker-B mutant Rpt6 site. Indeed, Rpt6-EQ proteasomes in the s1 conformation lacks nucleotide in the binding pocket of Rpt6 (Eisele et al. 2018). The ATPase rate of molecular machines has been observed to follow Arrhenius behavior (Gruber et al., 2017; Martin et al., 2018), and the conformational switching dynamics of the Rpt6-EQ mutant may be stimulated at higher temperatures by faster ATP hydrolysis in the other Rpt subunits, leading to more frequent expulsion of ATP from Rpt6, adoption of the s1 conformation, and thus restoration of wild-type-like degradation activity.

In summary, the detailed characterization of Rpn5-VTENKIF and Rpt6-EQ mutant proteasomes provides insight into the network of interactions within the regulatory particle that govern the crucial conformational switch during degradation. Both mutants highlight the critical importance of the s1 state being populated long enough for substrate-tail insertion and engagement, before the conformational switch to substrate-processing states enables processive threading, mechanical unfolding, co-translocational deubiquitination, and substrate transfer into the 20S core for proteolytic cleavage. While these mutations give rise to similar degradation defects, they are located in distant regions of the proteasome and affect the conformational switching in distinct ways. The Rpn5-VTENKIF mutation disrupts critical lid-base interactions, destabilizes the s1 state, and causes a spontaneous re-equilibration of proteasome conformations. In contrast, the Rpt6-EQ mutation stabilizes substrate-processing states and inhibits the sequential progression of the ATPase hydrolysis cycle in the hexamer, thereby pulling the conformational equilibrium away from the s1 state. These alternative ways of shifting the conformational landscape to influence substrate turnover hints to the numerous possibilities for regulatory fine-tuning of proteasomal degradation through posttranslational modifications or binding partners, such as Ubp6 (Bashore et al., 2015; Aufderheide et al., 2015). There is already a growing number of factors and site-specific modifications of the base and lid subcomplexes that are known to affect proteasome activities and are coupled to conformational switching (VerPlank and Goldberg, 2017; VerPlank et al., 2019). Furthermore, modulating the conformational equilibria through proteasome-interacting effectors could differentially influence the turnover of only specific substrate pools in the cell, as illustrated by our observations that the Rpn5-VTENKIF and Rpt6-EQ mutations led to a range of degradation defects depending on the substrate identity. Given the extensive structural and functional conservation of 26S proteasomes between yeast and humans (Bard et al., 2018; Finley et al., 2016;

Kachroo et al., 2015), we expect this mechanism of conformational regulation to be conserved among eukaryotic proteasomes.

Materials and Methods

Key resources table

Reagent type (species) or resource	Designation	Source or reference	Identifiers	Additional information
Recombinant DNA reagent	pET-Duet Rpn1, Rpn2, Rpn13	(Beckwith et al., 2013)	pAM81	
Recombinant DNA reagent	pACYC-Duet RIL Nas6, Hsm3, Rpn14, Nas2	(Beckwith et al., 2013)	pAM83	
Recombinant DNA reagent	pCOLA FLAG-Rpt1, Rpt2, His_6-Rpt3, Rpt5, Rpt6, Rpt4	(Beckwith et al., 2013)	pAM82	
Recombinant DNA reagent	pCOLA FLAG-Rpt1-191TAG, Rpt2, His_6-Rpt3, Rpt5, Rpt6, Rpt4	(Bard et al., 2019)	pAM88	
Recombinant DNA reagent	Synthetase pEVOL mod.	(Bard et al., 2019) (Worden et al., 2017)	pAM183	
Recombinant DNA reagent	pCOLA FLAG-Rpt1, sspB permutant-Rpt2, His_6-Rpt3, Rpt5, Rpt6, Rpt4	(Bashore et al., 2015)	pAM210	
Recombinant DNA reagent	pCOLA FLAG-Rpt1-EQ, Rpt2, His_6-Rpt3, Rpt5, Rpt6, Rpt4	(Beckwith et al., 2013)	pAM204	
Recombinant DNA reagent	pCOLA FLAG-Rpt1, Rpt2-EQ, His_6-Rpt3, Rpt5, Rpt6, Rpt4	(Beckwith et al., 2013)	pAM205	
Recombinant DNA reagent	pCOLA FLAG-Rpt1, Rpt2, His_6-Rpt3-EQ, Rpt5, Rpt6, Rpt4	(Beckwith et al., 2013)	pAM209	
Recombinant DNA reagent	pCOLA FLAG-Rpt1, Rpt2, His_6-Rpt3, Rpt5, Rpt6, Rpt4-EQ	(Beckwith et al., 2013)	pAM206	
Recombinant DNA reagent	pCOLA FLAG-Rpt1, Rpt2, His_6-Rpt3, Rpt5-EQ, Rpt6, Rpt4	(Beckwith et al., 2013)	pAM207	
Recombinant DNA reagent	pCOLA FLAG-Rpt1, Rpt2, His_6-Rpt3, Rpt5, Rpt6-EQ, Rpt4	(Beckwith et al., 2013)	pAM208	
Recombinant DNA reagent	pCOLA MBP-HRV3C-Rpt1, Rpt2, His_6-HRV3C-Rpt3, Rpt5, Rpt6-EQ, Rpt4	This study	pAM214	This plasmid encodes HRV3C cleavable affinity tags to make tagless recombinant base.
Recombinant DNA reagent	His_6-Ubp6	(Bashore et al., 2015)	pAM211	
Recombinant DNA reagent	His_6-Ubp6 C118A	(Bashore et al., 2015)	pAM212	

Reagent type (species) or resource	Designation	Source or reference	Identifiers	Additional information
Recombinant DNA reagent	MGCS-titin I27 ^{V15P}(lysineless)-ssrA-1K-35 amino acid tail including PPPY and His$_6$	(de la Peña et al., 2018)	pAM213	
Recombinant DNA reagent	titin I27$^{V13P/V15P}$(lysineless)-PPPY-ssrA-1K-35 amino acid tail containing ssrA	(Bard et al., 2019)	pAM94	
Recombinant DNA reagent	titin I27^{V15P}(lysineless)-PPPY-ssrA-1K-35 amino acid tail	(Bard et al., 2019)	pAM91	
Recombinant DNA reagent	titin I27 (lysineless)-PPPY-ssrA-1K-35 amino acid tail	(Bard et al., 2019)	pAM93	
Recombinant DNA reagent	His$_6$-thrombin-N1-G3P(lysineless)−1 K-54 amino acid tail including ssrA, PPPY, C-terminal lysineless StrepII tag.	(Worden et al., 2017)	pAM77	
Recombinant DNA reagent	His$_6$-SUMO-Ub$_4$	(Bard et al., 2019)	pAM102	
Recombinant DNA reagent	pET lid wild-type (Rpn5, MBP-HRV3C-Rpn6, Rpn8, Rpn11, Rpn9)	(Bard et al., 2019)	pAM85	
Recombinant DNA reagent	pET lid VTENKIF (Rpn5-VTENKIF, MBP-HRV3C-Rpn6, Rpn8, Rpn11, Rpn9)	This study	pAM203	This plasmid encodes a cleavable MBP tag on Rpn6 and is used to make tagless Rpn5-VTENKIF lid.
Recombinant DNA reagent	pCOLA (His$_6$-HRV3C-Rpn12, Rpn7, Rpn3)	(Bard et al., 2019)	pAM86	
Recombinant DNA reagent	pACYC Sem1, Hsp90	(Lander et al., 2012)	pAM80	
Recombinant DNA reagent	pRS305 His$_{10}$-HRV3C-RPN5	This study	pAM198	This plasmid encodes an *S. cerevisiae* integratableRpn5 gene with endogenous promotors and a cleavable N-terminal histidine tag on Rpn5.
Recombinant DNA reagent	pRS305 His$_{10}$-HRV3C-rpn5-vtenkif-aaaaaaa	This study	pAM199	This plasmid encodes an *S. cerevisiae* integratable Rpn5-VTENKIF gene with endogenous promotors and a cleavable N-terminal histidine tag on Rpn5.
Recombinant DNA reagent	pRS305 3 × FLAG-HRV3C-RPN5	This study	pAM200	This plasmid encodes an *S. cerevisiae* integratable Rpn5 gene with endogenous promotors and a cleavable N-terminal FLAG tag on Rpn5.
Recombinant DNA reagent	pRS305 3 × FLAG-HRV3C-rpn5-vtenkif-aaaaaaa	This study	pAM201	This plasmid encodes an *S. cerevisiae* integratable Rpn5-VTENKIF gene with endogenous promotors and a cleavable N-terminal FLAG tag on Rpn5.
Recombinant DNA reagent	pRS316 RPN6 promoter-RPN5-RPN5 terminator	This study	pAM202	This plasmid encodes the Rpn5 ORF with a Rpn6 promotor and Rpn5

Reagent type (species) or resource	Designation	Source or reference	Identifiers	Additional information
				terminator on an *S. cerevisiae* counter-selectable, non-integrating plasmid.
Strain, strain background *E. coli*	BL21(DE3)	Thermofisher	Cat#C601003	
Strain, strain background *S. cerevisiae*	MATa ade2-1 his3-11,15 leu2-3,112 trp1-1 ura3-1 can1-100 bar1 PRE1::PRE1−3 × FLAG(KANMX6)	(Beckwith et al., 2013)	yAM54	
Strain, strain background *S. cerevisiae*	MATa ade2-1, his3-11,15, LEU2::His$_{10}$-HRV3C-RPN5, trp1-1, ura3-1, can1-100, RPN11::RPN11-3XFLAG (HIS3)	This study	yAM99	This strain bears pAM198 integrated at LEU2 in an 3X-FLAG Rpn11 background.
Strain, strain background *S. cerevisiae*	MATa ade2-1, his3-11,15, LEU2::His$_{10}$-HRV3C-rpn5-vtenkif-aaaaaaa, trp1-1, ura3-1, can1-100, RPN11::RPN11-3XFLAG (HIS3)	This study	yAM100	This strain bears pAM199 integrated at LEU2 in an 3X-FLAG Rpn11 background.
Strain, strain background *S. cerevisiae*	MATa ade2-1 his3-11,15,112 trp1-1 ura3-1 can1-100 bar1 rpn5Δ::NATMX6, pRS316-promoter-RPN6-RPN5-terminator-RPN6	This study	yAM96	This strain has endogenous Rpn5 deleted and replaced with NATMX6 with pAM202 as a covering plasmid in a W303 background.
Strain, strain background *S. cerevisiae*	MATa ade2-1 his3-11,15 trp1-1 ura3-1 can1-100 bar1 rpn5Δ::NATMX6, LEU2::3 × FLAG-HRV3C-RPN5	This study	yAM97	This strain bears pAM200 integrated at LEU2 in a yAM96 background.
Strain, strain background *S. cerevisiae*	MATa ade2-1 his3-11,15 trp1-1 ura3-1 can1-100 bar1 rpn5Δ::NATMX6, LEU2::3 × FLAG-HRV3C-rpn5-vtenkif-aaaaaaa	This study	yAM98	This strain bears pAM201 integrated at LEU2 in a yAM96 background.
Antibody	Polyclonal rabbit anti-Rpn5	Abcam	Cat#ab79773	Dilution (1:5000)
Antibody	Polyclonal rabbit anti-Nas6	Abcam	Cat#ab91447	Dilution (1:5000)
Antibody	Monoclonal Goat anti-rabbit IgG-HRP	Bio-Rad	170–6515	Dilution (1:10000)
Peptide, recombinant protein	Fluorescein-HHHHHHLPETGG	Genscript	Custom ordered	
Peptide, recombinant protein	Bovine Serum Albumin	Sigma Aldrich	Cat#A9418	
Software	UCSF Chimera	UCSF	https://www.cgl.ucsf.edu/chimera/	
Software	Origin Pro	Origin Lab	https://www.originlab.com/	
Software	ImageQuant	GE	ImageQuant TL 8.1	
Chemical compound	Cy3 DBCO	Click Chemistry Tools	Cat#A140	
Chemical compound	Fluorescein-5-maleimide	ThermoFisher	Cat#62245	
Chemical compound	Cy5 Maleimide	Lumiprobe	Cat#23380	
Chemical compound	4-azido-L-phenylalanine	Amatek Chemical	Cat#A-7137	
Chemical compound	1,10-phenanthroline	Sigma Aldrich	Cat#P9375	

Strain construction

Strains yAM96, yAM97, and yAM98 were constructed using standard techniques. A W303-derived parental strain was transformed with a pRS316-RPN5 (pAM202) covering plasmid and then transformed with a PCR product containing homologous regions flanking the RPN5 gene and containing the NATMX marker (Goldstein and McCusker, 1999; Longtine et al., 1998). RPN5 disruption was confirmed by PCR and sequencing of both the 5' and 3' junctions of the NATMX integration. RPN5 and rpn5-vtenkif-aaaaaaa were introduced by integration of pRS305 vectors containing promoter and terminator from Rpn5 that had been linearized in the LEU2 marker. Curing of the covering plasmid was performed twice sequentially on plates containing 5-FOA and confirmed by loss of growth on dropout URA plates. yAM99 and yAM100 strains were also constructed using standard techniques. The YYS40 (Sone et al., 2004) parental strain bearing RPN11::3X-FLAG-RPN11 (HIS3) was transformed with pRS305 linearized at the LEU2 marker and containing either 10X-Histag-HRV3C-RPN5 or 10X-Histag-HRV3C-rpn5-vtenkif-aaaaaaa. Integration was confirmed by PCR.

Protein purification
Purification of the tagged heterologous base and SspB-fused base

Preparation of the *Saccharomyces cerevisiae* base subcomplex was conducted as described previously (Bard and Martin, 2018; Bashore et al., 2015; Beckwith et al., 2013; Worden et al., 2017). BL21-star (DE3) *E. coli* cells were transformed and grown in 3L of terrific broth, shaking at 37°C until OD_{600} ~0.8–1.0 was reached. Temperature was lowered to 30°C and protein expression was induced with 1 mM IPTG for 5 hr at 30°C, followed by overnight expression at 16°C. Cells were harvested by centrifugation and resuspended in base lysis buffer (60 mM HEPES pH 7.6, 50 mM NaCl, 50 mM KCl, 10 mM $MgCl_2$, 5% glycerol, 2 mM ATP, + 2 mg/mL lysozyme, proteasome inhibitors (PMSF, Aprotonin, Leupeptin, PepstainA), and benzonase, and then stored at −80°C. For the purification, cells were thawed and lysed by sonication. Lysate was clarified by centrifugation and loaded onto a HisTrap High-Performance 5 mL columns (GE Healthcare) using a peristaltic pump, washed with base NiA buffer (60 mM HEPES pH 7.6, 50 mM NaCl, 50 mM KCl, 10 mM $MgCl_2$, 5% glycerol, 2 mM ATP + 20 mM imidazole), and eluted with base NiB buffer (60 mM HEPES pH 7.6, 50 mM NaCl, 50 mM KCl, 10 mM $MgCl_2$, 5% glycerol, 2 mM ATP, 250 mM imidazole). Eluates were then flowed over M2 ANTI-FLAG affinity resin (Sigma) and eluted with 0.5 mg/mL 3X FLAG peptide (Genscript) in base lysis buffer. Base subcomplex was further purified by size-exclusion chromatography using a Superose 6 increase 10/300 column (GE Healthcare) pre-equilibrated with base GF buffer (60 mM HEPES pH 7.6, 50 mM NaCl, 50 mM KCl, 10 mM $MgCl_2$, 5% glycerol, 0.5 mM TCEP, 1 mM ATP). Peak fractions corresponding to assembled base subcomplex were concentrated, flash frozen in liquid nitrogen, and stored at −80°C. The concentration of base was determined by Bradford protein assay using bovine serum albumin (BSA) as a standard.

Purification and labeling of base containing unnatural amino acid

Preparation of 4-azidophenylalanine-containing base subcomplex was conducted as detailed previously (Bard et al., 2019; Bard and Martin, 2018). BL21star (DE3) *E. coli* were cultured overnight in 2xYT media and diluted into prewarmed media containing antibiotics (300 μg/mL Ampicillin, 25

μg/mL Chloramphenicol, 50 μg/mL kanamycin, and 100 μg/mL spectinomycin). Cells were grown with shaking to OD_{600} = 0.6 before pelleting and resuspending, pooling 6L of cells into 1L of buffered TB containing 2 mM 4-azidophenylalanine, 17 mM KH_2PO_4, and 72 mM K_2HPO_4 at 30°C. After 30 min, protein expression was induced with 1 mM IPTG for 5 hr, followed by overnight incubation with shaking at 16 °C.

Following centrifugation, cells were resuspended in base lysis buffer, and purification was performed as described above for heterologously expressed base until elution from FLAG affinity column. After elution from M2 ANTI-FLAG affinity resin (Sigma), artificial amino acid-containing base was incubated at room temperature with 150 μM 5,5'-dithiobis-2-nitrobenzoic acid for 10 min before chilling on ice and adding 300 μM DBCO-Cy3 (Click Chemistry Tools) and incubating at 4°C overnight. Following overnight labeling, the reaction was quenched with 10 mM DTT and subjected to size-exclusion chromatography on a Superose 6 Increase 10/300 (GE Healthcare) in GF buffer, as described for other base constructs above. Base concentration was determined by Bradford protein assay using BSA as a standard, while the extent of Cy3 labeling was determined by absorbance at 555 nm, and SDS-PAGE was used to confirm labeling of only Rpt1 as well as complete removal of free dye.

Purification of the heterologously expressed tagless base subcomplex

Preparation of recombinantly expressed, tagless *S. cerevisiae* base subcomplex was conducted using standard affinity-chromatography and size-exclusion chromatography protocols. Briefly, BL21-star (DE3) *E. coli* cells were grown in 3L of terrific broth shaking at 37°C until OD_{600} ~0.8–1.0 was reached. Temperature was lowered to 30°C and protein expression was induced with 1 mM IPTG for 5 hr at 30°C, followed by overnight expression at 16°C. Cells were harvested by centrifugation and resuspended in base lysis buffer (60 mM HEPES pH 7.6, 50 mM NaCl, 50 mM KCl, 10 mM $MgCl_2$, 5% glycerol, 2 mM ATP, + 2 mg/mL lysozyme, proteasome inhibitors (PMSF, Aprotonin, Leupeptin, PepstainA), and benzonase, and then stored at −80°C. For the purification, cells were thawed and lysed by sonication. Lysate was clarified by centrifugation and loaded onto HisTrap High-Performance 5 mL (GE Healthcare) columns using a peristaltic pump, washed with base NiA buffer (60 mM HEPES pH 7.6, 50 mM NaCl, 50 mM KCl, 10 mM $MgCl_2$, 5% glycerol, 2 mM ATP + 20 mM imidazole), and eluted with base NiB buffer (60 mM HEPES pH 7.6, 50 mM NaCl, 50 mM KCl, 10 mM $MgCl_2$, 5% glycerol, 2 mM ATP, 250 mM imidazole). Eluates were flowed over Amylose Resin (NEB), washed with base GF buffer (60 mM HEPES pH 7.6, 50 mM NaCl, 50 mM KCl, 10 mM $MgCl_2$, 5% glycerol, 0.5 mM TCEP, 2 mM ATP), and eluted with base GF buffer + 10 mM maltose + ATP regeneration system (creatine kinase and creatine phosphate). HRV3C protease was added to the Amylose eluate and cleavage was allowed to proceed for 45 min at room temperature or overnight at 4°C. The Amylose resin eluate was concentrated and loaded onto a Superose 6 increase 10/300 size exclusion column equilibrated with base GF buffer. Peak fractions corresponding to assembled base were concentrated, flash frozen, and stored at −80°C. The concentration of base was determined by Bradford protein assay using BSA as a standard.

Purification of Rpn10, core particle, Ubp6, Ubp6 C118A, *M. musculus* Uba1, *S. cerevisiae* Ubc4, *S. cerevisiae* Rsp5, ubiquitin, and linear ubiquitin tetramer

Rpn10, core particle, *M. musculus* Uba1, Ubc4, Rsp5, and ubiquitin were prepared as described in Worden et al. (2017) using standard expression and purification procedures (Bashore et al.,

2015; Worden et al., 2017; Bard and Martin, 2018). Purification of Ubp6 and Ubp6-C118A was performed as described (Bashore et al., 2015), and linear ubiquitin tetramer was purified exactly as described (Bard et al., 2019).

Purification of His$_{10}$-HRV3C-Rpn5-VTENKIF mutant and wild-type 26S holoenzymes

Yeast strains yAM99 (wild type Rpn5) and yAM100 (mutant Rpn5) were grown in 3L of YPD for 3 days at 30°C. Cells were harvested by centrifugation, weighed, and resuspended in 15 mL of 26S lysis buffer (60 mM HEPES pH 7.6, 25 mM NaCl, 10 mM MgCl$_2$, 2.5% glycerol, 5 mM ATP + ATP regeneration (creatine kinase and creatine phosphate)). Resuspended cells were flash frozen in liquid nitrogen, lysed by cryo grinding, and stored at −80°C. Lysed yeast powder was thawed at room temperature and diluted in 26S lysis buffer to 1.5 mL buffer per gram of yeast. Lysate was clarified by centrifugation and bound in batch to M2 ANTI-FLAG affinity resin (Sigma) for 1 hr at 4°C. FLAG resin was subsequently washed in batch twice with 25 mL of 26S lysis buffer, applied to a gravity flow column, and washed with an additional 25 mL of 26S lysis buffer. Proteasome was eluted with 26S lysis buffer + 0.5 mg/mL 3X FLAG peptide. FLAG eluate was loaded onto a 1 mL HisTrap High-Performance 5 mL columns (GE Healthcare) using a peristaltic bump and washed with five column volumes of 26S NiA buffer (30 mM HEPES pH 7.6, 10 mM MgCl$_2$, 10% glycerol, 5 mM ATP, 10 mM imidazole). Proteasome was eluted with 26S NiB buffer (30 mM HEPES pH 7.6, 10 mM MgCl$_2$, 10% glycerol, 5 mM ATP, 500 mM imidazole). HRV3C protease was added in excess, and cleavage was allowed to proceed for 30 min at 4°C. 26S proteasome was concentrated and loaded onto a Superose 6 increase 10/300 size exclusion column pre-equilibrated with 26S GF buffer (60 mM HEPES pH 7.6, 25 mM NaCl, 10 mM MgCl$_2$, 2.5% glycerol, 1 mM ATP, 0.5 mM TCEP). Peak fractions were spiked with ATP regeneration (creatine kinase and creatine phosphate), concentrated, flash frozen in liquid nitrogen, and stored at 80°C. 26S holoenzyme concentration was determined by Bradford protein assay using BSA as a standard for total protein and in-gel quantification using purified Rpn1 as an internal standard for total regulatory particle.

Purification of FLAG-HRV3C-Rpn5 mutant and wild-type 26S holoenzymes

Yeast strains yAM97 (wild type Rpn5) and yAM98 (mutant Rpn5) were grown in 3L of YPD for 3 days at 30°C. Cells were harvested by centrifugation, weighed, and resuspended in 15 mL of 26S lysis buffer (60 mM HEPES pH 7.6, 25 mM NaCl, 10 mM MgCl$_2$, 2.5% glycerol, 5 mM ATP + ATP regeneration (creatine kinase and creatine phosphate)). Resuspended cells were flash frozen in liquid nitrogen, lysed by cryo grinding (SPEX Freezer/Mill), and stored at −80°C. Lysed yeast powder was thawed at room temperature and diluted in 26S lysis buffer to 1.5 mL buffer per gram of yeast. Lysate was clarified by centrifugation and bound in batch to M2 anti-FLAG affinity resin (Sigma) for 1 hr at 4°C. FLAG resin was subsequently washed in batch twice with 25 mL of 26S lysis buffer, applied to a gravity flow column, and washed with an additional 25 mL of 26S lysis buffer. 26S proteasome was eluted with 26S lysis buffer + 0.5 mg/mL 3X FLAG peptide (Genscript). FLAG eluate was cleaved with HRV protease added in excess, and cleavage was allowed to proceed for 30 min at 4°C. 26S proteasome was concentrated and loaded onto a Superose 6 increase 10/300 size-exclusion column pre-equilibrated with 26S GF buffer (60 mM HEPES pH 7.6, 25 mM NaCl, 10 mM MgCl$_2$, 2.5% glycerol, 1 mM ATP, 0.5 mM TCEP). Peak fractions were spiked with ATP regeneration system (creatine kinase and creatine phosphate), concentrated, flash frozen in liquid nitrogen, and stored at −80°C. 26S holoenzyme concentration was determined by Bradford protein

assay using BSA as a standard for total protein and in-gel quantification using purified Rpn1 as a standard for total regulatory particle.

Purification of the heterologous lid

Heterologous expression and purification of the *Saccharomyces cerevisiae* lid subcomplex was performed similarly to previous studies (Bard et al., 2019). BL21-star (DE3) *E. coli* cells were grown in 2L of terrific broth medium shaking at 37°C until an OD_{600} ~1.0–1.5 was achieved. Protein expression was induced with 1 mM IPTG overnight at 18°C. Cells were harvested by centrifugation and resuspended in lid lysis buffer (60 mM HEPES pH 7.6, 25 mM NaCl, 10 mM $MgCl_2$, 2.5% glycerol + 2 mg/mL lysozyme, proteasome inhibitors (PMSF, Aprotonin, Leupeptin, PepstainA), and benzonase, and then stored at −80°C. For purification, cells were thawed and lysed by sonication. Lystate was clarified by centrifugation and loaded onto HisTrap High-Performance 5 mL columns (GE Healthcare) using a peristaltic pump, washed with lid NiA buffer (60 mM HEPES pH 7.6, 25 mM NaCl, 10 mM $MgCl_2$, 2.5% glycerol + 20 mM imidazole), and eluted with lid NiB buffer (60 mM HEPES pH 7.6, 25 mM NaCl, 10 mM $MgCl_2$, 2.5% glycerol, 250 mM imidazole). Eluates were flowed over Amylose Resin (NEB), washed with lid GF buffer (60 mM HEPES pH 7.6, 25 mM NaCl, 10 mM $MgCl_2$, 2.5% glycerol, 0.5 mM TCEP), and eluted with lid GF buffer + 10 mM maltose. HRV3C protease was added to the Amylose eluate and cleavage was allowed to proceed overnight at 4°C or at room temperature for 2 hr. Amylose resin eluate was concentrated and loaded onto a Superose 6 increase 10/300 size-exclusion column equilibrated with GF buffer. Peak fractions corresponding to assembled lid were concentrated, flash frozen, and stored at −80°C.

Substrate preparation and ubiquitination

G3P substrate preparation and labeling was performed as described previously (Worden et al., 2017), and the titin-I27$^{V13P/V15P}$, titin-I27^{V15P}, and titin-I27 substrates were purified and labeled as described (Bard et al., 2019; de la Peña et al., 2018). Ubiquitination reactions were carried out as described previously (Bard et al., 2019; de la Peña et al., 2018; Myers et al., 2018). Briefly, 10–20 µM substrate protein was incubated with 2 µM mouse E1 enzyme (mE1), 5 µM Ubc4, and 5 µM Rsp5 with 450–800 µM ubiquitin and 6–10 mM ATP in 25 mM HEPES pH 8.0, 150 mM NaCl, 5% glycerol at 25°C until completion (assessed by SDS-PAGE, 30–180 min). Ubiquitination reaction conditions were screened for uniform higher molecular weights and full non-ubiquitinated substrate depletion by SDS-PAGE.

Native polyacrylamide gel electrophoresis of purified assembled proteasomes

Proteasomes were reconstituted with 1 µM core particle and 2 µM base, lid, and Rpn10 in GF buffer with 5 mM ATP, 0.5 mM TCEP, and ATP regeneration system, and allowed to assemble for 5 min at room temperature. Equivalent amounts of reconstituted proteasomes were diluted appropriately in 5X native gel sample buffer (250 mM Tris*HCl pH 7.5, 50 mM $MgCl_2$, 1 mM ATP, 50% glycerol, 0.015% w/v xylene cyanol) and loaded onto 4% native polyacrylamide gels with 1 mM ATP and a 3% polyacrylamide stacking gel containing 2.5% sucrose and 1 mM ATP. Samples were electrophoresed at 100 V and 4°C for 4 hr as described (Elsasser et al., 2005). In-gel peptidase activity was assayed by incubating the gel in GF buffer with 5 mM ATP, 0.5 mM TCEP, and 100 µM Suc-LLVY-AMC with or without 0.02% SDS for 10 min before imaging on a Chemidoc MP Imaging System (Bio-Rad). The same gel was subsequently fixed and Coomassie stained for

detection of total protein. Where indicated, samples from reconstitutions were further diluted in 2X SDS-PAGE sample buffer, electrophoresed under denaturing conditions, and imaged as a loading control.

Negative-stain transmission electron microscopy

Wild-type *S. cerevisiae* 26S holoenzyme was diluted to ~400 nM in a buffer (60 mM HEPES, pH 7.6, 25 mM NaCl, 10 mM MgCl2, 1 mM TCEP) supplemented with 6 mM ATP or 2 mM ATPγS. 4 μL of the ATP- or ATPγS-containing solution were applied to a plasma treated (Electron Microscopy Sciences) carbon film supported by a Maxtaform 400 mesh Cu/Rh grid (TED PELLA). After incubation for 45 s, excess solution was wicked with Whatman #1 filter paper and immediately treated with a 2% (w/v) solution of uranyl formate stain. Excess stain was removed by wicking, and the grids were allowed to dry for 10 min before visualization by transmission electron microscopy. The same dilution, blotting, and staining approach was used for a solution containing Rpn5-VTENKIF-mutant 26S holoenzyme purified as described above.

Data were acquired with the Leginon automation software and a Tecnai F20 transmission electron microscope (FEI) operated at 200 keV with an under-focus range of 0.5–1.0 μm. A total fluence of 30 e⁻/ Å² was used to collect ~800 micrographs for each of the 26S holoenzyme variants in ATP or ATPγS with an Eagle 4 k CCD camera (FEI) at a nominal magnification of 62,000x and amplified pixel size of 1.79 Å. Approximately 800 micrographs were processed for each of the four datasets using single particle analysis (SPA) with RELION 3.0b3. The extracted particles were subject to the same SPA workflow (Figure 2—figure supplement 1B) with a final 3D classification step into six classes to quantify the degree of heterogeneity present in each dataset (Figure s2.3-2.9, Figure 2.2A). Proteasome conformational state for each class was determined for each state using UCSF Chimera's 'Fit in Map' tool comparing each class to the atomic models in Eisele et al. (2018).

Anti-FLAG pulldown of assembled proteasome complexes

Proteasomes were reconstituted with 500 nM core particle and 1 μM tagless base, lid, and Rpn10, and allowed to assemble for 5 min in GF buffer with 1 mg/mL BSA, 5 mM ATP, and ATP regeneration system at room temperature. Magnetic ANTI-FLAG m2 resin (Sigma) was added to the solution and resin binding was allowed to proceed at 4°C for 1 hr. Resin was washed three times with 120 μL of GF buffer including 1 mg/mL BSA and 5 mM ATP, before eluting bound complexes with 35 μL of GF buffer supplemented with 5 mM ATP and 1 mg/mL 3X FLAG peptide at 30°C for 30 min.

Immunoblot analysis

SDS-PAGE gels including Precision Plus Stained protein standards (Thermo Fisher) were transferred to activated 0.2 μm PVDF membrane (Thermo Scientific) via semi-dry transfer in (25 mM Tris-HCl pH 8.3, 192 mM glycine, 5% methanol) for 45 min using constant 80 mA current before membrane blocking with 5% milk in TBST (50 mM Tris-HCl pH 7.6, 150 mM NaCl, 0.05% Tween-20) for at least one hour. Blocked membranes were probed with primary antibody (diluted in TBST with 5% milk) for at least 1 hr before being washed with TBST and re-probed with secondary anti-Rabbit-HRP for at least 30 min. Membranes were subsequently washed three times with TBST (15 min each) before visualization of Chemiluminescence activity using Western Lightning ECL

reagent (Perkin Elmer) in Chemidoc MP Imaging System (Bio-Rad) with exposure times ranging from 30 to 120 s.

ATPase activity measurements

ATP-hydrolysis rates were determined using an NADH-coupled assay (pyruvate kinase and lactate dehydrogenase) as described previously (Beckwith et al., 2013; Bashore et al., 2015). Briefly, proteasomes were reconstituted under base-limiting conditions with 200 nM base of the indicated mutant, 800 nM core, 800 nM lid, and 1 μM Rpn10 in GF buffer with 5 mM ATP and 0.5 mM TCEP at room temperature for 5 min, before being 2-fold diluted into ATPase mix (final concentrations: 1 mM NADH, 5 mM ATP, 7.5 mM phosphoenolpyruvate, 3 U/mL pyruvate kinase, and 3 U/mL lactate dehydrogenase), applied to a 384-clear bottom plate (Corning), and centrifuged at (1000 x g) for 1 min prior to measurement. Steady-state depletion of NADH was assessed by measuring the absorbance at 340 nm in a Synergy Neo2 Multi-Mode Plate Reader (Biotek). Solution pathlength was manually determined per experiment through titration of NADH and used to calculate ATPase rate.

For ATPase response to ubiquitin-bound Ubp6, measurements were performed as described above, using Rpn10-ΔUIM rather than full length Rpn10 and with the addition of 400 nM Ubp6-C118A and 100 μM linear Ub_4.

To determine lid affinity through the ATPase response of the base, holoenzymes were assembled at room temperature for 5 min with 100 nM base, 1.6 μM core, 4 μM Rpn10, and varying concentrations of lid, before a 2-fold dilution with ATPase mix to start the reaction. For measurements in the presence of substrate, ubiquitinated titin-I27^{V15P} was added at a final concentration of 3 μM.

Ubp6 Ub-AMC cleavage-activity assays

Ubp6 activity was measured using the cleavage of the fluorogenic Ub-AMC substrate (Life Sensors). Proteasomes were reconstituted as base-limited complexes (at a final concentration of 200 nM base, 1.2 μM lid, 600 μM core, 1.5 μM Rpn10ΔUIM) in either 1X ATP regeneration mix or 4 mM ATPγS with 40 nM Ubp6. After 4 min preincubation at 25 °C, samples were mixed with Ub-AMC to a final concentration of 10 μM. Cleavage was measured by monitoring the change of fluorescence at 445 nm after excitation at 345 nm on a plate reader (Synergy Neo2 Multi-Mode Plate Reader, Biotek).

Measurement of peptidase stimulation

Proteasomes were reconstituted at 2X final concentration with limiting concentration of core particle (10 nM final) and saturating concentrations of base (0.5 μM (1X) or 1 μM (2X) for experiments where the base concentration was doubled), lid (2 μM), and Rpn10 (2 μM) in GF buffer supplemented with 0.5 mM TCEP and 5 mM ATP for 5 min at room temperature. Reconstituted proteasomes were incubated in either 5 mM ATP or 5 mM ATPγS at room temperature for an additional 5 min. Suc-LLVY-AMC was diluted to 2X concentration (100 μM final) in 26S GF buffer. Reactions were initiated by aliquoting 5 μL of reconstituted proteasomes into 5 μL of Suc-LLVY-AMC solution in a 384-well flat bottom black corning plate. Suc-LLVY-AMC hydrolysis was tracked

by the increase in fluorescence upon AMC release in a Synergy Neo2 Multi-Mode Plate Reader (Biotek). Data were fit by linear regression, and slopes were normalized to wild-type proteasomes in ATP.

Proteasome degradation assays

Michaelis-Menten analyses of titin substrate degradation monitored by fluorescence anisotropy

Proteasomes were reconstituted at 2X concentration with limiting concentrations of core particle (100 nM final) and saturating concentrations of base, lid, and Rpn10 (2 µM final) for 5 min at room temperature in assay buffer (GF buffer supplemented with 5 mM ATP, 1 mg/mL BSA, and ATP regeneration (creatine kinase and creatine phosphate)). Fluorescein labeled titin-I27 with a V15P mutation and a C-terminal 35 residue tail (FAM-titin-I27^{V15P}) was prepared at 2X final concentration in assay buffer. Reactions were initiated with 5 µL of proteasome sample being added to 5 µL of FAM-titin-I27^{V15P} substrate in a 384-well flat bottom black corning plate. Degradation was monitored by the loss of fluorescence anisotropy of conjugated fluorescein over time in a Synergy Neo2 Multi-Mode Plate Reader (Biotek). Degradation rates were calculated by determining the fluorescence anisotropy difference between substrate and substrate peptides and applying linear regression to initial anisotropy decreases. Initial rates were plotted against substrate concentration and fitted to the Michaelis-Menten equation (OriginPro9) to determine k_{cat} and K_m values.

Multiple-turnover degradation measured by fluorescence anisotropy

Proteasomes were either reconstituted at 2X concentration with limiting concentrations of core particle (100 nM final) and saturating concentrations of base (0.5 µM), lid (2 µM), Rpn10 (2 µM final) for 5 min at room temperature or purified holoenzyme was diluted to 100 nM (final) in 26S GF buffer with 5 mM ATP, 1 mg/mL BSA, and an ATP regeneration system (creatine kinase and creatine phosphate). Substrate was prepared at 2X concentration in 26S GF buffer. Reactions were initiated with 5 µL of proteasome sample being added to 5 µL of substrate in a 384-well flat bottom black corning plate. Degradation was monitored by the loss of fluorescence anisotropy in a Synergy Neo2 Multi-Mode Plate Reader (Biotek). Degradation rates were calculated by determining the fluorescence anisotropy difference between undegraded substrate and fully degraded substrate (using chymotrypsin (Sigma) to fully degrade substrate) and linear regression.

Single-turnover degradation measured by fluorescence anisotropy

Proteasomes were either reconstituted at 2X concentration with limiting concentrations of core particle (0.9 µM final) and saturating concentrations of base, lid, and Rpn10 (2.5 µM each) for 5 min at room temperature or purified holoenzyme was diluted to 2X concentration (2 µM final) in 26S GF buffer with 5 mM ATP, 1 mg/mL BSA, and an ATP regeneration system (creatine kinase and creatine phosphate). Substrate was prepared at 2X concentration (150 nM final) in GF buffer. Reactions were initiated with 2.5–5 µL of proteasome sample being added to 2.5–5 µL of substrate in a 384-well flat bottom black Corning plate. Degradation was monitored by loss of fluorescence anisotropy in a Synergy Neo2 Multi-Mode Plate Reader (Biotek). Degradation rates were calculated by fitting fluorescence anisotropy traces to a double exponential decay model, see Equation 1 below (OriginPro9).

To assess the effects of doubling the concentration of Rpn5-VTENKIF proteasome, holoenzyme was reconstituted at 4X concentration with limiting concentration of core particle (0.9 µM final) and saturating concentrations of base, lid, and Rpn10 (2.5 µM each, final) for 5 min at room temperature in 26S GF buffer with 5 mM ATP, 1 mg/mL BSA, and an ATP regeneration system (creatine kinase and creatine phosphate). Proteasome was either kept undiluted or diluted to 2X concentration with GF buffer before reactions were initiated with 2.5 µL of 2X substrate (150 nM final) in a 384-well flat-bottom black Corning plate. Anisotropy change over time was observed as described above.

Effects of the regulatory particle on substrate processing measured by fluorescence anisotropy

Regulatory particles were reconstituted at 4X concentration with equimolar base, lid, and Rpn10 (2.5 µM each, final at 1X) for 5 min at room temperature in GF buffer with 5 mM ATP, 1 mg/mL BSA, and an ATP regeneration system (creatine kinase and creatine phosphate), either alone or incubated with core particle (900 nM core particle final; 2.5 µM RP final at 1X or 5 µM RP final at 2X). Control with core particle alone were prepared by mixing 2X core particle (900 nM final) in GF buffer with 5 mM ATP, 1 mg/mL BSA, and an ATP regeneration system (creatine kinase and creatine phosphate). Reactions were initiated by adding 5 µL 2X substrate (150 nM final) to RP/proteasomes in a 384-well flat-bottom black Corning plate. Substrate processing was monitored by the decrease in fluorescence anisotropy in a Synergy Neo2 Multi-Mode Plate Reader (Biotek). After completion of the measurements, samples were diluted with 2X SDS-PAGE sample buffer for SDS-PAGE analysis.

Single-turnover degradation monitored by SDS-PAGE

Gel-based single-turnover measurements of FAM-titin-I27 degradation were initiated as described above. 1.2 µL aliquots at various time points were quenched in 2X SDS-PAGE loading buffer (5 µL) and electrophoresed on 4–20% TGX SDS-PAGE gels (Bio-Rad). Gels were imaged on a Typhoon variable mode scanner (GE Healthcare) for fluorescein fluorescence. Gel lanes were quantified for fraction-of-total fluorescence intensity using ImageQuant (GE Healthcare).

Substrate-tail insertion monitored by FRET

Similar to the previously described procedure (Bard et al., 2019), substrate-tail insertion was measured by detecting FRET between Cy5-labeled ubiquitinated FAM-titin-I27^{V15P} substrate and Cy3-labeled, Rpn11-inhibited proteasomes under single-turnover conditions. Reactions containing 2-fold concentrated, base-limited, and o-PA-inhibited holoenzyme (220 nM base containing Rpt1-$^{I191AzF-Cy3}$, 1.2 µM lid, 800 nM core, 1.5 µM Rpn10, 6 mM o-PA and either 2X ATP Regeneration system or 2.5 mM ATPγS) were mixed with 2X concentrated ubiquitinated Cy5-labeled FAM-titin-I27^{V15P} substrate (6 µM, as 2X stock) in an Auto SF120 stopped flow fluorometer (Kintek). Samples were excited at 550 nm with emission at 576 nm (Cy3) and 690 nm (Cy5) measured simultaneously. Kinetics were determined by fitting of the Cy5 gain of signal to Equation 2.

For substrate-tail insertion reactions monitored by FRET under single-turnover conditions, substrate was prepared as described above. Proteasomes were reconstituted at 2X concentration with limiting amounts of core particle (0.9 µM final) and saturating amounts of base, lid, and Rpn10

(2.5 µM each) for 5 min at room temperature in 26S GF buffer with 5 mM ATP, 1 mg/mL BSA, 6 mM o-PA, and an ATP regeneration system (creatine kinase and creatine phosphate). Substrate was prepared at 2X concentration (150 nM final) in GF buffer. Reactions were initiated with 2.5 µL of proteasome sample being added to 2.5 µL of substrate in a 384-well flat-bottom black Corning plate. FRET was monitored by simultaneous detection of Cy3 (680 nm, 30 nm bandpass filter) and Cy5 (590 nm, 35 nm bandpass filter) after excitation at 540 nm (25 nm bandpass) on a Synergy Neo2 Multi-Mode Plate Reader (Biotek).

Proteasome restart assays

Assays were performed similarly as described (Worden et al., 2017). Briefly, proteasomes were reconstituted in GF buffer with 10 mM ATP and 0.5 mM DTT and allowed to assemble at 20°C for 3 min. Single-turnover reactions were initiated with ubiquitinated TAMRA-G3P substrate. Under restart conditions, assembled proteasome were stalled with substrate by incubating with o-PA (3 mM final) for an additional 3 min at 20°C before substrate addition. Stalled proteasomes were restarted by additional of GF with $ZnCl_2$ at a final concentration of 1 mM. From each reaction, 1.2 µL aliquots after various times were collected and quenched in 5 µL sample buffer (50 mM Tris pH 6.8, 20% glycerol, 0.2% SDS). Gel samples were electrophoresed on Criterion TGX 4–20% SDS-PAGE gels (Bio-Rad) and imaged on a Typhoon variable mode scanner (GE Healthcare) for TAMRA fluorescence using at least 25 µm per pixel resolution. Gels were quantified for fluorescence intensity using ImageQuant (GE Healthcare). Each lane was partitioned into segments for poly-ubiquitinated substrate (Ub_n), unmodified substrate, and peptide products and intensities were quantified as a fraction of total lane intensity. These data were plotted v time and fit to a first order exponential, see Equation 3 below (OriginPro9) to derive degradation rates.

Equations

Double Exponential Decay:
$$(1) y = y_0 + A_1 * \exp(-(x-x_0)/k_1) + A_2 * \exp(-(x-x_0)/k_2)$$

Single exponential decay with linear component:
$$(2) y = y_0 + A_1 * \exp(-x/k_1) + m * x$$

Single Exponential Decay:
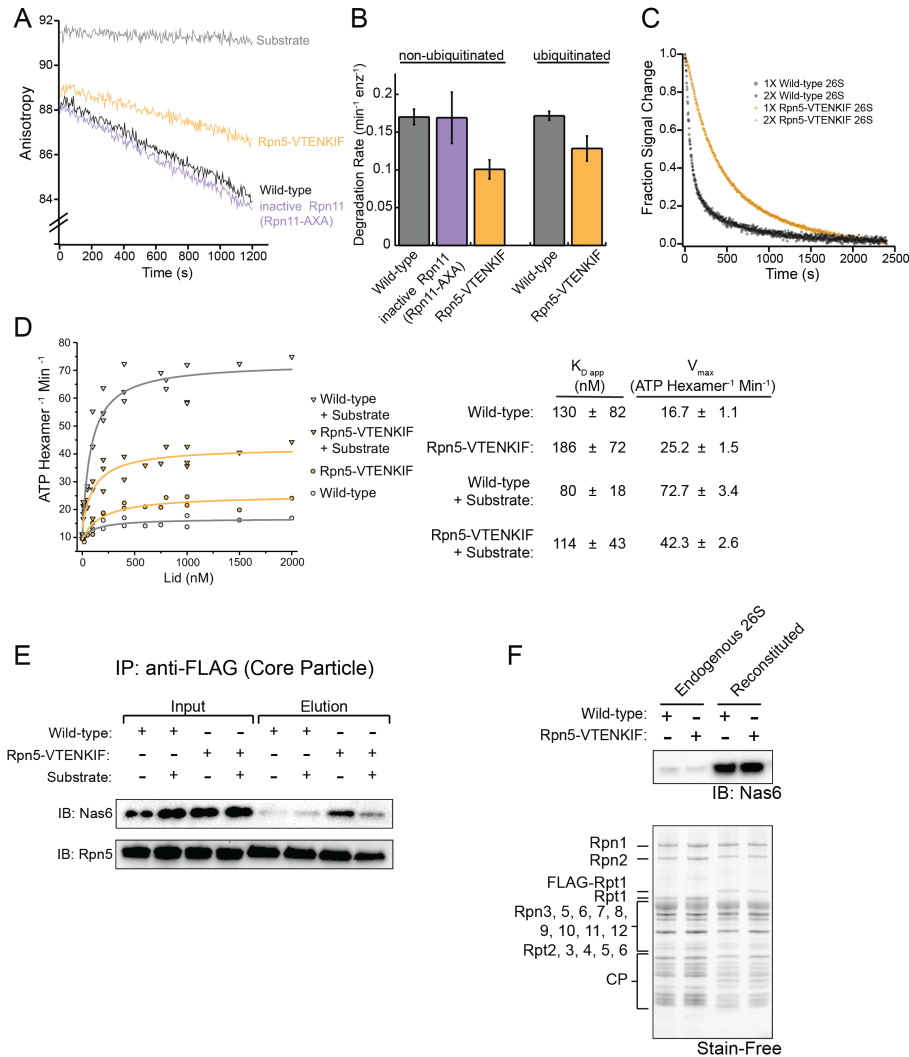$$(3) y = y_0 + A\exp(-x/k)$$

Figure s2.1. Presence of the lid subcomplex and Rpn5's contact with AAA+ are necessary for substrate processing.
(**A**) Representative traces for the changes in anisotropy upon ubiquitin-independent degradation of FAM-titin-I27[V15P] by in-vitro reconstituted proteasomes containing recombinantly produced, SspB-fused base and either wild-type lid, Rpn5-VTENKIF mutant lid, or lid with inactive Rpn11 (Rpn11[AXA]) that were also recombinantly produced. (Matyskiela et al., 2013). (**B**) Comparison of rates for ubiquitin-dependent and -independent degradation of FAM-titin-I27[V15P] by wild-type and mutant proteasomes (both reconstituted), as derived from multiple-turnover measurements similar to the traces shown in (A) (N = 3, technical replicates, error bars plotted are SEM). (**C**) Normalized ubiquitin-dependent single-turnover degradations of ubiquitinated TAMRA-G3P substrate by reconstituted Rpn5-VTENKIF and wild-type proteasomes. Single-turnover conditions were verified by doubling the concentration of proteasome as indicated by 1X and 2X 26S proteasome (N = 2, technical replicates). (**D**) ATPase rates of the base subcomplex in the presence of core and various concentrations of wild-type or mutant lid subcomplex and excess of ubiquitinated FAM-titin-I27[V15P] substrate. Data were fit to a Michaelis-Menten model, and the derived values for k_{cat} and K_D are shown in the table on the right (error represents SEM of the fit). (**E**) Anti-FLAG immunoprecipitation of proteasomes reconstituted with 3XFLAG-tagged core, tag-less base, and tag-less lid, and incubated with or without an excess of ubiquitinated FAM-titin-I27[V15P] substrate. Samples were immunoblotted for Nas6 and lid subunit Rpn5. (**F**) Top: Immunoblotting for the presence of Nas6 in endogenous proteasomes purified from S. cerevisiae and proteasomes in-vitro reconstituted from recombinant lid, recombinant base, and core purified from S. cerevisiae. Bottom: Stain-free detection of the total protein present on the SDS-PAGE gel used for Nas6 immunoblotting above. Proteasome samples analyzed on this gel were used for the single-turnover degradation experiments shown in Figure 1C.
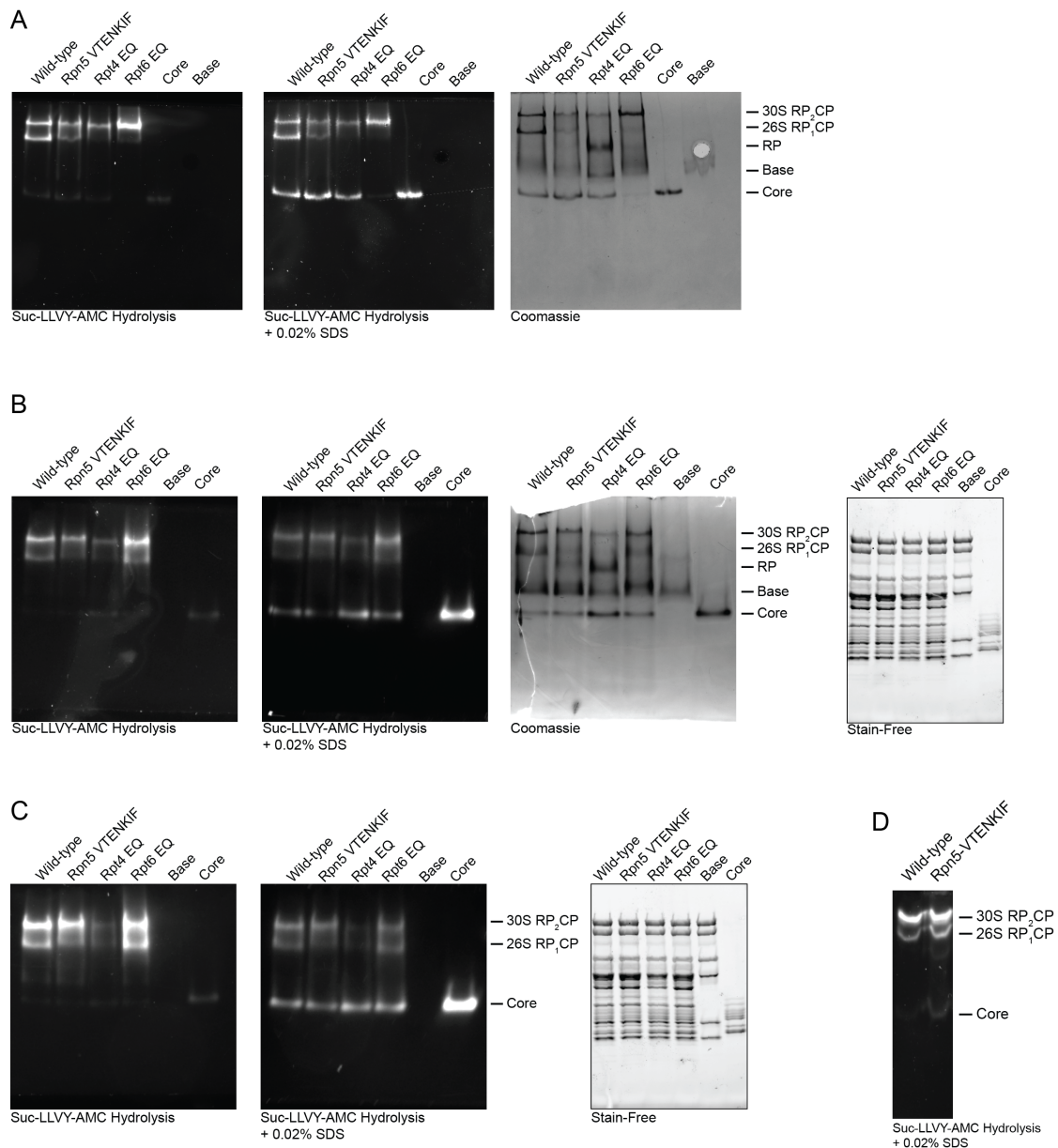
39

Figure s2.2. Analysis of proteasome mutant assemblies by Native-PAGE.
(**A**) The stimulated peptidase activity of the 20S core (CP) upon proteasome holoenzyme formation with reconstituted regulatory particle (RP) components (lid and base) is detected by in-gel cleavage of Suc-LLVY-AMC (left). Free and holoenzyme-incorporated CP is detected by the in-gel Suc-LLVY-AMC cleavage after treatment with 0.02% SDS (middle). The Coomassie stained gel (right) shows the total protein used in the reconstitutions. The left, middle, and right images are visualizations of the same gel. (**B**) and (**C**) Technical replicates of the reconstitutions reactions and native-PAGE gel described in (**A**). Panel B and C show the additional SDS-PAGE analysis of the proteasome-reconstitution reactions, detected by Stain-Free imaging. (**D**) Native-PAGE analysis of endogenous wild-type and Rpn5-VTENKIF proteasomes visualized by in-gel Suc-LLVY-AMC cleavage after treatment with 0.02% SDS.
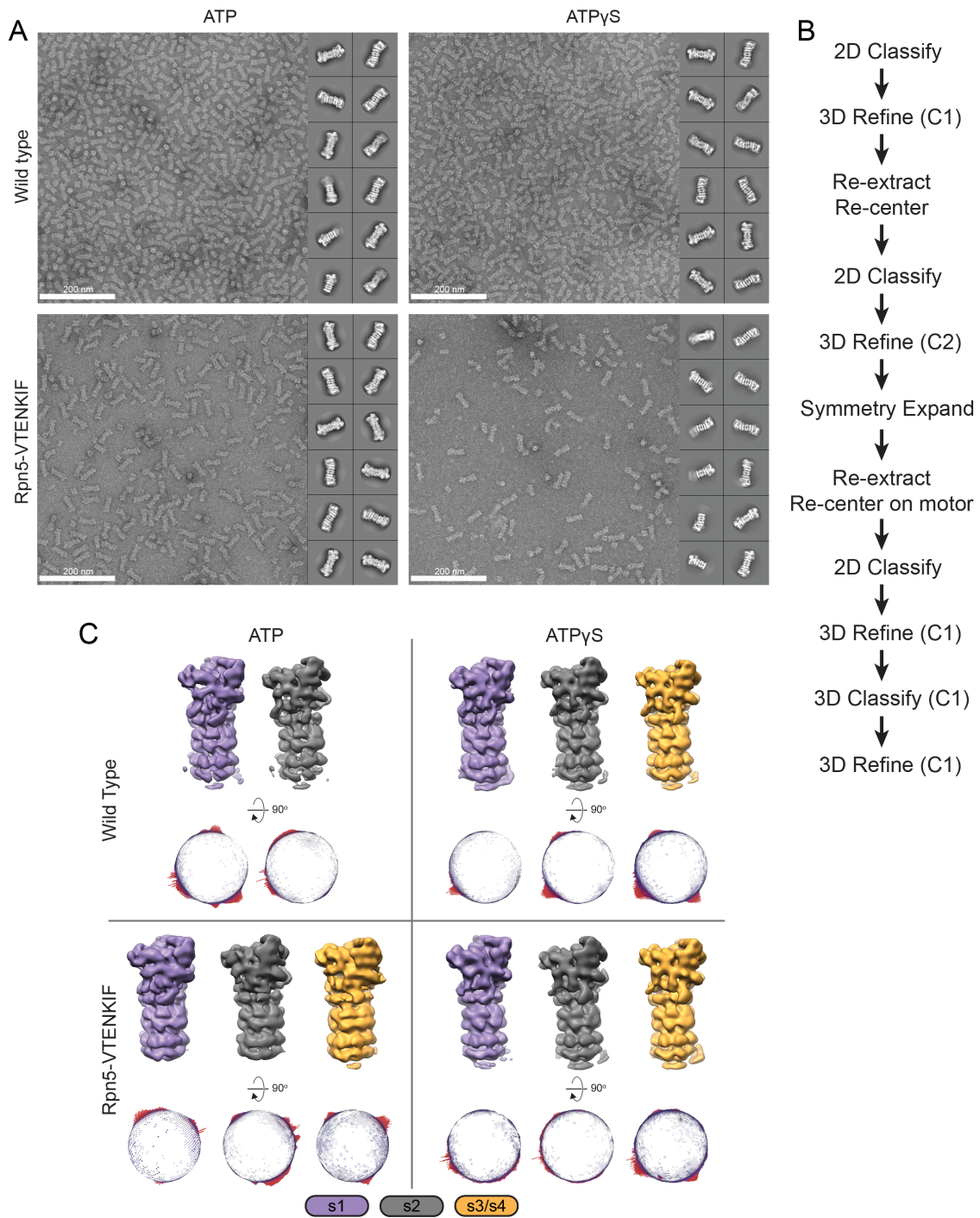
40

Figure s2.3. EM processing of Rpn5-VTENKIF and wild-type proteasomes.
(**A**) Representative images and 2D class averages of wild-type and Rpn5-VTENKIF proteasomes in either nucleotide condition. (**B**) EM workflow as described in Materials and methods. (**C**) Representative 3D classes, colored by conformation classification. Below, Euler distributions presented per conformer displayed above.
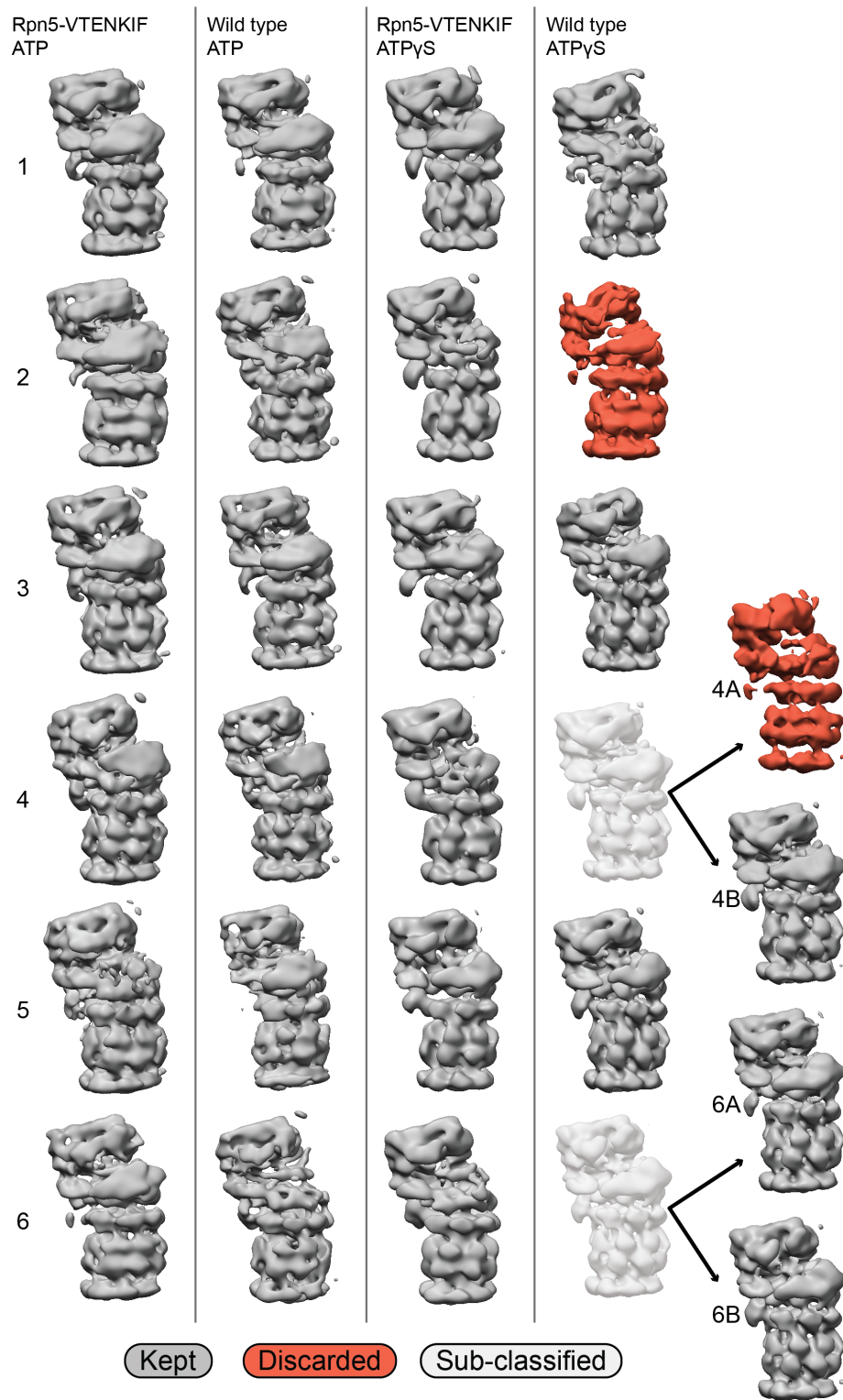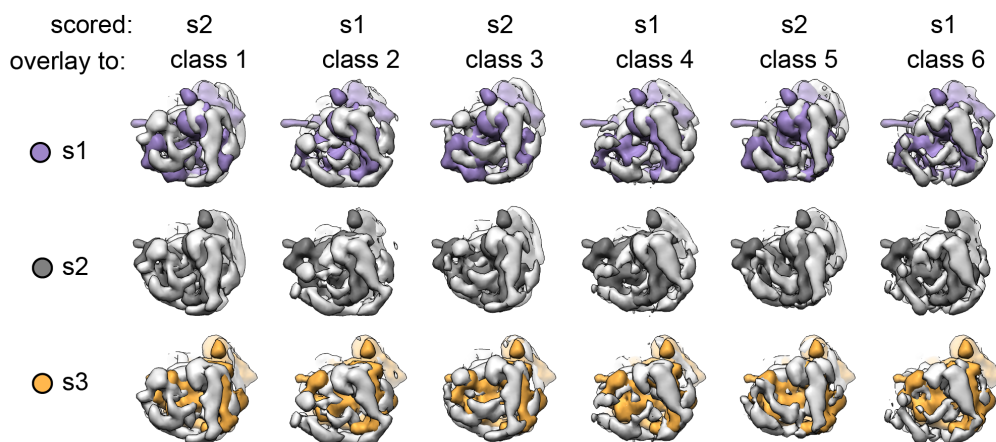
Figure s2.4. Picking of final 3D classes.
Representative views for all six classes attained per dataset. Classes shown in red were discarded due to incomplete density in stable portions of the proteasome, such as the core particle, and poor alignment to any of the simulated densities generated from Eisele et al. (2018). Classes were subclassified and these subclassifications were retained only when they aligned better to different states.
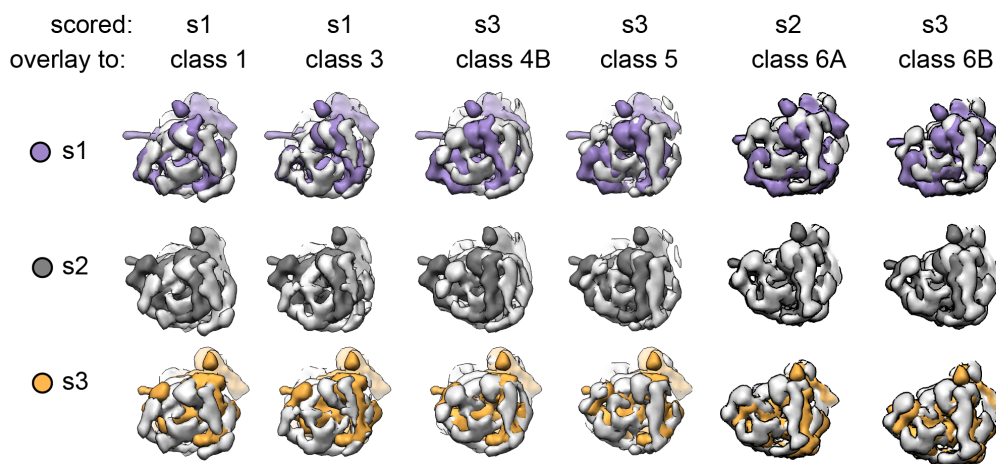
Figure s2.5. Overlays of each class for wild-type proteasomes to simulated 20 Å maps of s1, s2, and s3 states.
Each negative-stain class is shown in light grey and pairwise aligned to the core particles in the 20Å-simulated maps for the s1 (purple), s2 (dark grey), or s3 (orange). Classes were assigned to the scored state based on the best fit of these alignments.
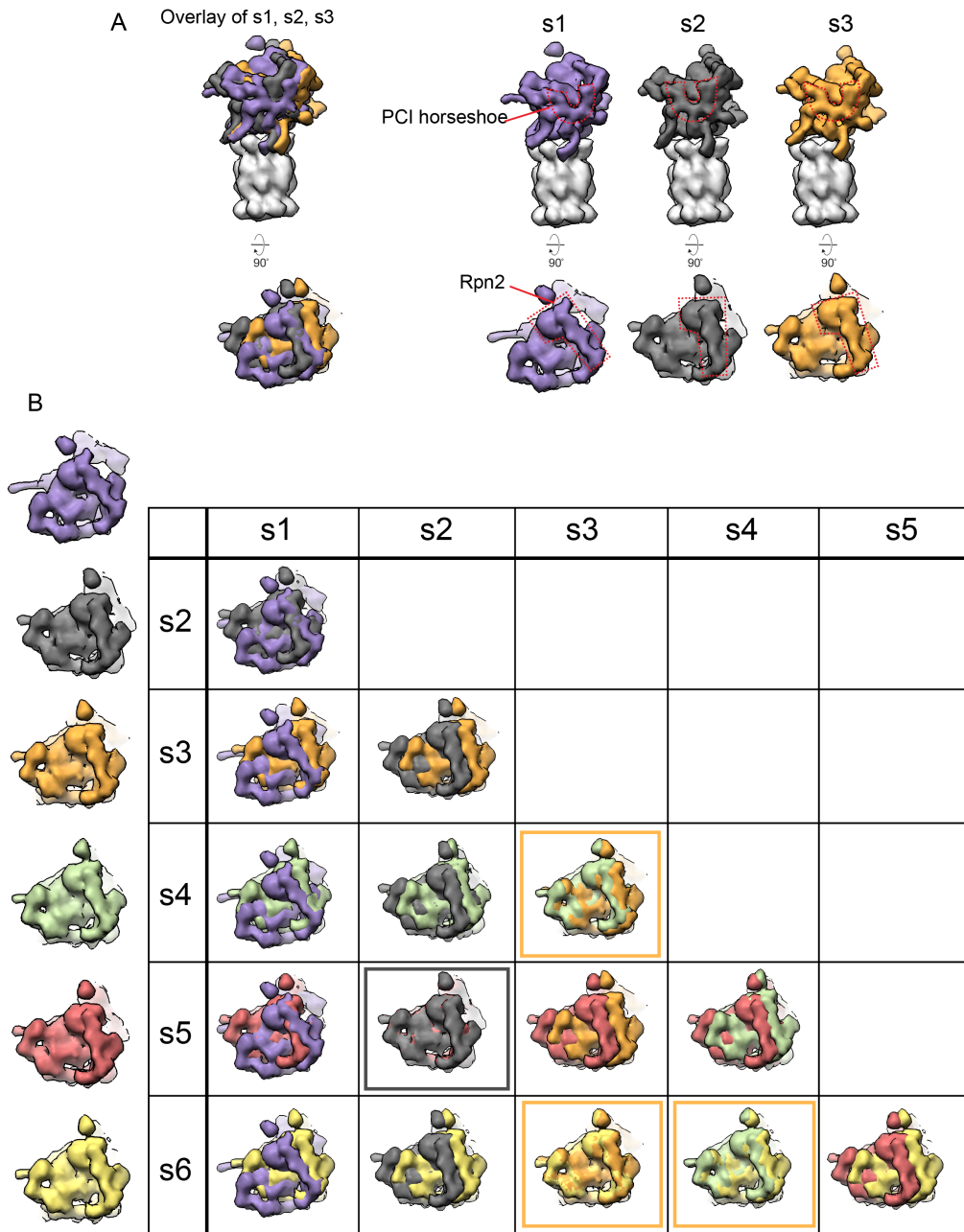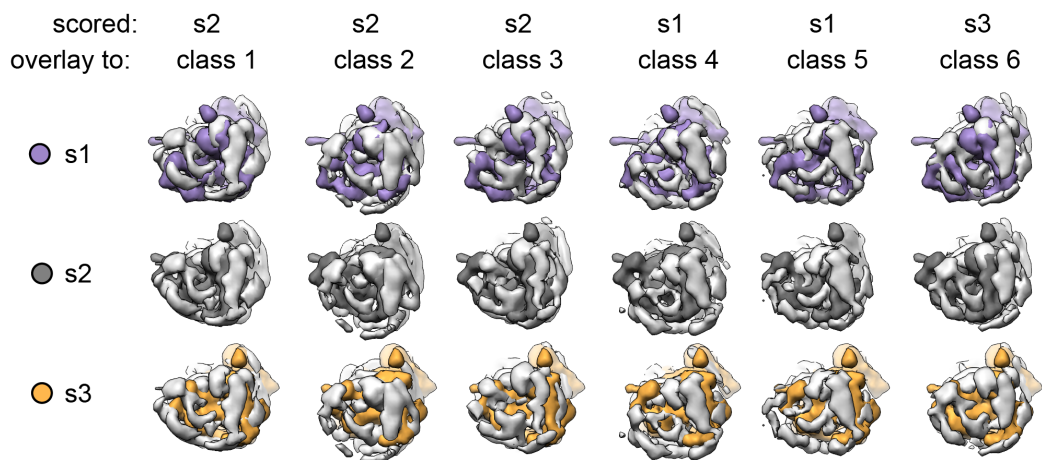
Figure s2.6. Low resolution simulated maps from Eisele et al. (2018) capture the conformational changes that occur in the regulatory particle.

(**A**) Low resolution maps simulated at 20 Å were generated from the atomic models of the s1, s2, and s3 states from Eisele et al. (2018). The overlay on the left was aligned by the core particles and shows the positions of the PCI-horseshoe (top) and Rpn2 (bottom) as distinguishable differences between the three states (below). (**B**) Comparison of all states (s1, purple; s2, dark grey; s3, orange; s4, green; s5, red; and s6, yellow) described in Ref 19, using simulated 20 Å maps generated from the atomic models. At this resolution, s2 and s6 are indistinguishable (boxed in dark grey) as are s3, s4, and s5 (boxed in orange).

Rpn5-VTENKIF ATP

scored:	s2	s2	s2	s1	s1	s3
overlay to:	class 1	class 2	class 3	class 4	class 5	class 6

Rpn5-VTENKIF ATPγS

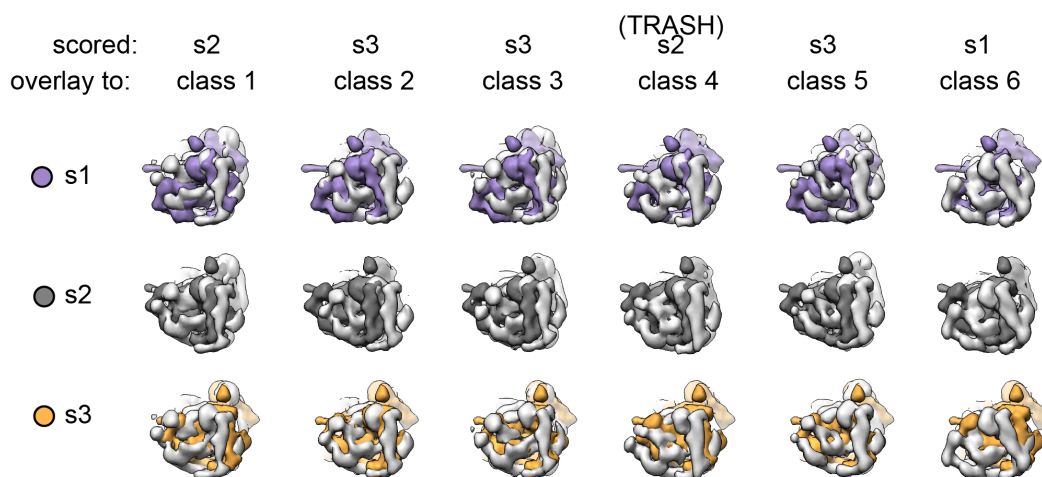| scored:	s2	s3	s3	(TRASH) s2	s3	s1
overlay to:	class 1	class 2	class 3	class 4	class 5	class 6

Figure s2.7. Overlays of each class for Rpn5-VTENKIF-containing proteasomes to simulated 20 Å maps of s1, s2, and s3 states.
Each negative-stain class is shown in light grey and pairwise aligned to the core particles in the 20Å-simulated maps for the s1 (purple), s2 (dark grey), or s3 (orange). Classes were assigned to the scored state based on the best fit of these alignments.
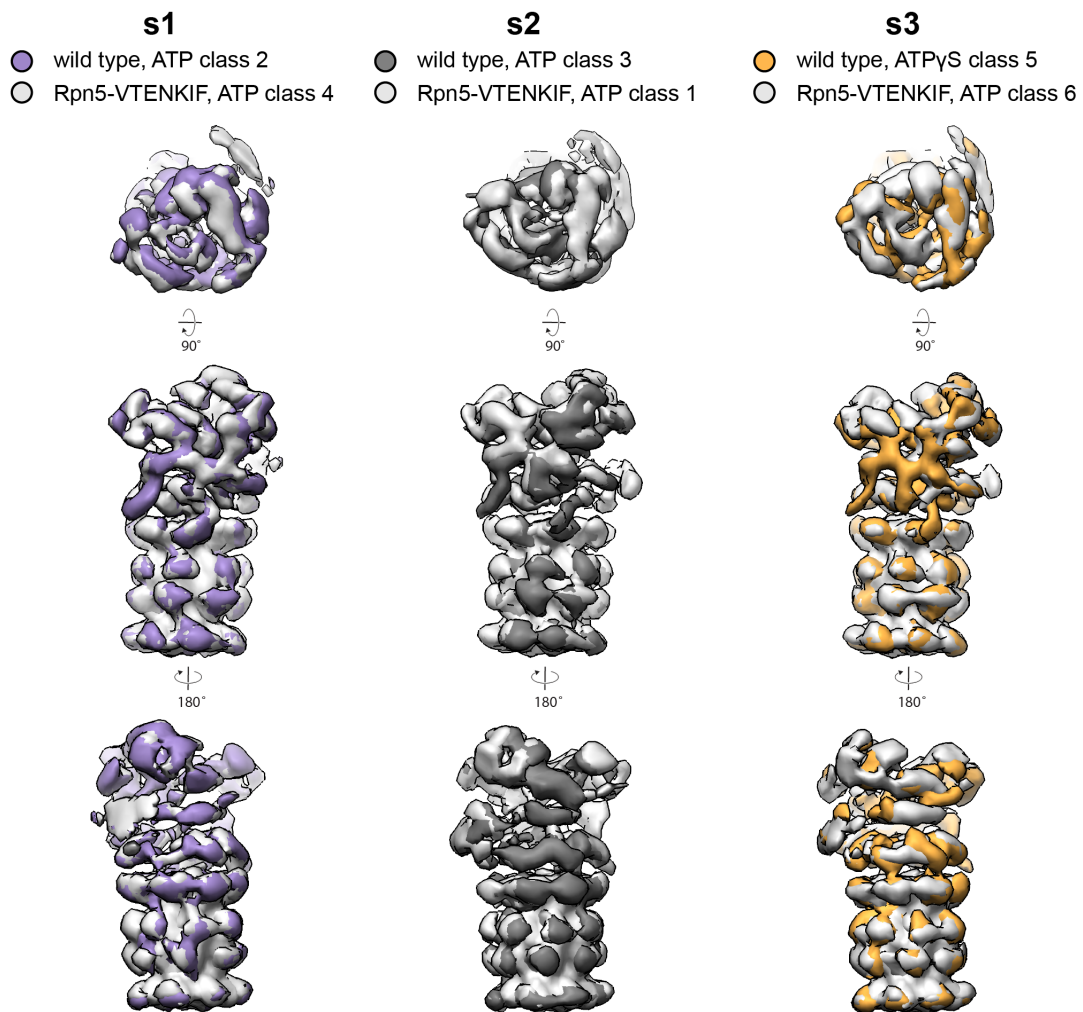
s1
- ⬤ wild type, ATP class 2
- ◯ Rpn5-VTENKIF, ATP class 4

s2
- ⬤ wild type, ATP class 3
- ◯ Rpn5-VTENKIF, ATP class 1

s3
- ⬤ wild type, ATPγS class 5
- ◯ Rpn5-VTENKIF, ATP class 6

Figure s2.8. Overlays of negative-stain classes.
Classes from wild-type and Rpn5-VTENKIF samples that were assigned the same conformational state (s1, s2, or s3) overlay with each other when aligned to a core peptidase model.
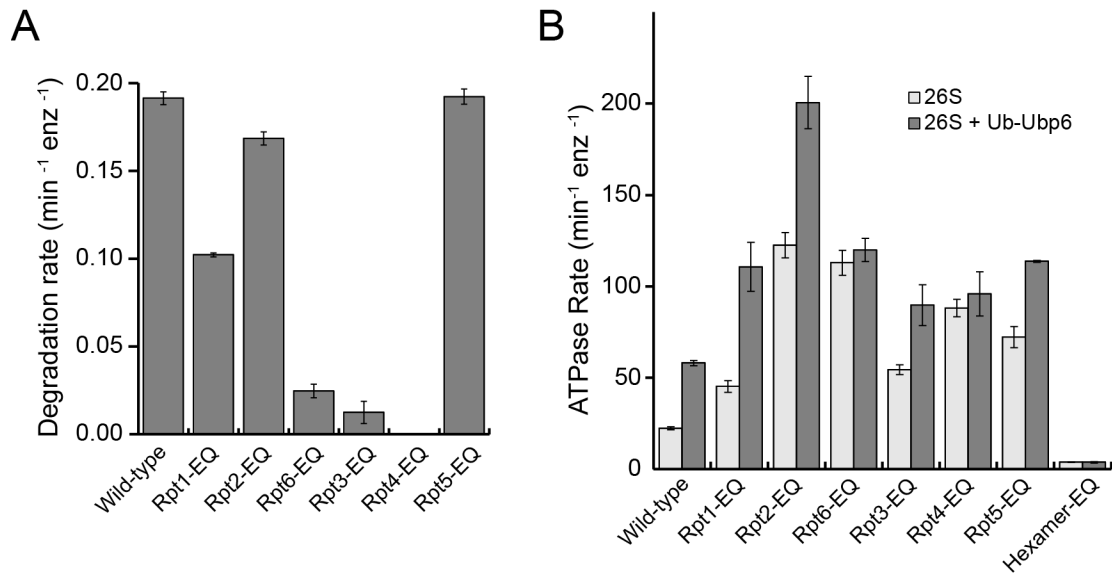
Figure s2.9. Degradation and ATPase activities of Walker-B mutant proteasomes.
(**A**) Rates for multiple-turnover ubiquitin-dependent degradation of FAM-titin-I27^{V15P} (N = 3, technical replicates, error bars represent SD). (**B**) ATPase rates of Walker-B mutant proteasomes in the absence (light grey) and presence (dark grey) of ubiquitin-bound Ubp6, Ub-Ubp6 (N ≥ 3, technical replicates, errors represent SEM).
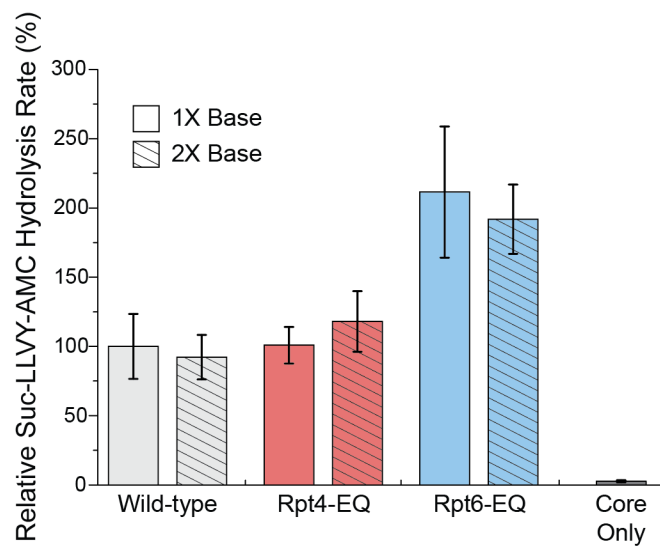

Figure s2.10. Core-gate opening activities of reconstituted proteasomes.
Gate-opening was measured through cleavage of the fluorogenic Suc-LLVY-AMC substrate. Proteasomes were reconstituted with either stoichiometric amounts (1X base) or a two-fold excess of base (2X base). Cleavage rates were determined by linear fitting of the AMC-fluorescence increase, normalized to wild-type proteasome with 1X base, and plotted as averages with standard deviations (N = 3, technical replicates).
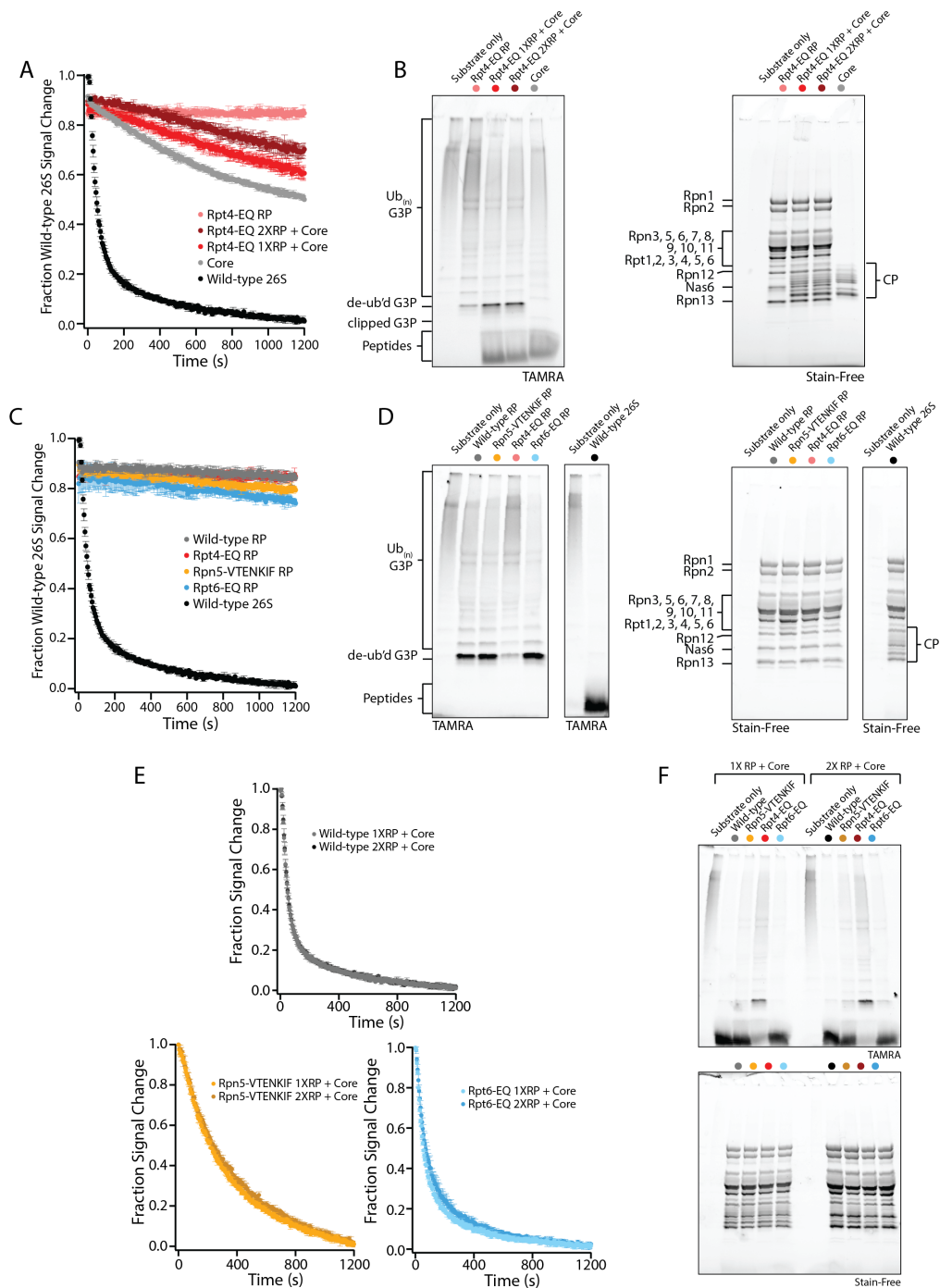
Figure s2.11. Analysis of substrate processing by free regulatory particle during proteasome degradation.
(**A**) Normalized fluorescence anisotropy measurements showing the processing of ubiquitinated TAMRA-G3P-substrate by reconstituted Rpt4-EQ regulatory particle (RP) alone, by proteasomes reconstituted with Rpt4-EQ regulatory particle at stoichiometric amounts (2RP:1CP = 1X RP + Core) or in two-fold access (4RP:1CP = 2X RP + Core), and by core particle alone, normalized to the degradation by reconstituted wild-type 26S proteasome (N = 3; error presented = SD). (**B**) SDS-PAGE analysis of end-point samples from single-turnover degradation reactions performed in (A), visualizing the fluorescence of TAMRA-labeled G3P-substrate (left) and total protein at (right). (**C**) Normalized fluorescence anisotropy measurements showing the processing of ubiquitinated TAMRA-G3P-substrate by proteasomes reconstituted with mutant regulatory particles, normalized to reconstituted wild-type 26S proteasome. (N = 3; error present = SD). (**D**) SDS-PAGE analysis of end-point samples from single-turnover degradation reactions performed in (**C**), visualizing the fluorescence of TAMRA-G3P-substrate (left) and total protein (right). (**E**) Normalized fluorescence anisotropy measurements showing the processing of ubiquitinated TAMRA-G3P-substrate by wild-type,

48

Rpn5-VTENKIF-, and Rpt6-EQ-mutant proteasomes reconstituted with a stoichiometric amount (2RP:1CP = 1 XRP) or two-fold excess of RP (4RP:1CP = 2 XRP). (N = 3, error presented = SD). (**F**) SDS-PAGE analysis of end-point samples from single-turnover degradation reactions performed in (**D**), visualizing the fluorescence of TAMRA G3P-substrate (top) and total protein (bottom).
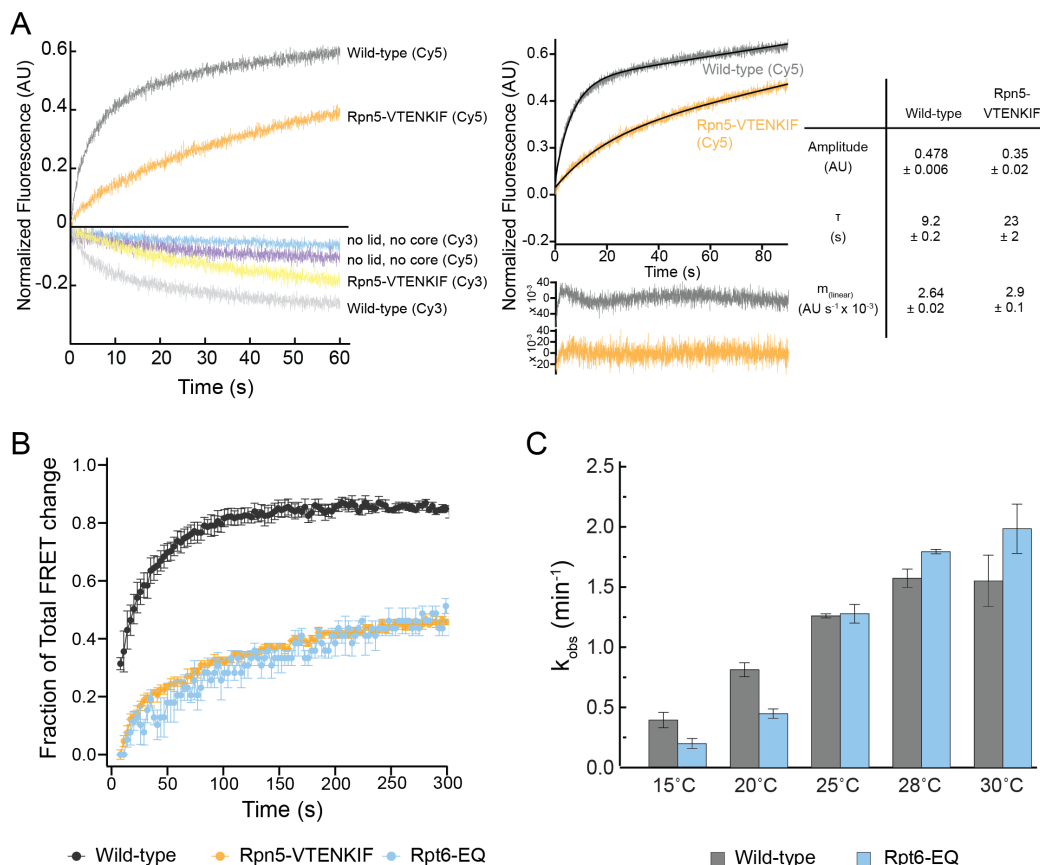

Figure s2.12. Tail insertion can be rate limiting for mutant proteasomes with compromised conformational equilibria.
(**A**) FRET-based assay monitoring the insertion of the ubiquitinated Cy5-labeled titin-I27^{V15P} substrate tail into the central pore of Cy3 labeled, o-PA-inhibited wild-type or Rpn5-VTENKIF mutant proteasomes. Representative traces (left) show the reciprocal change in Cy3 and Cy5 fluorescence, indicative of FRET, and the dependence of substrate-tail insertion on fully assembled proteasomes. Middle, traces for the substrate-tail insertion of wild-type and Rpn5-VTENKIF mutant proteasomes, monitored through Cy5 fluorescence and fit to Equation 2 (solid line). Residuals of the fit are shown below the traces, and derived kinetic parameters are shown on the right (N = 3, technical replicates, error represents SEM). (**B**) FRET-based tail-insertion assay, as described in (A), comparing wild-type, Rpn5-VTENKIF, and Rpt6-EQ mutant proteasomes (N ≥ 3, technical replicates, error represents S.E.M.). (**C**) Ubiquitin-dependent, single-turnover degradation rates as a function of temperature for wild-type and Rpt6-EQ mutant proteasomes degrading the G3P-TARMA substrate. Degradation rates for 15°C and 20°C were determined using a gel-based assay as shown in Figure 5B (N=3, technical replicates, error bars represent SD). The 20°C data are the same as for the single turnover presented in Figure 5B. The 25°C, 28°C, and 30°C degradation data were determined using fluorescence polarization and are presented as the rate constants for the dominant fast phase derived from a double-exponential fit of the degradation kinetics (N=3, technical replicates, error bars represent SD).
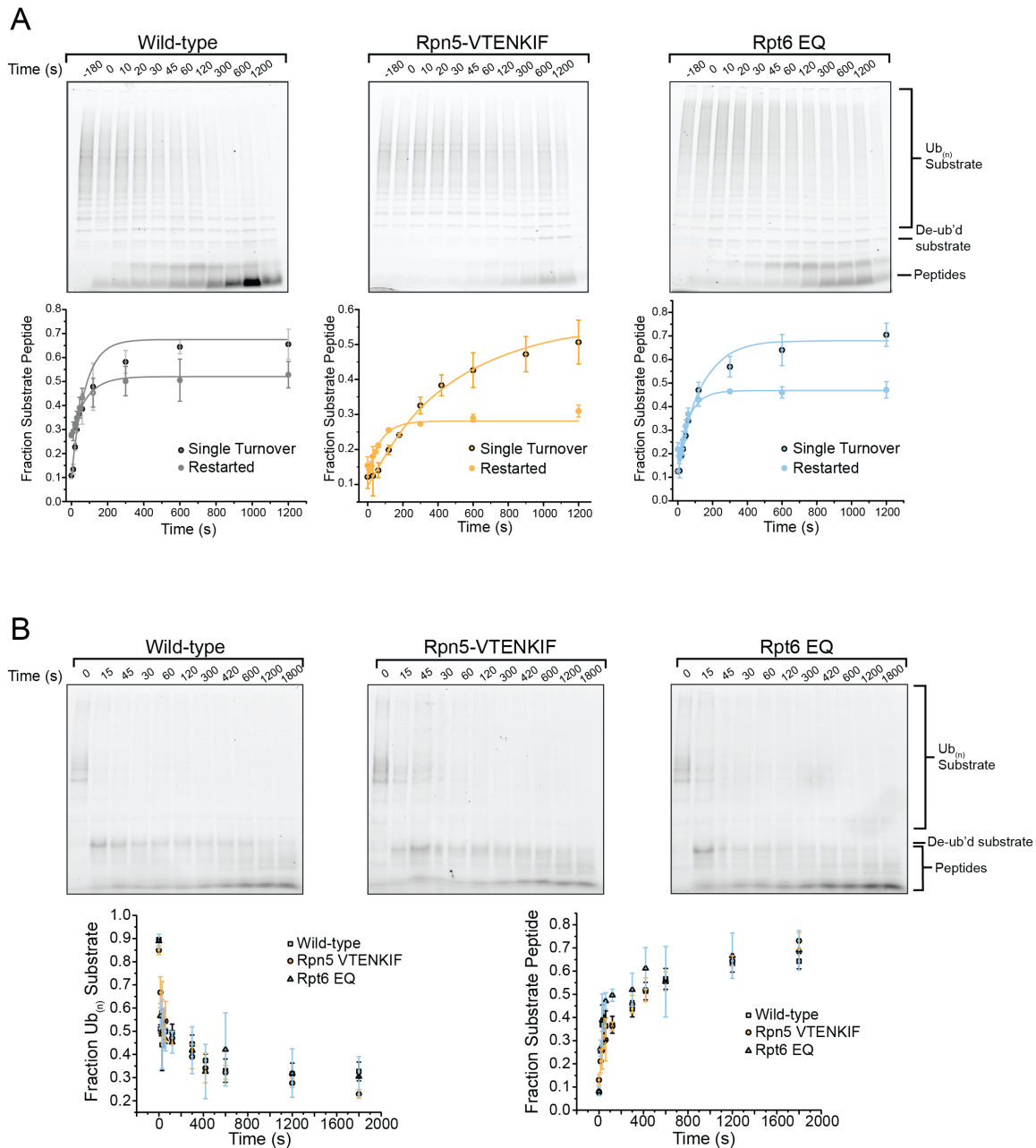
Figure s2.13. Gel based degradation assay analysis.
(**A**) Representative SDS-PAGE gels for the end-point analyses of ubiquitinated TAMRA-G3P-degradation reactions by wild-type, Rpn5-VTENKIF, and Rpt6-EQ mutant proteasomes after restart from an o-PA-induced stall. The fluorescence signal of the substrate-attached TAMRA dye was use for in-gel detection and quantifications, which are plotted below the gels. Data were fitted to Equation 3 (N = 3, technical replicates, error bars represent SD). (**B**) Representative SDS-PAGE gels for the analyses of non-destabilized FAM-titin-I27 degradation by wild-type and mutant proteasomes under single-turnover conditions. Quantified FAM-fluorescence values for ubiquitinated substrate and peptide products are plotted below the gels (N = 3, technical replicates, error bars represent SD).

Chapter 3: Site-specific ubiquitination affects protein energetics and proteasomal degradation

Abstract

Changes in the cellular environment modulate protein energy landscapes to drive important biology, with consequences for signaling, allostery, and other vital processes. The effects of ubiquitination are particularly important because of their potential influence on degradation by the 26S proteasome. Moreover, proteasomal engagement requires unstructured initiation regions that many known proteasome substrates lack. To assess the energetic effects of ubiquitination and how these manifest at the proteasome, we developed a generalizable strategy to produce isopeptide-linked ubiquitin within structured regions of a protein. The effects on the energy landscape vary from negligible to dramatic, depending on the protein and site of ubiquitination. Ubiquitination at sensitive sites destabilizes the native structure and increases the rate of proteasomal degradation. Importantly, in well-folded proteins, ubiquitination can even induce the requisite unstructured regions needed for proteasomal engagement. Our results indicate a biophysical role of site-specific ubiquitination as a potential regulatory mechanism for energy-dependent substrate degradation.

Introduction

A protein's function and folding is defined by its energy landscape, which encompasses all the accessible conformations, their relative populations, and rates of interconversion. This energy landscape is determined by a protein's amino-acid sequence and environment, and small changes modulate this landscape. The phenotypic effects of these changes can range from undetectable to pathological (Kenniston et al., 2004; Liu et al., 2006; Martin et al., 2008; Raschke et al., 1999). Posttranslational modifications (PTMs) are one important environmental change that affect the energy landscape. Many PTMs have been shown to affect protein structure and function (Xin and Radivojac, 2012), and the attachment of ubiquitin to lysine side chains is particularly interesting, as one of its most important roles is to target proteins for degradation by the 26S proteasome.

The ubiquitin-proteasome system (UPS) is responsible for the majority of protein turnover in eukaryotic cells. Ubiquitin is an 8.5 kDa protein appended to other proteins (substrates) through an isopeptide bond between its C-terminus and the amino group of substrate lysines. Ubiquitin itself contains seven lysines, such that additional ubiquitin molecules can be added to form chains of

different lengths, linkages, and topologies. The 26S proteasome is the executor of the UPS, using ubiquitin receptors to selectively bind ubiquitinated substrates and degrade them in an ATP-dependent manner. The degradation activity resides in the proteasome's 20S core particle, whose proteolytic sites are sequestered inside a central cavity. Substrates are delivered to the 20S core particle through the 19S regulatory particle (RP), which caps one or both sides of the barrel-shaped 20S core. RP recruits ubiquitinated substrates, mechanically unfolds them with its AAA+ (ATPase Associated with diverse cellular Activities) motor, and translocates the unstructured polypeptides into the core particle for proteolysis.

Although ubiquitination is best known for its association with proteasomal degradation, it is involved in a wide array of other cellular processes (Swatek and Komander, 2016). Therefore, the proteasome must carefully differentiate between ubiquitinated proteins that should be degraded and those ubiquitinated for other purposes. Failure of the proteasome to properly regulate substrate selection results in aberrant degradation, wasted energy, and collapse of proteostasis.

Conformational properties also affect whether a protein is degraded by the proteasome. In order to engage with the proteasomal AAA+ motor for unfolding and translocation, a substrate needs an unstructured initiation region long enough to enter the central pore and interact with conserved pore loops of the ATPase hexamer (Prakash et al., 2004; Yu et al., 2017). Nonetheless, a significant percentage of proteasome clients lack an obvious unstructured region (Hagai et al., 2011). For some substrates, another AAA+ translocase, Cdc48 (also known as p97 or VCP), has been implicated in preparing them through partial or complete unfolding for subsequent proteasomal engagement (Godderz et al., 2015; Olszewski et al., 2019; Tsuchiya et al., 2017).

An exciting possibility is that ubiquitination itself can modulate the landscape and expose an unstructured region for initiation of proteasomal degradation. Molecular dynamics studies suggest that ubiquitination may destabilize proteins, principally through a decrease in substrate conformational entropy (Hagai et al., 2010; Gavrilov et al., 2015). If true, does this destabilization populate a proteasome-engageable unstructured region? Purification of ubiquitin-conjugated substrates with native isopeptide bonds has been a challenging hurdle (Faggiano and Pastore, 2014), and the experimental characterization of ubiquitin-mediated changes in protein energetics has therefore been limited to artificial, non-physiological ubiquitin-attachment (Morimoto et al., 2016) or heterogeneous samples (Cundiff et al., 2019). Thus, the potential energetic effects of substrate ubiquitination on proteasomal degradation remain completely unknown.

Here, we developed a generalizable protocol to generate milligram quantities of homogeneously mono-ubiquitinated proteins. In this system, ubiquitin is attached via a native isopeptide linkage to a lysine within a folded protein domain. Using several single-lysine variants of the small protein barstar, we show that mono-ubiquitination induces site-specific local and global energetic changes that can lead to significant protein destabilization. Furthermore, these energetic modulations can affect proteasomal processing. Substrate variants destabilized by mono-ubiquitination display enhanced proteasomal degradation rates when appended with an unstructured region for initiation. Importantly, in the absence of these unstructured regions, ubiquitin-induced energetic changes can transiently expose flexible initiation regions, presumably by allowing access to high-energy, partially-unstructured states that are proteasome-engageable. Our data establish a connection between ubiquitin-induced changes in substrate energetics and proteasomal processing. We propose that modulation of substrate energy landscapes by site-specific ubiquitination can play a consequential role for substrate engagement and degradation by the proteasome.

Results

Generalizable strategy for site-specific ubiquitination

Traditional spectroscopic studies of protein energetics and dynamics require large amounts of homogeneous sample, yet such quantities are not feasible using established strategies of ubiquitin attachment (Hagai et al., 2011; Faggiano and Pastore, 2014). Furthermore, many approaches employed for artificial ubiquitin attachment require harsh chemical conjugation conditions and result in non-physiological linkages. Here, we used a biochemically reconstituted enzymatic ligation and deubiquitination strategy to overcome these technical obstacles and produce ubiquitin-substrate conjugates with native isopeptide bonds.

Substrate proteins were expressed as C-terminal fusions to maltose binding protein (MBP) with a connecting linker containing a PPPY recognition sequence for the yeast HECT E3-ubiquitin ligase Rsp5 (Saeki et al., 2005). Since substrates lacking MBP were less efficiently conjugated with ubiquitin, we believe MBP acts as a scaffold to promote productive E3-substrate interaction, as previously described (Kamadurai et al., 2013; Kim et al., 2011). Substrates also contain a single cysteine for fluorescein-maleimide labeling (Fig. 1a).

After purification, efficient *in vitro* poly-ubiquitination was achieved using a reconstituted system with mouse Uba1 ubiquitin-activating enzyme (E1), yeast Ubc4 ubiquitin conjugase (E2), and yeast Rsp5 ubiquitin ligase (E3) (Fig. 1a). Treatment with the K63-specific deubiquitinase AMSH (Associated Molecule with the SH3 domain of STAM) collapses the heterogeneously poly-ubiquitinated substrates into lower molecular weight conjugates (Fig. 1a and Supplementary Fig. 1a-f). AMSH efficiently trims the Rsp5-generated, K63-linked ubiquitin chains, but is much slower in removing the proximal, substrate-attached ubiquitin moiety. Optimizing the AMSH amount and the duration of deubiquitination before quenching with EDTA allowed accumulation of the mono-ubiquitinated species. For experiments requiring large quantities, we generated mono-ubiquitinated substrates using methylated ubiquitin, which prevents chain formation and results in higher yield of modified protein. For both approaches, a two-step subtractive Ni^{2+}-NTA purification followed by size-exclusion chromatography was sufficient to purify the mono-ubiquitinated substrate to homogeneity (Fig. 1b and Supplementary Fig. 2a-2e). Using this generalizable method, we attached ubiquitin to various single-lysine substrates (Fig. 1c-1h, Supplementary Fig. 1a-1f, and Supplementary Fig. 2a-2e) and scaled up to produce spectroscopic quantities.
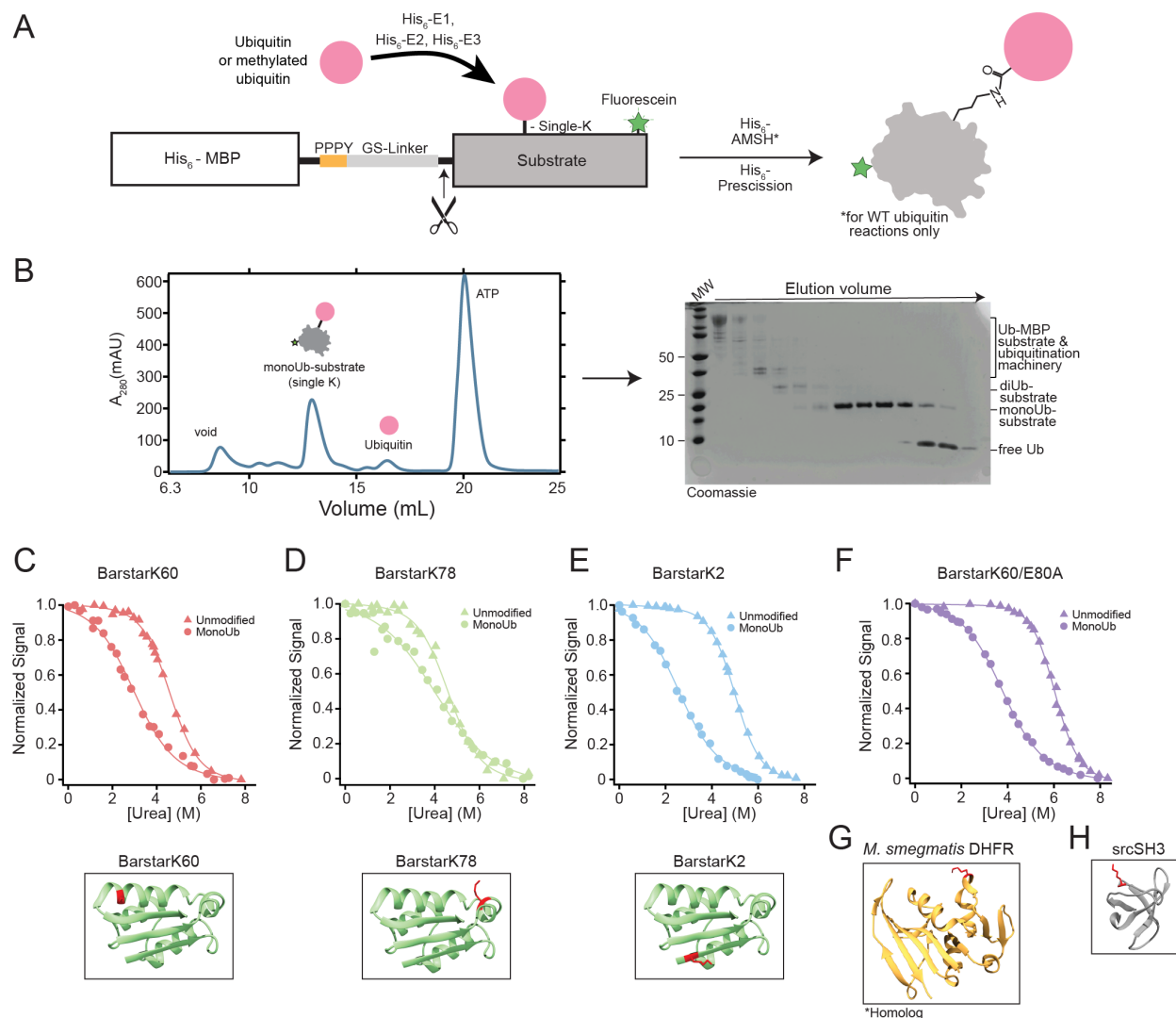
Figure 3.1. Generation of substrates with isopeptide-linked ubiquitin in structured regions and equilibrium unfolding studies. (**A**), Schematic of ubiquitination machinery and substrate design. A His$_6$-MBP scaffold with PPPY Rsp5-binding motif for enzymatic ubiquitination is fused to the N terminus of a single-lysine substrate. *denotes that AMSH treatment is not required when using methylated ubiquitin. **b**, Representative size-exclusion chromatography trace for methylated monoUb-barstar and Coomassie-stained gel of selected size-exclusion fractions, where mAU represents milli-absorbance units and MW represents molecular weight in kDa. **c–f**, Ribbon diagrams of barstar (green, PDB 1BTA) showing the position of ubiquitinated lysines in red and urea-induced unfolding transition ($n = 1$) of unmodified (triangles) and methylated mono-ubiquitinated- (monoUb-)barstar (circles) with barstarK60 presented in (**c**), barstarK78 (**d**), barstarK2 (**e**), and barstarK60/E80A (**f**). **g**, Ribbon diagram of *M. smegmatis* DHFR homolog from *M. tuberculosis* (orange, PDB 1DG8, * denotes that a structure of a homolog is presented) and **h**, *src*SH3 (gray, PDB 1SRL) showing ubiquitinated lysine positions in red.

Site-specific, ubiquitin-induced global energetic changes

The ability to purify milligram quantities of homogenously mono-ubiquitinated proteins enabled us to determine global stability changes using traditional chemically-induced equilibrium unfolding monitored by intrinsic fluorescence. The fluorescence signal arises exclusively from tryptophan residues in our substrates, as ubiquitin is tryptophan-free. For these studies, we used a well-established model protein, barstar from *Bacillus amyloliquefaciens*, in which all except one lysine were replaced by arginine to generate different single-lysine variants for site-specific ubiquitination.

Four single-lysine barstar variants were characterized: barstarK2, barstarK60, barstarK78, and barstarK60/E80A (where the position of the remaining lysine is denoted after barstar). We determined their global stabilities in both unmodified and purified mono-ubiquitinated forms by urea-induced chemical denaturation and fit the data using a two-state assumption and linear extrapolation (see Methods). The non-ubiquitinated versions of all single-lysine variants display only minor destabilization compared to wild-type barstar ($\Delta G_{unfolding}$ = 5.0 +/- 0.5 kcal/mol and C_m = 4.7 +/- 0.2 M urea) (Khurana et al., 1995)(Fig. 1c-1f). In contrast, we observed dramatically different stabilities upon modification with mono-ubiquitin, indicating site-specific effects (Fig. 1c-1f, Table 1).

Table 3.1. Summary of thermodynamic values determined for all barstar variants and *src*SH3

	BarstarK2	BarstarK60	BarstarK78	BarstarK60/E80A	*src*SH3
C_m unmodified (M urea)	4.97 ± 0.28	4.41 ± 0.55	4.65 ± 1.19	6.02 ± 0.38	ND
C_m monoUb (M urea)	2.52 ± 0.16	2.51 ± 0.34	4.24 ± 1.05	3.72 ± 0.26	ND
ΔC_m (M urea)	2.45 ± 0.32	1.90 ± 0.65	0.42 ± 1.59	2.30 ± 0.46	ND
m-value$_{global}$ unmodified (kcal mol^{-1} M)	1.06 ± 0.04	0.96 ± 0.08	0.89 ± 0.17	1.16 ± 0.05	ND
m-value$_{global}$ MonoUb (kcal mol^{-1} M)	0.59 ± 0.02	0.68 ± 0.07	0.48 ± 0.09	0.70 ± 0.04	ND
Δm-value$_{global}$ (kcal mol^{-1} M)	-0.47 ± 0.05	-0.28 ± 0.11	-0.41 ± 0.19	-0.47 ± 0.06	ND
$\Delta G_{unfolding}$ unmodified [a] (kcal mol^{-1})	5.27 ± 0.20	4.25 ± 0.38	4.16 ± 0.74	6.99 ± 0.31	ND
$\Delta\Delta G_{unfolding}$ [b] (kcal mol^{-1})	-2.02 ± 0.10	-1.56 ± 0.22	-0.28 ± 0.45	-2.14 ± 0.11	ND
$\Delta G_{proteolysis}$ unmodified (kcal mol^{-1})	272 ± 0.02	3.24 ± 0.11	2.72 ± 0.06	3.52 ± 0.01	2.70 ± 0.12
$\Delta G_{proteolysis}$ monoUb (kcal mol^{-1})	1.66 ± 0.10	2.12 ± 0.06	2.66 ± 0.09	2.56 ± 0.08	2.38 ± 0.23
$\Delta\Delta G_{proteolysis}$ (kcal mol^{-1})	-1.06 ± 0.11	-1.12 ± 0.13	-0.06 ± 0.15	-0.96 ± 0.12	-0.32 ± 0.10

Equilibrium denaturant-induced unfolding transitions were performed in a single trial (n = 1), and values reported represent fit parameters. Native-state proteolysis experiments were performed in triplicate (n = 3; barstarK2, barstarK78, and barstarK60/E80A) or quadruplicate (n = 4; barstarK60), and values represent the mean. All reported errors represent SEM derived from curve fitting and propagated through all calculations. [a] Indicates that $\Delta G_{unfolding}$ values were calculated using a two-state model with linear extrapolation. [b] indicates that $\Delta\Delta G_{unfolding}$ values were calculated by multiplying the C_m from the denaturation curves by the average m-value for the unmodified and mono-ubiquitinated proteins.

Interestingly, all mono-ubiquitinated constructs show a small but notable decrease in m-value (the denaturant dependence of stability) compared to their unmodified counterparts (Table 1). m-values are known to correlate with the size of a protein or the non-polar surface area exposed during unfolding (Myers et al., 1995), which may slightly change with the various ubiquitin attachments. Alternatively, these decreased m-values may indicate direct surface interactions with ubiquitin or a loss of two-state unfolding behavior, with the population of an unfolding intermediate (Nölting et al., 1997; Zaidi et al., 1997). Because this questions the validity of the two-state assumption used to calculate $\Delta G_{unfolding}$, we report the midpoints of the denaturation curves (C_m) for the unmodified and mono-ubiquitinated variants. BarstarK2 and barstarK60 were destabilized upon mono-ubiquitination (ΔC_m of 2.5 M and 1.9 M urea, respectively, Fig. 1c and 1e). A stabilized mutant of barstarK60, barstarK60/E80A, exhibited nearly identical net destabilization upon mono-

ubiquitination (ΔC_m of 2.3 M urea, Fig. 1f). Conversely, mono-ubiquitination of barstarK78 caused only marginal destabilization (ΔC_m of 0.42 M urea, Fig. 1d). To provide a sense for the thermodynamic changes associated with ubiquitination, we used the average *m*-value of the fits for unmodified and mono-ubiquitinated barstar variants to approximate $\Delta G_{unfolding}$ (Table 1). Taken together, these results establish that the energetic effects of ubiquitin on a particular substrate can be highly site-specific, rather than broadly destabilizing.

Ubiquitination affects energetics of partial unfolding

While the above results demonstrate that mono-ubiquitin attached via a native isopeptide bond can site-specifically alter a substrate's global stability, the globally unfolded state is unlikely to be the most relevant fluctuation for proteasomal degradation. Under cellular conditions, proteins sample partially-unfolded conformations more frequently than the globally-unfolded state. Furthermore, the proteasome does not require global unfolding for successful substrate engagement.

To assess the population of partially-unfolded states, we utilized a quantitative analysis of susceptibility to a soluble protease, thermolysin (Park, 2014; Park and Marqusee, 2004). Because cleavage by soluble proteases requires regions of ~10-12 unstructured amino acids (Park and Marqusee, 2004), proteolysis of well-folded proteins under native conditions occurs via transient excursions to partially-unfolded, high-energy states (Fig. 2a). Typically, the lowest energy conformation that is competent for proteolytic cleavage (the "cleavable state") predominates. Because thermolysin has low affinity for its substrates ($K_d \sim 0.1\text{-}10$ mM), proteolysis of the native state typically proceeds via an EX2-like kinetic regime, in which the proteolysis step itself, rather than the conformational change to the cleavable state, is rate-limiting (Park and Marqusee, 2004). As such, observed proteolysis rates are directly related to the free-energy difference between the native state and this cleavable state ($\Delta G_{proteolysis}$, Supplementary Fig. 3a). The $\Delta\Delta G_{proteolysis}$ for the same protein in two different states (i.e. unmodified and mono-ubiquitinated) can be reliably determined (Park and Marqusee, 2004; Park, 2014).
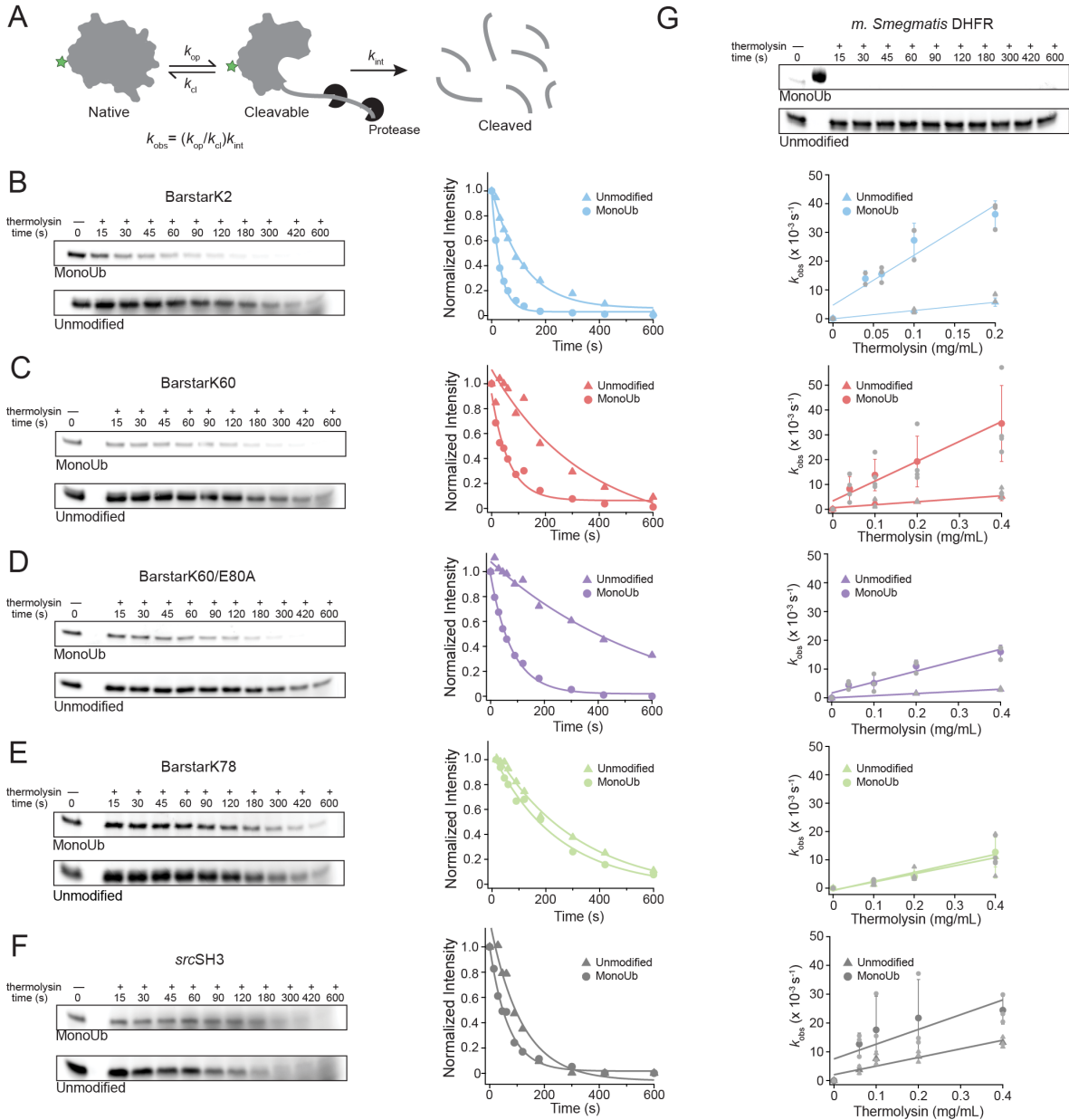
Figure 3.2 Native-state proteolysis demonstrates the effects of mono-ubiquitination on the energetics of partial unfolding.
(**a**) Under native conditions, well-folded proteins are proteolyzed via transient excursions to partially-unfolded states. The observed rate of proteolysis, k_{obs}, is proportional to the free energy of the conformational change from the native to partially-unfolded state ($\Delta G_{proteolysis}$). (**b-f**) Representative gels for native-state proteolysis and quantified band intensities for indicated substrate proteins at 0.2 mg/mL thermolysin. $\Delta\Delta G_{proteolysis}$ upon mono-ubiquitination with non-methylated ubiquitin is calculated from the ratio of slopes of the mean k_{obs} (n=3 for barstarK2, barstarK78, and barstarK60/E80A; or n=4 for barstarK60) against thermolysin concentration ranging from 0.04 to 0.4 mg/mL. Individual trial data are represented in light grey. Error bars represent the standard deviation of replicates. (**g**) Representative gels for native-state proteolysis of *M. smegmatis* DHFR at 0.2 mg/mL thermolysin (n=2). See **Supplementary Fig. 5**.

We measured the $\Delta G_{proteolysis}$ for unmodified and mono-ubiquitinated (non-methylated) versions of all single-lysine barstar variants described above, as well as single-lysine *src*SH3 and *M. smegmatis* DHFR (wildtype is single-lysine). AMSH concentration and reaction length were adjusted to yield a mixture of both unmodified and mono-ubiquitinated protein, which allowed their direct comparison within the same experiment. Importantly, although ubiquitin methylation has been observed to have

various effects on the behavior and recognition of ubiquitin, we observed no difference compared to non-methylated ubiquitin in our biophysical measurements (Supplementary Fig. 4).

Unmodified barstarK2, barstarK60, and barstarK78 exhibit nearly identical proteolysis kinetics (Supplementary Fig. 3b,c) and are proteolyzed through sub-global unfolding ($\Delta G_{proteolysis} < \Delta G_{unfolding}$, Table 1). We observed a similar trend in the $\Delta\Delta G_{proteolysis}$ values as for the global stabilities, with barstarK2 and barstarK60 showing significant changes in the population of the cleavable state ($\Delta\Delta G_{proteolysis}$ = -1.1 kcal/mol, Fig. 2b,c, Supplementary Fig. 5a,c, and Table 1). BarstarK60/E80A exhibited a similar $\Delta\Delta G_{proteolysis}$ (-0.96 kcal/mol, Fig. 2d and Supplementary Fig. 5d). Conversely, negligible $\Delta\Delta G_{proteolysis}$ was detected for barstarK78, indicating no change in the energetics of partial unfolding upon mono-ubiquitination (Fig. 2e and Supplementary Fig. 5b).

These variable effects on $\Delta G_{proteolysis}$ were recapitulated with other proteins. A single-lysine *sn*SH3 domain variant showed little $\Delta\Delta G_{proteolysis}$ (-0.32 kcal/mol, Fig. 2f and Supplementary Fig. 5e), which is particularly interesting because the *sn*SH3 domain is smaller than ubiquitin (64 aa vs 76 aa). In contrast, the naturally single-lysine *M. smegmatis* DHFR (159 aa) shows the most drastic changes upon mono-ubiquitination (Fig. 2g and Supplementary Fig. 5f) and is completely proteolyzed within the dead time of the experiment (15 seconds), despite very little cleavage on this timescale for unmodified DHFR. Interestingly, monoUb-DHFR is still capable of binding methotrexate, albeit with greatly reduced affinity, suggesting that the native state is populated (Supplementary Fig. 2e and Supplementary Fig. 3d). Nevertheless, even in the presence of 500 µM methotrexate, the mono-ubiquitinated variant is completely proteolyzed within the dead time of the experiment (Supplementary Fig. 6).

Fast proteasomal degradation of Ubiquitin-destabilized proteins

The ability of the proteasome's AAA+ motor to unfold proteins is paramount to successful clearance of substrates and has been proposed as the rate-limiting step for degradation (Bard et al., 2019). Therefore, we asked whether ubiquitin-mediated substrate destabilization conferred an increase to the proteasomal degradation rate. In order to compare directly mono-ubiquitinated substrates to their non-ubiquitinated counterparts, we used a system for ubiquitin-independent substrate delivery to the proteasome. In this system, a permutant of the bacterial SspB$_2$ adaptor protein fused to the N-terminus of the Rpt2 ATPase in the proteasomal AAA+ motor recruits substrates that contain an ssrA sequence on a sufficiently long unstructured tail region for engagement (Bashore et al., 2015) (Fig. 3a and Supplementary Fig. 7a). All substrates delivered in this manner are engaged equally, and thus, observed changes in degradation rate can be attributed to differences in substrate energetics. These experiments were performed at substrate concentrations saturating for SspB$_2$ binding, but well below the K$_d$ of mono-ubiquitin for proteasomal ubiquitin receptors (Chojnacki et al., 2017) to rule out contributions of ubiquitin to substrate recruitment and engagement. Proteasome-mediated degradation under single-turnover conditions (Supplementary Fig. 7b) was monitored by SDS-PAGE, and rates were determined based on both the disappearance of full-length substrate and the appearance of peptide products (Fig. 3b and Supplementary Fig. 7c).
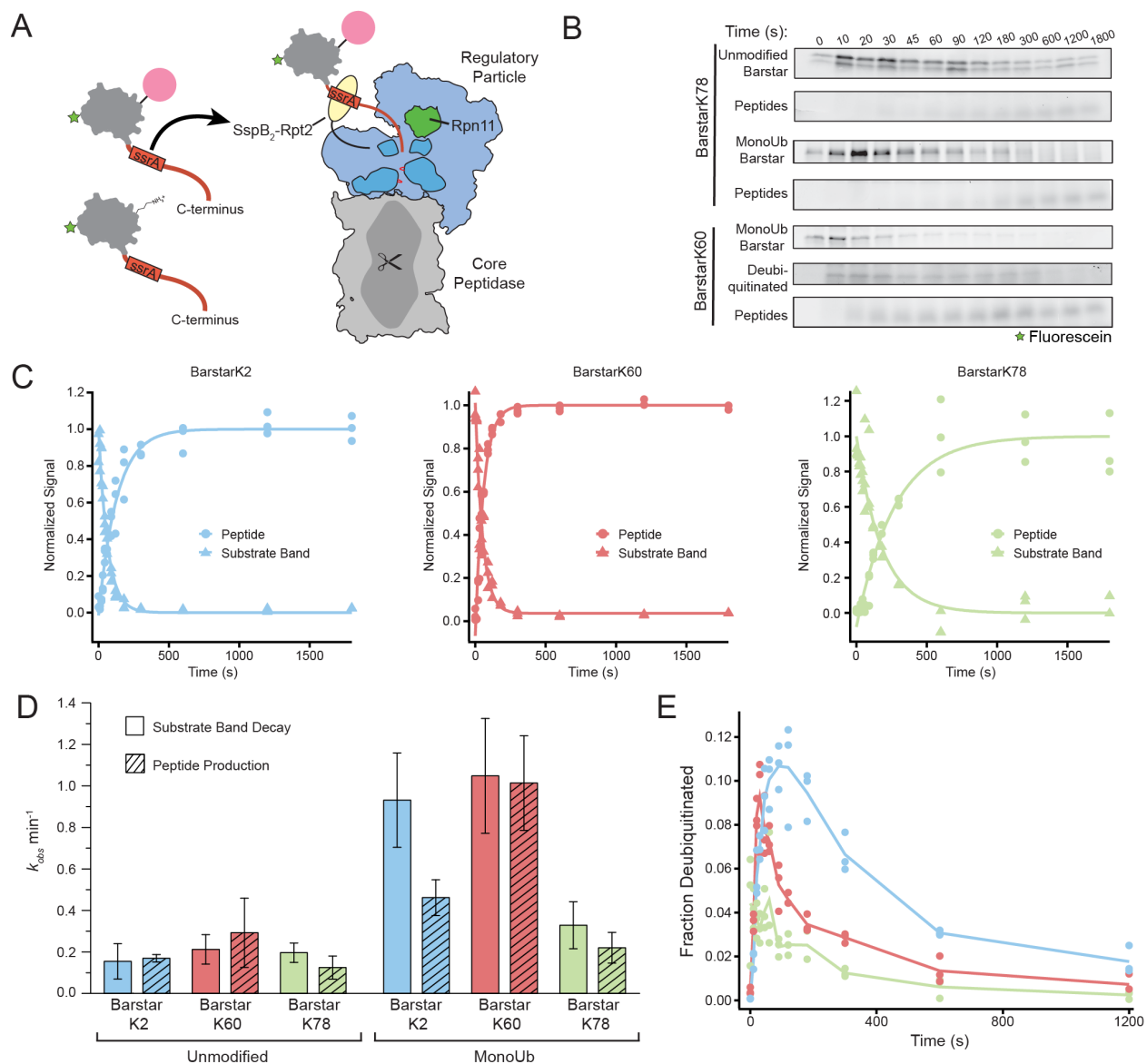
Figure 3.3. Mono-ubiquitin mediated substrate destabilization directly modulates degradation rate. (**a**) Schematic of ubiquitin-independent substrate delivery system, where substrates contain a flexible C-terminal tail with an ssrA-recognition motif that binds an SspB$_2$-dimer (yellow) fused to the base AAA+ ATPase. Core particle is represented in gray, regulatory particle in blue, Rpn11 in green, the AAA+ ATPase motor in dark blue, pore loops in red, substrate in gray, with a green star representing fluorescein, red representing the unstructured tail, and ubiquitin in pink. (**b**) Representative fluorescein-scanned SDS-PAGE gels showing disappearance of unmodified barstarK78 or mono-ubiquitinated (monoUb) barstarK78 and K60 with concomitant peptide production during proteasomal degradation upon ubiquitin-independent delivery. The transient appearance of a deubiquitinated species for monoUb-barstarK60 is shown and quantified in **e**. (**c**) Normalized fractional signal plotted as individual points (n=3) of mono-ubiquitinated substrate band decay and peptide production. Lines represent fit of mean values (n=3) to Equation 3. (**d**) Calculated rates for proteasomal degradation derived by curve fitting to the mean (n=3) and associated fitting errors (S.E.M.) from **b** and **c**. (**e**) Fraction of total signal of deubiquitinated species plotted against time as mean (line) and individual data points (dots; n=3). **See Supplementary Fig. 7**.

All ubiquitinated and non-ubiquitinated barstar variants were processed by the proteasome. As expected, all showed anti-correlated substrate depletion and peptide formation with fast kinetics that were dependent on the presence of RP and ATP (Fig. 3b,c, Supplementary Fig. 7c,d, and Supplementary Fig. 8). Degradation rates thereby correlated with the stability changes described

above. All non-ubiquitinated barstar variants displayed similar degradation kinetics, with an observed rate (k_{obs}) of 0.1 - 0.3 min^{-1} (Fig. 3d). As previously documented, full-length, unmodified substrate bands appeared as doublets (Bard et al., 2019). MonoUb-barstarK78 showed comparable kinetics, consistent with the negligible stability change upon ubiquitination for this variant (Fig. 3d). However, for the highly destabilized monoUb-barstar variants, degradation kinetics were substantially increased (k_{obs} = 1.04 min^{-1} for monoUb-barstarK60 and 0.93 min^{-1} for monoUb-barstarK2), suggesting that ubiquitin-mediated substrate destabilization increases the rate of unfolding by the proteasome.

For monoUb-barstarK60, we obtained similar results when following the substrate decay versus peptide production (Fig. 3c,d). For the monoUb-barstarK2 variant, however, these two processes were decoupled, with the mono-ubiquitinated species disappearing two times faster than the appearance of peptide products (Fig. 3c,d). This apparent decoupling may originate from differences in the temporal order of deubiquitination and unfolding. All variants showed a transient appearance of deubiquitinated species (Fig. 3e), accounting for ~10% of the total substrate intensity for barstarK2 and barstarK60 at their peak. However, the deubiquitinated barstarK60 species was short-lived (peaked at 30 s, negligible at 3 mins), while the barstarK2 species persisted for ~5 mins. Differences in the placement of ubiquitin relative to the substrate-engagement site (the C-terminal appended tail) may alter the timing of deubiquitination relative to crossing the unfolding barrier. In the native barstar structure, the N- and C-termini are located in close proximity (Fig. 1c-e and Fig. 3a, PDB: 1BTA). Engagement via the fused C-terminal tail may therefore place the K2-ubiquitin in close proximity to the proteasome's deubiquitinase (Rpn11), allowing deubiquitination immediately after engagement and before unfolding. If deubiquitination occurs prior to substrate unfolding, the destabilizing effect conferred by ubiquitin is lost, resulting in a lower rate of peptide production compared to the disappearance of the ubiquitinated substrate. Other ubiquitination sites (such as K60 or K78) might require substrate unfolding and translocation to occur first to position the ubiquitin-modified lysine for deubiquitination. These data therefore support the correlation between a substrate's thermodynamic stability and its rate of proteasomal degradation, and extend this hypothesis to include ubiquitin attachment as a mode of site-specific destabilization of substrate proteins.

Ubiquitination can induce a proteasome-engageable region

We next investigated the effect of ubiquitin-induced energetic changes on substrate engagement by the proteasomal AAA+ motor. Numerous studies have demonstrated the role of an unstructured initiation or engagement region (Lee et al., 2001; Prakash et al., 2004; Yu et al., 2017), yet a substantial fraction of cellular proteasomal substrates appear to lack such flexible segments (Hagai et al., 2011), begging the question of how their degradation is initiated. While other unfoldases, like Cdc48/p97 may generate disordered regions (Olszewski et al., 2019; Tsuchiya et al., 2017; Twomey et al., 2019), it is also possible that for some proteins ubiquitin-mediated conformational changes are sufficient to expose the obligate unstructured segments. To test this hypothesis, we poly-ubiquitinated our panel of single-lysine barstar variants (Ub$_n$-barstar) and assayed the proteasome's ability to recognize these substrates via its endogenous ubiquitin receptors and degrade them in an ATP-dependent manner (Fig. 4a). Native-state proteolysis experiments showed that these poly-ubiquitinated barstar variants have similar energetic profiles as the mono-ubiquitinated variants (Supplementary Fig. 9a).

Surprisingly, despite not harboring any obvious proteasome-engageable unstructured region, some poly-ubiquitinated single-lysine barstar variants were fully degraded by the 26S proteasome, whereas others were only slowly deubiquitinated (Supplementary Fig. 9b). Importantly, the degradation kinetics depend on the ubiquitination site and correlate with the thermodynamics reported above. To gain a quantitative understanding of the degradation kinetics, we utilized the fluorescein label on Ub_n-barstar and monitored degradation through the decrease in fluorescence polarization (Fig. 4a). Under single-turnover conditions (confirmed by varying the proteasome concentration, Supplementary Fig. 9c), Ub_n-barstarK60 and Ub_n-barstarK2 showed exponential degradation kinetics, with time constants of approximately 310 s and 432 s, respectively (Fig. 4b,c). In contrast, Ub_n-barstarK78 did not show measurable degradation, consistent with the hypothesis that site-specific, ubiquitin-mediated substrate destabilization determines whether an unstructured region for proteasome engagement is sufficiently populated (Fig. 4d). Furthermore, introducing the stabilizing mutation E80A to Ub_n-barstarK60 substantially increased the degradation time constant to 1018 s (Fig. 4b).
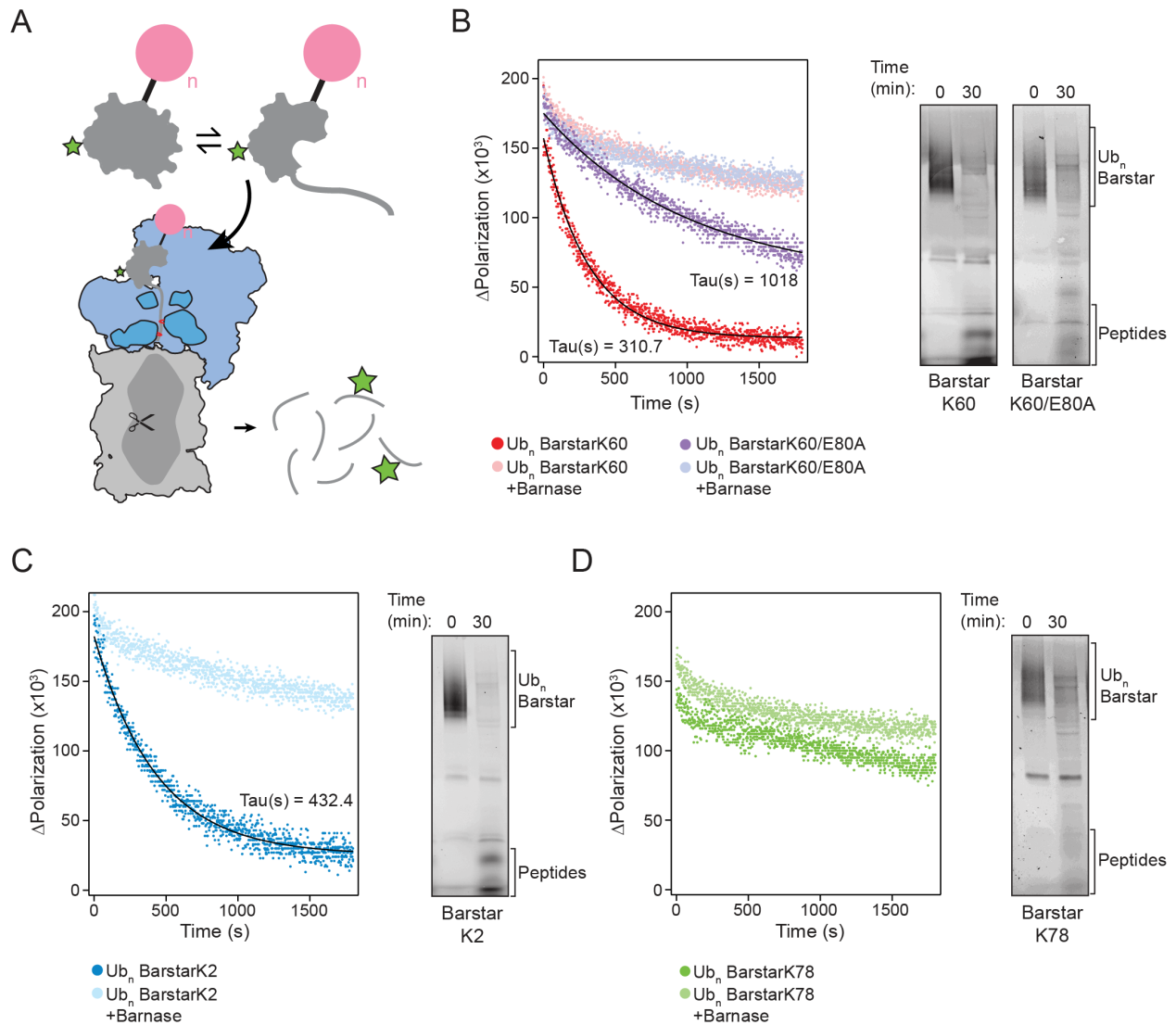
Figure 3.4. Ubiquitin-mediated destabilization of barstar is sufficient to expose a proteasome-engageable unstructured region. (**a**) Schematic of degradation reaction, showing Ub$_n$-substrate lacking an unstructured region at equilibrium with a partially-unfolded state, whereby the partially-unfolded state is competent for proteasome engagement, unfolding, and proteolysis. Core particle is represented in gray, regulatory particle in blue, the AAA+ ATPase motor in dark blue with pore loops in red, substrate in gray with a green star representing fluorescein, and ubiquitin in pink. Degradation can be monitored through the decrease in fluorescence polarization upon transition from a large poly-ubiquitinated substrate to peptides. (**b-d**) Left: fluorescence polarization kinetic measurements for single-turnover degradations of Ub$_n$-barstar in absence or presence of saturating barnase, presented as individual data points (n=3), with lines representing fitting to Equation 3 and calculated time constants (Tau) shown. Right: fluorescein scan of SDS-PAGE gel with 30-minute endpoint samples for single-turnover Ub$_n$-barstar degradations, showing conversion of substrate to peptides and/or deubiquitinated species. Uncropped gels are presented in **Supplementary Fig. 9**.

To further support our hypothesis that the ubiquitin-mediated modulation of barstar's energy landscape is the principal determinant for its degradability, we added saturating concentrations of barnase, the high-affinity ligand of barstar, to these reactions (Supplementary Fig. 9d). In all cases, barnase ablated substrate degradation. The remaining minimal decrease in fluorescence polarization could be attributed to minor degradation-independent deubiquitination (Fig. 4b-d). Addition of barnase has no effect on the degradation of a ubiquitinated titin substrate with a flexible initiation region (FAM-Titin-I27^{V13P,V15P}-35mer-tail)(Bard et al., 2019), confirming that the inhibition observed

for the barstar variants was due to specific binding and stabilization of barstar's folded state, rather than inhibitory interactions with the proteasome (Supplementary Fig. 9d).

In addition, we monitored degradation of the Ub_n-barstar variants by the isolated core particle to verify that robust degradation requires the entire 26S proteasome and includes ubiquitin recognition, ATP-driven unfolding and translocation. The core particle can only hydrolyze unstructured polypeptides that diffuse into its central chamber to access the proteolysis sites. Indeed, the core particle only minimally cleaved the Ub_n-barstarK2 and Ub_n-barstarK60 species with low rates compared to the 26S holoenzyme (Supplementary Fig. 9c,e). Similar to the differences seen for the ATP-dependent degradation by the 26S proteasome, Ub_n-barstarK78 displayed no core-particle mediated degradation, and Ub_n-barstarK60/E80A was cleaved by the core much more slowly than Ub_n-barstarK60.

Unlike our observations with the ubiquitin-independent delivery system, where we saw buildup of a deubiquitinated species for monoUb-barstarK2 (Fig. 3e), Ub_n-barstarK2 did not populate a deubiquitinated species (Fig. 4c and Supplementary Fig. 9b). Because Ub_n-barstarK2 lacks the appended unstructured C-terminal tail, it must engage via a partially-unfolded state, in which the ubiquitin attachment site may no longer be optimally positioned for Rpn11-mediated cleavage prior to unfolding. Moreover, given that this variant is ubiquitinated near the N-terminus, it must be engaged C-terminal to the ubiquitination site. This is confirmed by our observation that inhibition of Rpn11 deubiquitination by *o*-phenanthroline did not inhibit degradation of Ub_n-barstarK2, but inhibited all other variants (Supplementary Fig. 10a). For Ub_n-barstarK2, the polypeptide between the ubiquitin-attachment point, K2, and the fluorescein-labeled Cys82 (80 residues) is long enough to span the minimal distance between the entrance of the AAA+ pore and the proteolytic active sites (approximately 55 residues; Supplementary Fig. 10b). Rpn11-inhibited proteasomes can therefore move this substrate far enough into the 20S core for proteolysis near fluorescein, before translocation stalls on the K2-attached ubiquitin chain (De la Peña et al., 2018).

Ubiquitin-induced unfolding is rate-limiting for degradation

The proteasomal degradation rates observed for poly-ubiquitinated barstar variants are notably lower than for barstar or other substrates with flexible tails (Bard et al., 2019; Worden et al., 2017; Greene et al., 2019), suggesting that engagement of a spontaneously unfolding region represents the rate-limiting step for degradation. To probe this further, we turned to a proteasome variant, Rpn5-VTENKIF, whose mutations in the RP affect the conformational equilibrium of the proteasome and thereby hinder insertion of flexible segments into the AAA+ pore, making engagement rate-determining even for moderately stable substrates with unstructured tails (Greene et al., 2019). Using Rpn5-VTENKIF proteasome, we see a three-fold (Ub_n-barstarK2) and two-fold (Ub_n-barstarK60) decrease in degradation rates (Supplementary Fig. 10c), suggesting that their slow degradation kinetics are indeed determined by slow engagement and not unfolding. This leads to the interesting conclusion that for well-folded substrates, exposure of a flexible segment through spontaneous unfolding determines the rate of degradation, providing an alternative means of regulation for proteasomal targeting.

Discussion

Clearance of damaged, misfolded, and regulatory intracellular proteins is paramount for sustaining life and catalyzed largely by the UPS. While substrate energetics critically affect the degradation of various substrates (Bard et al., 2019; Guo et al., 2018; Prakash et al., 2004; Reichard et al., 2016), the influence of the substrate-attached ubiquitin itself has been elusive. Here, we show that ubiquitin can mediate substrate destabilization with direct consequences for proteasomal degradation. To carry out these studies, we developed a generalizable system to produce ubiquitin-modified single-lysine proteins with native isopeptide bonds (Fig. 1a), achieving efficient ubiquitination for several different single-lysine substrates. We expect that this strategy will be useful to address a number of biological questions that are currently hampered by challenges in producing and purifying proteins with natively attached ubiquitin on structural domains (Faggiano and Pastore, 2014). Using these isopeptide-linked ubiquitinated substrates, we show that ubiquitin-mediated energetic effects can dictate how fast a protein is degraded and, surprisingly, whether a protein is susceptible to proteasomal degradation at all, thus providing an additional regulatory mechanism for clearance of a ubiquitinated substrate based on its conformational and energetic properties.

Consistent with this concept, we found that stabilizing the substrate via ligand binding (as in barstar:barnase) inhibits proteasomal processing. The engagement of these substrates appears to be rate-limiting and modulated directly by the accessibility of partially-unfolded, proteasome-engageable states. Thus, the overall context of the ubiquitinated protein with respect to cellular environment, binding partners, and perhaps other stabilizing or destabilizing PTMs can influence whether a ubiquitinated substrate is actually degraded.

Based on our results, we can build a model for the effect of ubiquitin-mediated, site-specific changes in protein energy landscapes on proteasomal degradation (Fig. 5), in which: 1) a protein may or may not be engaged by the proteasome based on its altered energetics, and 2), the speed with which ubiquitinated substrates are degraded is related to the extent of ubiquitin-induced destabilization. Both aspects of proteasomal turnover are directly modulated by the increased sampling of partially-unfolded states and further influenced by other factors, such as stabilizing mutations or deubiquitination prior to substrate unfolding, either at the proteasome by Rpn11 or by a host of cellular deubiquitinases (Komander and Rape, 2012).
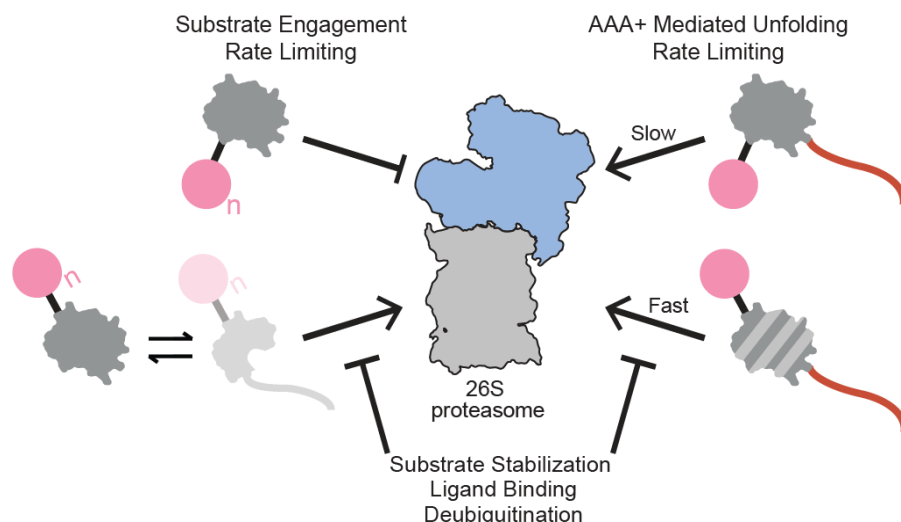
Fig. 5 | Model for the consequences of site-specific, ubiquitin-induced substrate energy landscape modulation on proteasomal degradation. If ubiquitination occurs on a non-sensitive structured lysine, as in barstarK78, the substrate does not sufficiently populate a partially-unfolded, proteasome-engageable conformation. If ubiquitin-modification occurs on a sensitive lysine, as in barstarK2 and barstarK60, the otherwise well-folded substrate is sufficiently destabilized to populate partially-unfolded, proteasome-engageable conformations and is successfully degraded. The observed degradation kinetics thus appear dependent on the changes to the protein energy landscape upon ubiquitination. When substrates contain an unstructured proteasome-engageable region, ubiquitination at sensitive lysine positions allows for substantially faster degradation kinetics, while degradation kinetics of substrates with non-destabilizing ubiquitinations remain essentially unchanged. Successful proteasome engagement and degradation of ubiquitin-destabilized substrate proteins can be slowed or blocked by a number of energetically stabilizing events, including deubiquitination, ligand binding, or stabilizing mutation.

This model has implications for a number of different processes, including the engineering of substrate degradation via Proteolysis Targeting Chimeras (PROTACs) (Sakamoto et al., 2001). PROTACs are synthetic molecules containing two moieties, a ligand binding the target protein to be degraded and another ligand with affinity for an E3 ubiquitin ligase that facilitates ubiquitination of the target. The linker length between the two ligands has been found to affect whether the target protein is degraded (Nowak et al., 2018), likely because it determines which lysines on the target are ubiquitinated in a manner that facilitates delivery to the downstream processing enzymes (i.e. Cdc48/p97 and the proteasome)(Smith et al., 2019; Twomey et al., 2019), but also possibly depending on whether ubiquitination at these lysines destabilizes the target. Non-specific ligands that promiscuously bind to 50-100 protein kinases were found to facilitate the degradation of only a small subset of these kinases (Bondeson et al., 2018; Huang et al., 2018), which could also be due to which lysines are ubiquitinated on the different targets and whether these ubiquitinations are sufficiently destabilizing to allow degradation.

While it is clear that ubiquitination has site-specific effects on the energy landscape, the mechanisms for ubiquitin-induced destabilization and the population of partially-unfolded conformers remains unknown. Potential mechanisms include destabilization from reduced conformational entropy in the substrate, a ubiquitin-induced entropic pulling force, direct substrate-ubiquitin interactions, or the ubiquitin-induced population of an intermediate state. There are no clear patterns regarding the region or type of secondary structure within the substrate that is energetically sensitive to the attachment of ubiquitin, nor are the effects correlated with the substrate size, as previously suggested (Morimoto et al., 2016). It is reasonable to expect that the addition of a protein domain, such as ubiquitin, can alter the energetics and dynamics of a target protein in this manner. Biophysical studies of multidomain proteins have demonstrated that the stability of one domain can be modulated by the presence of another (Batey et al., 2008). In differentially-linked polyubiquitin

chains, the ubiquitin monomers themselves can have different thermodynamic and mechanical stabilities (Carrion-Vazquez et al., 2003; Morimoto et al., 2015). Studies on N-terminal ubiquitin fusions and disulfide-linked ubiquitin attachments have reported small changes in the midpoints for thermally-induced unfolding depending on the modification (Morimoto et al., 2016).

Computational studies have postulated that ubiquitin-induced destabilization is a result of a decrease in a substrate's overall conformational entropy (Gavrilov et al., 2015). Site-specific effects could be realized through the difference in the potential flexibility at the different sites. The local structure and packing at the three different ubiquitination sites in barstar, however, do not reveal any notable differences in the density of atomic contacts or number of contacting residues (PDB: 1BTA). Detailed calculations or experiments evaluating these potential changes in conformational entropy are needed to evaluate this hypothesis.

Our results do not yield specific information about a potential entropic pulling force. NMR studies of the protein FKBP12 with chemically conjugated ubiquitin demonstrated increased backbone flexibility (Morimoto et al., 2016), which could be rationalized by an entropic pulling model whereby a highly stable protein fold, like ubiquitin, attached through a native isopeptide bond with many degrees of translational and rotational freedom, can provide a net pulling force on the substrate from the site of ligation (Sousa and Lafer, 2019).

The energetic modulation may also arise from direct interactions between the ubiquitin and the substrate. Ubiquitin has multiple exposed hydrophobic patches, one near Ile44 and another at Ile36, which could potentially stabilize exposed hydrophobic residues on a partially-unfolded substrate. The Ile44 hydrophobic patch is known to interact with PCNA when in an N-terminal fusion (Freudenthal 2010) and is responsible for the inter-ubiquitin interactions that give K48-linked ubiquitin chains their compact conformation (Eddins et al., 2007; Varadan et al., 2002). Ubiquitin also contains an acidic patch that electrostatically interacts with some target proteins (Debelouchina et al., 2017). In sum, how exactly ubiquitin destabilizes the substrate protein remains unknown and will require further investigation.

Cellular proteostasis relies upon careful regulation of protein degradation via the UPS, and the consequences of aberrant degradation are severe. We find that ubiquitin directly modulates a protein's conformational energy landscape, and these energetic changes play a pivotal role in regulating both 26S proteasome substrate selection and degradation kinetics. We conclude that ubiquitin signaling and proteasomal degradation overall are dependent on the biological and biophysical contexts of individual ubiquitinated proteins. A full understanding of the energetic effects contributed by a particular ubiquitination event is therefore crucial for building a complete model of how ubiquitin-mediated signals are transduced *in vivo*. We hope the tools and results presented herein can facilitate addressing these questions and be used to expand our model of the biophysical factors governing ubiquitin-mediated signaling.

Materials and Methods

Preparation of substrate proteins

E. coli BL21 Rosetta 2 (DE3) cells were transformed with either pEC072 (single-lysine *src*SH3), pEC074 (*M. smegmatis* DHFR), pEC076 (barstarK2), pEC062 (barstarK60), pEC081 (barstarK60/E80A), or pEC059 (barstarK78). Cells were then grown in 2 L LB Broth (Fisher) to 0.4 < OD_{600} < 0.8 and induced with 1 mM IPTG for 3 hours at 37°C. Bacteria were then pelleted and resuspended in 50 mM HEPES pH 7.0, 150 mM NaCl, 0.5 mM TCEP supplemented with 1X Halt™ protease inhibitor cocktail (Thermo) and benzonase (Novagen). Resuspended cells were lysed by sonication and the lysate was clarified by centrifugation at 20,000 rcf, 4°C, 30 minutes. The substrate was first purified by Ni^{2+}-NTA affinity chromatography using its N-terminal His_6 tag. Clarified lysate was allowed to batch bind to HisPur™ Ni^{2+}-NTA resin (Thermo) washed with 50 mM HEPES pH 7.0, 150 mM NaCl, 25 mM imidazole, 0.5 mM TCEP and eluted with 50 mM HEPES pH 7.0, 150 mM NaCl, 500 mM imidazole, 0.5 mM TCEP. Concentration of protein in the eluate was then measured using UV-Vis absorption at 280 nm. Eluate was then labeled for 2 hours at room temperature with 5X molar excess fluorescein-maleimide dye (Thermo). The labeling reaction was quenched with 10X molar excess DTT and unreacted dye was removed using a S200 16/60 size exclusion column (GE) pre-equilibrated with 25mM HEPES pH 7.5, 150 mM KCl, and 15 mM MgOAc. Peak corresponding to the labeled, full length His-MBP substrate was collected, and quantified by UV-Vis absorption at 280 nm and 495 nm according to the manufacturer's instructions before addition of 10% glycerol and flash freezing to store at -80°C for future use.

Preparation of substrate proteins with C-terminal ssrA tag/cyclin B engageable tail

E. coli BL21 Rosetta 2 (DE3) cells were transformed with either pEC098 (barstarK2), pEC093 (barstarK60), pEC097 (barstarK78). Cells were then grown in 2 L LB Broth (Fisher) to 0.4 < OD_{600} < 0.8 and induced with 1 mM IPTG for 3 hours at 37°C. Bacteria were then pelleted and resuspended in 50 mM HEPES pH 7.0, 150 mM NaCl, 0.5 mM TCEP supplemented with 1X Halt™ protease inhibitor cocktail (Thermo) and benzonase (Novagen). Resuspended cells were lysed by sonication and the lysate was clarified by centrifugation at 20,000 rcf, 4°C, 30 minutes. The substrate was first purified by Ni^{2+}-NTA affinity chromatography using its N-terminal His_6. Clarified lysate was allowed to batch bind to HisPur™ Ni^{2+}-NTA resin (Thermo) washed with 50 mM HEPES pH 7.0, 150 mM NaCl, 25 mM imidazole, 0.5 mM TCEP and eluted with 50 mM HEPES pH 7.0, 150 mM NaCl, 500 mM imidazole, 0.5 mM TCEP + 1X Halt™ protease inhibitor cocktail. Eluate was diluted 1:2 with 50 mM HEPES pH 7.0, 150 mM NaCl, and 0.5 mM TCEP and 5 mM EDTA was added. Eluate was then batch bound to *Strep*-Tactin Superflow Plus resin (Qiagen), washed with 50 mM HEPES pH 7.0, 150 mM NaCl and eluted with 50 mM HEPES pH 7.0, 150 mM NaCl, 2.5mM desthiobiotin (Sigma). Eluate was labeled with 5X molar excess fluorescein-maleimide dye (Thermo). The labeling reaction was quenched with 10X molar excess DTT and unreacted dye was removed using a S200 16/60 size exclusion column (GE) pre-equilibrated with 25mM HEPES pH 7.5, 150 mM KCl, and 15 mM MgOAc. The peak corresponding to the labeled, full length, labeled His-MBP substrate was collected, and quantified by UV-Vis absorption at 280 nm and 495 nm according to the manufacturer's instructions before addition of 10% glycerol and flash freezing to store at -80°C for future use.

Preparation of ubiquitin

E. coli BL21 Rosetta 2 (DE3) cells were transformed with pEC086. Cells were then grown in 2 L LB Broth (Fisher) to $0.4 < OD_{600} < 0.8$ and induced with 1 mM IPTG for 3 hours at 37°C. Bacteria were then pelleted and resuspended in 20 mM sodium acetate pH 5.1 (pH adjusted with acetic acid). Resuspended cells were lysed by sonication and the lysate was clarified by centrifugation at 20,000 rcf, 4°C, 30 minutes. Clarified lysate was loaded onto a HiPrep™ SP XL 16/10 cation exchange column (GE) preequilibrated in 20 mM sodium acetate pH 5.1. Column was washed with 5 column volumes of 20 mM sodium acetate pH 5.1 and then eluted with a gradient of 20 mM sodium acetate to 500 mM sodium acetate pH 5.1. The peak corresponding to WT ubiquitin was collected and further purified by size exclusion on an S75 16/60 column (GE) preequilibrated with 50 mM Tris pH 7.5, 150 mM NaCl. Peak corresponding to WT ubiquitin was collected, and quantified by UV-Vis absorption at 280 nm before flash freezing to store at -80°C for future use.

Preparation of barnase

E. coli BL21 Rosetta 2 (DE3) cells were transformed with pEC099. Cells were then grown in 2 L LB Broth (Fisher) to $0.4 < OD_{600} < 0.8$ and induced with 1 mM IPTG for 3 hours at 37°C. Bacteria were then pelleted and resuspended in 50 mM HEPES pH 7.0, 150 mM NaCl, 0.5 mM TCEP supplemented with 1X Halt protease inhibitor cocktail (Thermo) and benzonase (Novagen). Resuspended cells were lysed by sonication and the lysate was clarified by centrifugation at 20,000 rcf, 4°C, 30 minutes. The substrate was first purified by Ni^{2+}-NTA affinity chromatography using its N-terminal His_6. Clarified lysate was allowed to batch bind to HisPur™ Ni^{2+}-NTA resin (Thermo) washed with 50 mM HEPES pH 7.0, 150 mM NaCl, 25 mM imidazole, 0.5 mM TCEP and eluted with 50 mM HEPES pH 7.0, 150 mM NaCl, 500 mM imidazole, 0.5 mM TCEP. HRV3C-protease was added and the cleavage reaction was allowed to proceed overnight at 4°C under dialysis to 50 mM HEPES pH 7.0, 150 mM NaCl, 0.5 mM TCEP. HRV3C-protease and His-MBP tags were removed using a subtractive Ni^{2+}-NTA purification step. Flow through was further purified by size exclusion chromatography using a S75 16/60 column (GE). Peak corresponding to barnase was collected, and quantified by UV-Vis absorption at 280 nm before addition of 10% glycerol and flash freezing to store at -80°C for future use.

Preparation of ubiquitination enzymes

Ubiquitination machinery *M. musculus* mE1, *S. cerevisiae* Ubc4, and *S. cerevisiae* Rsp5 were purified as described previously using the same procedure (Bard et al., 2019; Worden et al., 2017). *E. coli* BL21 Rosetta 2 (DE3) pLysS cells were transformed with pAM235 (mE1) or pAM236 (Ubc4) or pAM237 (Rsp5) and grown at 37°C in 6L of terrific broth (Novagen) until $OD_{600} = 0.8$ before expression was induced with 1 mM IPTG and allowed to continue overnight at 18°C. Cells were resuspended in 50 mM HEPES pH 7.6, 250 mM NaCl supplemented with protease inhibitors (pepstatin A, aprotonin, PMSF, and leupeptin), benzonase, and lysozyme (2 mg/mL) and stored at -80°C. Resuspended cells were thawed and lysed by sonication before lysate was clarified by centrifugation at 20,000 rcf for 30 mins at 4°C. Clarified lysate was batch bound to HisPur™ Ni^{2+}-NTA resin (ThermoFisher) equilibrated with 50 mM HEPES pH 7.6, 250 mM NaCl for one hour at 4°C. Resin was washed in a gravity flow column with at least 50 mL of 50 mM HEPES pH 7.6, 250 mM NaCl, 20 mM imidazole before protein was eluted with 50 mM HEPES pH 7.6, 250 mM NaCl, 250 mM imidazole. Eluate was concentrated in an Amicon spin concentrator (Millipore) and loaded onto a

Superdex200 16/60 size exclusion column (GE) equilibrated in 20 mM HEPES pH 7.6, 100 mM NaCl, 10% glycerol. Peak corresponding with target protein was collected, concentrated in Amicon spin concentrator (Millipore), quantified by absorbance at 280 nm, and flash frozen in liquid nitrogen for storage at -80°C.

Preparation of AMSH deubiquitinase

E. coli BL21 Rosetta 2 (DE3) pLysS cells were transformed with pAM241 and grown in 2 L of terrific broth (Novagen) at 37°C until OD_{600} = 0.6 after which expression was induced with 0.5 mM IPTG overnight at 18°C. Cells were resuspended in 50 mM HEPES pH 7.6, 250 mM NaCl supplemented with protease inhibitors (pepstatin A, aprotonin, PMSF, and leupeptin), benzonase, and lysozyme (2 mg/mL) and stored at -80°C. Resuspended cells were thawed and lysed by sonication before lysate was clarified by centrifugation at 20,000 rcf for 30 mins at 4°C. Clarified lysate was batch bound to HisPur^{TM} Ni^{2+}-NTA resin (ThermoFisher) equilibrated with 50 mM HEPES pH 7.6, 250 mM NaCl for one hour at 4°C. Resin was washed with 50 mM HEPES pH 7.6, 250 mM NaCl, 10 mM ATP (to remove contaminating DnaK), 20 mM imidazole. The His$_6$ tag was cleaved from AMSH by HRV3C-protease overnight at 4°C and AMSH was clarified through an ortho Ni^{2+}-NTA step using HisPur Ni^{2+}-NTA resin (ThermoFisher). Protein was concentrated in Amicon spin concentrator (Millipore) before being loaded on a S75 16/60 size exclusion column (GE) equilibrated with 20 mM HEPES pH 7.6, 100 mM NaCl, 10% glycerol. Peak corresponding to AMSH was collected, concentrated in an Amicon spin concentrator (Millipore), quantified by absorbance at 280 nm, and flash frozen in liquid nitrogen for storage at -80°C.

Preparation of homogenous mono-ubiquitinated substrate proteins

Substrate proteins, ubiquitin, ubiquitination enzymes, and AMSH were prepared as described above. Ubiquitination reactions were set up in reaction buffer (50 mM HEPES pH 8.0, 150 mM NaCl, 5 mM MgCl$_2$, and 5% glycerol) in 20 µL aliquots as follows: 5 µM Uba1 (E1), 5 µM Ubc4 (E2), 5 µM Rsp5 (E3), 20 µM substrate, 750 µM wild-type (non-methylated) ubiquitin or methylated ubiquitin, 5 mM ATP and incubated in a thermocycler for 3 hours at 25°C. 48 individual 20 µL reactions were performed for a typical prep. After three hours, reactions were pooled and HRV3C-protease was added and allowed to cleave overnight at 4°C. If wild-type (non-methylated) ubiquitin was used, reactions were then treated with 0.5 µM AMSH for 30 minutes at room temperature and quenched with 5 mM EDTA. His-tagged ubiquitination machinery and the His-MBP scaffold were then removed via a subtractive Ni^{2+}-NTA affinity step using a 1 mL HisTrap HP column (GE) pre-equilibrated with 50 mM HEPES pH 7.0, 150 mM NaCl, 25 mM imidazole. This removed most, but not all, of the His-tagged ubiquitination machinery and ubiquitinated His-MBP substrate scaffold. Flow through was then concentrated and loaded onto an S75i 10/300 size exclusion column (GE) pre-equilibrated with 25 mM HEPES pH 7.5, 150 mM KCl, and 15 mM MgOAc. The peak corresponding to the mono-ubiquitinated substrate was collected, concentrated, and quantified by UV-Vis absorption at 280 nm and 495 nm according to the manufacturer's instructions before addition of 10% glycerol and flash freezing to store at -80°C for future use.

Preparation of mono-ubiquitinated substrate proteins with C-terminal ssrA tag/engageable tail

Substrate proteins and ubiquitination enzymes were prepared as described above. Ubiquitination reactions were set up in reaction buffer (50 mM HEPES pH 8.0, 150 mM NaCl, 5 mM MgCl$_2$, and 5% glycerol) in 20 µL aliquots as follows: 5 µM Uba1 (E1), 5 µM Ubc4 (E2), 5 µM Rsp5 (E3), 20 µM substrate, 500 µM methylated ubiquitin (Millipore), 5 mM ATP and incubated in a thermocycler for 3 hours at 25°C. 24 individual 20 µL reactions were performed for a typical prep. After three hours, reactions were pooled and HRV3C-protease was added and allowed to cleave for 30 minutes at room temperature. Ubiquitination enzymes and His-MBP were removed by batch binding to MagneHis™ (Promega) magnetic Ni^{2+}-NTA resin for 1 hour at 4°C. Resin was pelleted in a magnetic tube rack, and the supernatant was collected for gel based single-turnover ubiquitin-independent degradation assays.

Preparation of proteasome lid subcomplex

Lid subcomplex was recombinantly expressed and purified as described previously(Bard et al., 2019). *E. coli* BL21-star(DE3) (Invitrogen) cells were transformed with pAM80, pAM85, and pAM86 for lid. pAM80 encodes for Sem1 and rare tRNA codons, pAM85 encodes Rpn5, MBP-HRV3C-Rpn6, Rpn8, Rpn11, and Rpn9, and pAM86 encodes Rpn3, His$_6$-HRV3C-Rpn12, and Rpn7. Cells were grown in 2 L of terrific broth (Novagen) at 37°C until $1.0 < OD_{600} < 1.5$ after which expression was induced with 1 mM IPTG at 16°C for overnight. Bacteria were pelleted and resuspended in 60 mM HEPES pH 7.6, 50 mM NaCl, 50 mM KCl, 10 mM MgCl$_2$, 5% glycerol and supplemented with protease inhibitors (aprotonin, pepstatinA, leupeptin, and PMSF or AEBSF), benzonase (Novagen), and 2 mg/mL lysozyme and stored at -80°C. Resuspended cells were lysed by sonication and the lysate was clarified by centrifugation at 20,000 rcf, 4°C, 30 minutes. Lid was first purified by Ni^{2+}-NTA affinity chromatography via His$_6$-HRV3C-Rpn12 using a 5mL HisTrap HP (GE) column, washed with 60 mM HEPES pH 7.6, 50 mM NaCl, 50 mM KCl, 10 mM MgCl$_2$, 5% glycerol, 20 mM imidazole and eluted with 60 mM HEPES pH 7.6, 50 mM NaCl, 50 mM KCl, 10 mM MgCl$_2$, 5% glycerol, 250 mM imidazole. Eluate was further purified via MBP-HRV3C-Rpn6 and amylose resin (NEB) and eluted with 60 mM HEPES pH 7.6, 50 mM NaCl, 50 mM KCl, 10 mM MgCl$_2$, 5% glycerol, 10 mM maltose. Amylose eluates were cleaved with HRV3C-protease overnight at 4°C before being loaded onto a Sup6i 10/300 size exclusion column (GE) pre-equilibrated with 60 mM HEPES pH 7.6, 50 mM NaCl, 50 mM KCl, 10 mM MgCl$_2$, 5% glycerol, 0.5 mM TCEP. Peak corresponding to fully assembled lid was collected, concentrated, and quantified by UV-Vis spectroscopy before being flash frozen and stored at -80°C for future use.

Preparation of proteasome base subcomplex and SspB$_2$-fused base subcomplex

Base subcomplex was recombinantly expressed and purified as described previously (Beckwith et al., 2013). *E. coli* BL21-star(DE3) (Invitrogen) cells were transformed with pAM81, pAM83, and pAM82 for wild-type base or pAM81, pAM83, and pAM210 for SspB$_2$-Rpt2 base. pAM82 encodes for Rpt1, Rpt2, Rpt3, Rpt4, Rpt5, and Rpt6, pAM210 encodes Rpt1, SspB$_2$-Rpt2, Rpt3, Rpt4, Rpt5, and Rpt6, pAM81 encodes Rpn1, Rpn2, and Rpn13, and pAM83 encodes rare tRNA codons and base chaperones (Nas6, Nas2, Rpn14, and Hsm3). Cells were grown in 3 L of terrific broth (Novagen) at 37°C until $0.6 < OD_{600} < 0.8$ after which expression was induced with 1 mM IPTG at 30°C for 5 hours followed by 16°C overnight expression. Bacteria were pelleted and resuspended in 60 mM HEPES pH 7.6, 50 mM NaCl, 50 mM KCl, 10 mM MgCl$_2$, 5% glycerol, 1 mM ATP and supplemented with protease inhibitors (aprotonin, pepstatinA, leupeptin, and PMSF or AEBSF),

benzonase (Novagen), and 2 mg/mL lysozyme and stored at -80°C. Resuspended cells were lysed by sonication and the lysate was clarified by centrifugation at 20,000 rcf, 4°C, 30 minutes. Base was first purified by Ni^{2+}-NTA affinity chromatography via His_6-Rpt6 using a 5mL HisTrap HP (GE) column, washed with 60 mM HEPES pH 7.6, 50 mM NaCl, 50 mM KCl, 10 mM $MgCl_2$, 5% glycerol, 1 mM ATP, 20 mM imidazole and eluted with 60 mM HEPES pH 7.6, 50 mM NaCl, 50 mM KCl, 10 mM $MgCl_2$, 5% glycerol, 1 mM ATP, 250 mM imidazole. Eluate was further purified via FLAG-Rpt1 and anti-FLAG M2 affinity resin (Sigma) and eluted with 60 mM HEPES pH 7.6, 50 mM NaCl, 50 mM KCl, 10 mM $MgCl_2$, 5% glycerol, 1 mM ATP, 0.15 mg/mL FLAG peptide (Genscript). FLAG eluates were loaded onto a Sup6i 10/300 size exclusion column (GE) pre-equilibrated with 60 mM HEPES pH 7.6, 50 mM NaCl, 50 mM KCl, 10 mM $MgCl_2$, 5% glycerol, 1 mM ATP, 0.5 mM TCEP. Peak corresponding to fully assembled base was collected, concentrated, and quantified by Bradford assay (BioRad) using BSA (Sigma) as a standard before being flash frozen and stored at -80°C for future use.

Preparation of proteasome core particle

20S core particle from *S. cerevisiae* was purified as described previously (Matyskiela et al., 2013) from yeast strain yAM54 bearing 3X-FLAG-Pre1. yAM54 cells were grown in 3 L of YPD at 30°C until saturation (3 days). Cells were pelleted and resuspended in 60 mM HEPES pH 7.6, 500 mM NaCl, 10 mM $MgCl_2$, 5% glycerol, plunged into liquid nitrogen and subsequently stored at -80°C. Frozen resuspended cells were lysed using a 6875 Freezer Mill Dual Chamber Cryogenic grinder (SPEX Sample Prep). Lysate was diluted in 60 mM HEPES pH 7.6, 500 mM NaCl, 10 mM $MgCl_2$, 5% glycerol and clarified by centrifugation at 20,000 rcf, 4C, 45 minutes. Base was first purified by anti-FLAG affinity chromatography using anti-FLAG M2 affinity resin (Sigma), exhaustively washed with 60 mM HEPES pH 7.6, 500 mM NaCl, 10 mM $MgCl_2$, 5% glycerol, and eluted with 60 mM HEPES pH 7.6, 500 mM NaCl, 10 mM $MgCl_2$, 5% glycerol, 0.15 mg/mL FLAG peptide (Genscript). Eluate was loaded onto a Sup6i 10/300 size exclusion column (GE) pre-equilibrated with 60 mM HEPES pH 7.6, 50 mM NaCl, 50 mM KCl, 10 mM $MgCl_2$, 5% glycerol, 0.5 mM TCEP. Peak corresponding to fully assembled core was collected, concentrated, and quantified by UV-Vis spectroscopy before being flash frozen and stored at -80°C for future use.

Determination of global substrate stability by intrinsic tryptophan fluorescence

Two 5 µM protein stocks were prepared: A no denaturant protein stock and a high urea protein stock both in 25 mM HEPES pH 7.5, 150 mM KCl, and 15 mM MgOAc. The exact urea concentration in the high denaturant stock was determined by taking the refractive index. Samples with a range of urea concentrations were prepared by serial dilution of the two stocks and allowed to equilibrate at room temperature overnight. Measurements were then performed at 25°C using a PTI Quantamaster Fluorometer (Horiba). Tryptophan fluorescence was excited at 295 nm and a 10 second kinetic read of fluorescence emission at both 330 nm and 350 nm was performed at each denaturant concentration. Samples were recovered from the cuvette after each measurement and the exact urea concentration was determined by taking the refractive index. The signal was averaged over each 10 second period and reported as a ratio of average signal 330/average signal 350. Ratios were then normalized using equation 1 and each mono-ubiquitinated and unmodified variant were globally fit with linked baselines to a two state folding model (equation 2) using Igor Pro 7, which allowed determination of the C_m, $\Delta G_{unfolding}$, and *m*-value.

(1) y-y$_D$/y$_N$-y$_D$

(2) y = (m1+m5*x)*(1/(1+(exp(-(m3-m4*x)/RT))))+(m2+m6*x)*(exp(-(m3-m4*x)/RT)/(1+(exp(-(m3-m4*x)/RT)))

Parameter definitions:
m1=folded intercept, m2 = unfolded intercept, m3 = $\Delta G_{unfolding}$, m4 = *m*-value, m5= folded baseline slope, m6=unfolded baseline slope

Determination of substrate native-state energetics by native-state proteolysis

Ubiquitinated substrate sample prep was performed as described above except that AMSH deubiquitinase was allowed sufficient time to leave a mixed population of unmodified and mono-ubiquitinated species. Additionally, the final size exclusion step was omitted. Protein stocks were prepared in a 2 mL volumetric flask with final buffer of 25 mM HEPES pH 7.5, 150 mM KCl, and 15 mM MgOAc. Samples were allowed to equilibrate at room temperature in the dark overnight. Native-state proteolysis experimental protocol was adapted from previous work(Park and Marqusee, 2004). The equilibrated stock was divided into 200 µL aliquots and thermolysin protease (stock concentration 10 mg/mL) was added to a final concentration of 0.04 to 0.4 mg/mL. Time points (15 µL) were taken at (no protease control, 0:15, 0:30, 0:45, 1:00, 1:30, 2:00, 3:00, 5:00, 7:00, and 10:00) from the reactions and quenched in 2.5 µL of 0.5 M EDTA. 2.5 µL of 6X SDS-PAGE loading buffer was added to each sample and time points were run out on a 12% NuPAGE Bis-Tris™ gel (Invitrogen) in 1X MES running buffer (50 mM MES, 50 mM Tris Base, 0.1% SDS, 1 mM EDTA). Gels were imaged using a BioRad ChemiDoc™ and color inverted using the "Invert" command in ImageJ for ease of viewing and analysis. Band intensities of the unmodified and mono-ubiquitinated substrate bands were then quantified using ImageJ. SH3 and mono-ubiquitinated SH3 gels were quantified in ImageQuant (GE Healthcare) with a rolling ball background subtraction because proteolysis products could comigrate near full length protein. Band intensities were normalized to the no protease lane and fit to a first order exponential (equation 3) using IgorPro 7 to calculate the observed proteolysis kinetics (k_{obs}). For a given substrate, k_{obs} was determined at several thermolysin concentrations and plotted against protease concentrations. $\Delta\Delta G_{proteolysis}$ was calculated from the slope of the linear fit to thermolysin vs. k_{obs}. using equation 4 and equation 5. Individual $\Delta G_{proteolysis}$ could also be calculated using equation 6 and the measured k_{cat}/K$_M$ of thermolysin for a generic protein of 99,000 M^{-1}s^{-1} (Park and Marqusee, 2004).

(3) y = y$_0$ + A*exp(-(x-x$_0$)/τ_{obs})

(4) k_{obs} = K$_{op}$ (k_{cat}/K$_M$) [E] = 1/τ_{obs}
         slope of k_{obs} vs. [E] linear fit = K$_{op}$ (k_{cat}/K$_M$)

(5) $\Delta\Delta G_{proteolysis}$ = -RT*ln(K$_{op, mono-ubiquitinated}$ (k_{cat}/K$_M$) /K$_{op, unmodified}$ (k_{cat}/K$_M$))

(6) $\Delta G_{proteolysis}$ = -RT*ln(K$_{op}$ (k_{cat}/K$_M$)/99,000 M^{-1}s^{-1})

Cy5-methotrexate binding to DHFR by fluorescence polarization

Equilibrium binding of Cy5-methotrexate to *M. smegmatis* DHFR was assessed by monitoring the increase in fluorescence polarization of Cy5-methotrexate upon binding DHFR. 50 nM Cy5-methotrexate was incubated with increasing concentration of unmodified or mono-ubiquitinated DHFR (quantified by fluorescein fluorescence using a standard curve) in 60 mM HEPES pH 7.6, 50 mM NaCl, 50 mM KCl, 10 mM MgCl$_2$, 5% glycerol, 0.5 mM TCEP for 20 minutes at room temperature to reach equilibrium. Fluorescence polarization was monitored for 5 minutes on a Synergy Neo2 multi-mode plate reader. Time points were averaged and normalized to Cy5-methotrexate in the absence of DHFR. For the unmodified DHFR, K_d was determined by fitting the change in fluorescence polarization as a function of DHFR concentration to simple single site binding model (Pollard 2010) (Equation 7).

(7) Polarization = [DHFR] * maxPolarization / (K_d + [DHFR])

Preparation of polyubiquitinated barstar variants

Barstar ubiquitination was performed exactly as above except that AMSH removal of K63-linked polyubiquitin chains was omitted. Ortho-Ni^{2+} purified ubiquitinations were subsequently separated by size-exclusion chromatography on an S200i 10/300 (GE Healthcare) and 0.5 mL fractions were assessed for degradable species by incubating with proteasome under single turnover conditions at 30°C for 30 minutes and analyzing products by SDS-PAGE (Supplementary Fig. 9b).

Gel-based single-turnover ubiquitin-independent degradation assay

2X stocks of substrate (300 nM final) were prepared in assay buffer (60 mM HEPES pH 7.6, 50 mM NaCl, 50 mM KCl, 10 mM MgCl2, 0.5 mM TCEP, 5 mM ATP, 5% glycerol, 1 mg/ml BSA). 2X proteasome stocks were performed by reconstituting recombinant lid (5 μM final), recombinant SspB$_2$-Rpt2 base (5 μM final), recombinant Rpn10 (5 μM final), and core particle (2.5 μM final) in assay buffer with an ATP-regeneration system (creatine kinase, creatine phosphate, and 5 mM ATP) and allowed to assemble for 3 minutes at room temperature. Reactions were performed in technical triplicate at 30°C in a thermocycler and initiated by mixing equivolume (12.5 μL) of 2X substrate with 2X proteasome. Time points (1.2 μL) were taken at (0:10, 0:20, 0:30, 0:45, 1:00, 1:30, 2:00, 3:00, 5:00, 10:00, 15:00, 20:00, 30:00 min) from the reactions and quenched in 5 μL of 2X SDS-PAGE loading buffer (125 mM TrisHCl pH 6.8, 20% glycerol, 4% SDS). Gel samples were separated by electrophoresis on 4-20% TGX gels (Bio-Rad) before fluorescence imaging on a typhoon variable mode scanner (GE) with 50 μm per pixel density. Images were quantified in ImageQuant (GE) by normalizing band intensity of each species per total lane intensity to account for loading variation. Quantified species were plotted as percent total signal (Supplementary Fig. 7c) and fit to a single exponential equation (Equation 3) in IgorPro7. For degradations performed with ATPγS, proteasomes were assembled in ATP for 3 minutes at room temperature, then ATPγS was added (5 mM final) for 3 minutes at room temperature prior to substrate addition. For degradations using only the core particle, core particle was added to 900 nM final with substrate and incubated at 30°C for the indicated time points. Time points of 0, 10:00, and 30:00 minutes were quenched in SDS-PAGE loading buffer for trials involving core particle only or ATPγS inhibited proteasome and separated by SDS-PAGE on 4-20% and assess qualitatively.

Fluorescence polarization single-turnover ubiquitin-independent degradation assay

For ubiquitin-independent degradations assessed by fluorescence polarization, reactions were initiated with equivolume (2.5 µL) addition of substrate to proteasome directly within a 384-well black bottom plate (Corning) and fluorescence polarization was monitored in a Synergy Neo2 multimode plate reader (BioTek). Decreased fluorescence polarization over time as substrate was processed into peptides could also be fit to a single exponential model (Equation 3) in IgorPro7.

Fluorescence polarization single-turnover ubiquitin-dependent degradation assay of Ub_n barstar variants

Substrates were prepared to 2X concentration (6 nM final) in assay buffer. Proteasome was reconstituted to 2X concentration in assay buffer (2.5 µM lid, base, and Rpn10 with 0.9 µM core particle) and allowed to assemble for 3 minutes at room temperature prior to reaction initiation. Reactions were initiated with appropriate dilution of 2X substate (2.5 µL) into 2X proteasome (2.5 µL) in a 384-well black bottom plate (Corning) and the decrease of fluorescence polarization over time was monitored on a Synergy Neo2 multimode plate reader (BioTek). Trials were repeated for n=3. Where exponential decay was observed, curves could be fit to a single exponential model (Equation 3) in IgorPro7. For reactions performed with core particle only, core particle was made to 2X concentration (1.8 µM) and added equivolume with 2X substrate (5 µL final) and fluorescence polarization was monitored as above. Single turnover conditions were verified by single reactions with doubled proteasome concentration by reconstituting proteasome to 4X concentration and diluting with equivolume substrate (2.5 µl each) to 2X proteasome and monitoring fluorescence polarization kinetics as described above. For degradations with *o*-phenanthroline inhibited proteasomes, proteasomes were allowed to assemble at 3X concentration for 3 minutes at room temperature between dilution with *o*-phenanthroline (30 mM stock in assay buffer; 5 mM final) to 2X concentration for 2 minutes before degradation initiation as described above. For degradations using only the core particle, core particle was added to 900 nM final with substrate as described above.

Fluorescence polarization single-turnover ubiquitin-dependent degradation assay of substrates in the presence of barnase

Substrates were prepared to 2X concentration (6 nM final) in assay buffer with barnase added in excess (20 µM final) and allowed to come to equilibrium for greater than 5 minutes at room temperature (Pollard 2010) prior to degradation initiation. Degradations were performed exactly as described above. Saturation of barnase binding was assessed by doubling barnase concentration (40 µM final) and comparing fluorescence polarization kinetic differences. FAM-Titin-I27^{V13P,V15P} ubiquitinated as described above was degraded in the presence or absence of 20 µM barnase with proteasome at the same concentration as described.
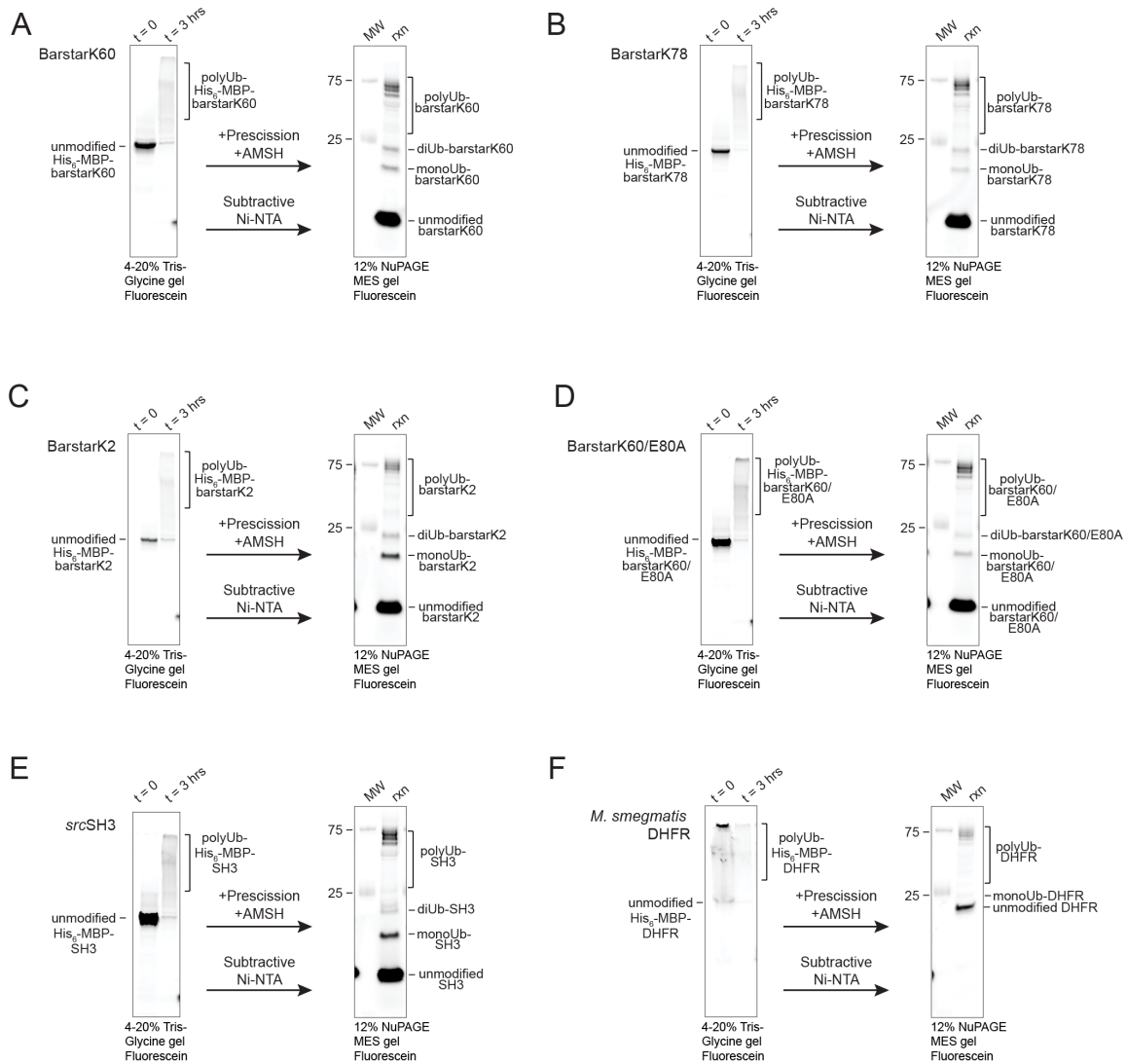
Figure s3.1. Reconstituted *in vitro* ubiquitination system for diverse single-lysine substrates. (**a-f**) Representative fluorescence scans of SDS-PAGE gels showing the full-length substrates immediately after reaction initiation and after 3 hours of ubiquitination. Reactions were treated with Prescission (HRV3C) protease and AMSH deubiquitinase prior to subtractive Ni^{2+}-NTA chromatography to reveal clearly defined mono- and di-ubiquitinated substrate with native isopeptide linkages. All experiments were repeated at least five times with similar results.
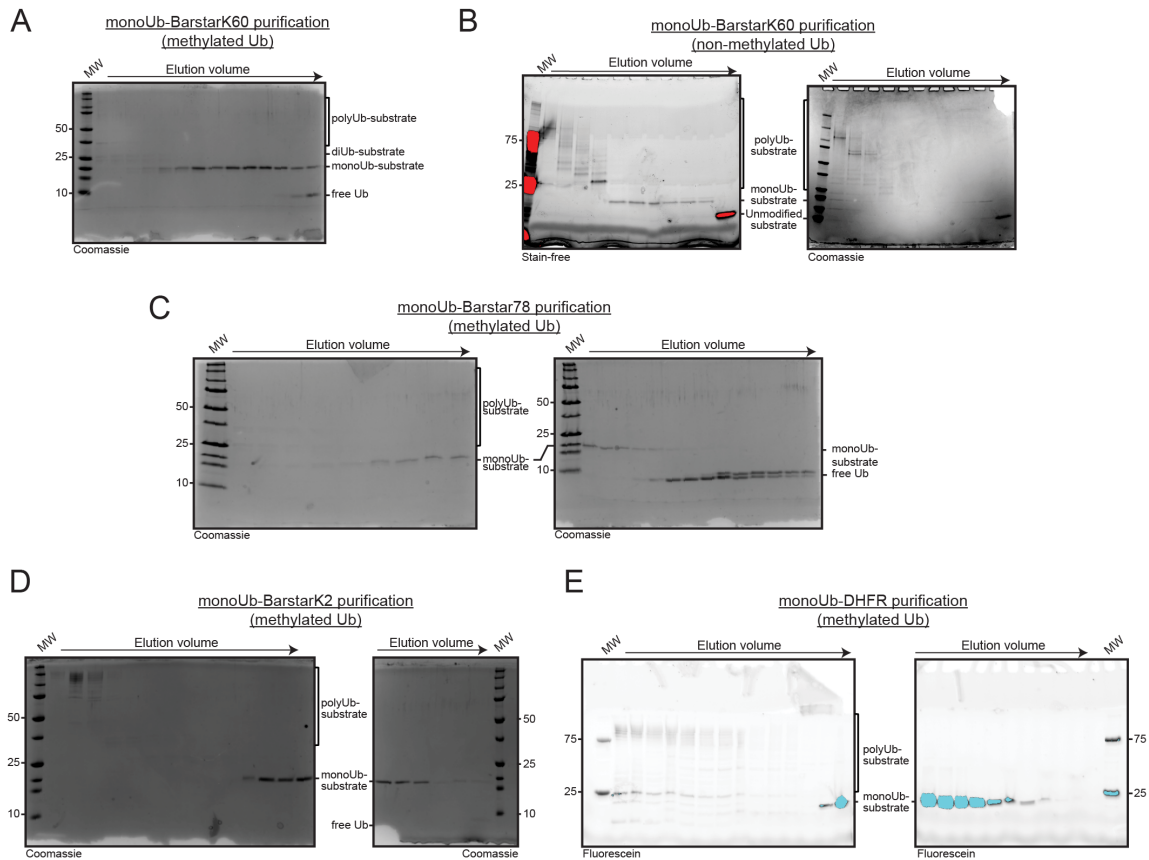
Figure s3.2. SDS-PAGE gels showing size exclusion chromatography fractions for purified monoUb-substrates. Representative gels (with indicated imaging modalities) of selected S75 size exclusion chromatography fractions from purification of monoUb-barstarK60 proteins with methyl-ubiquitin (**a**) or non-methylated ubiquitin (**b**) conjugation. Representative gels (with indicated imaging modalities) of selected S75 size exclusion chromatography fractions from purifications of methyl-ubiquitinated monoUb-barstarK78 (**c**) monoUb-barstarK2 (**d**) or monoUb-DHFR (**e**). Experiments **a**-**d** were repeated at least once with similar results.
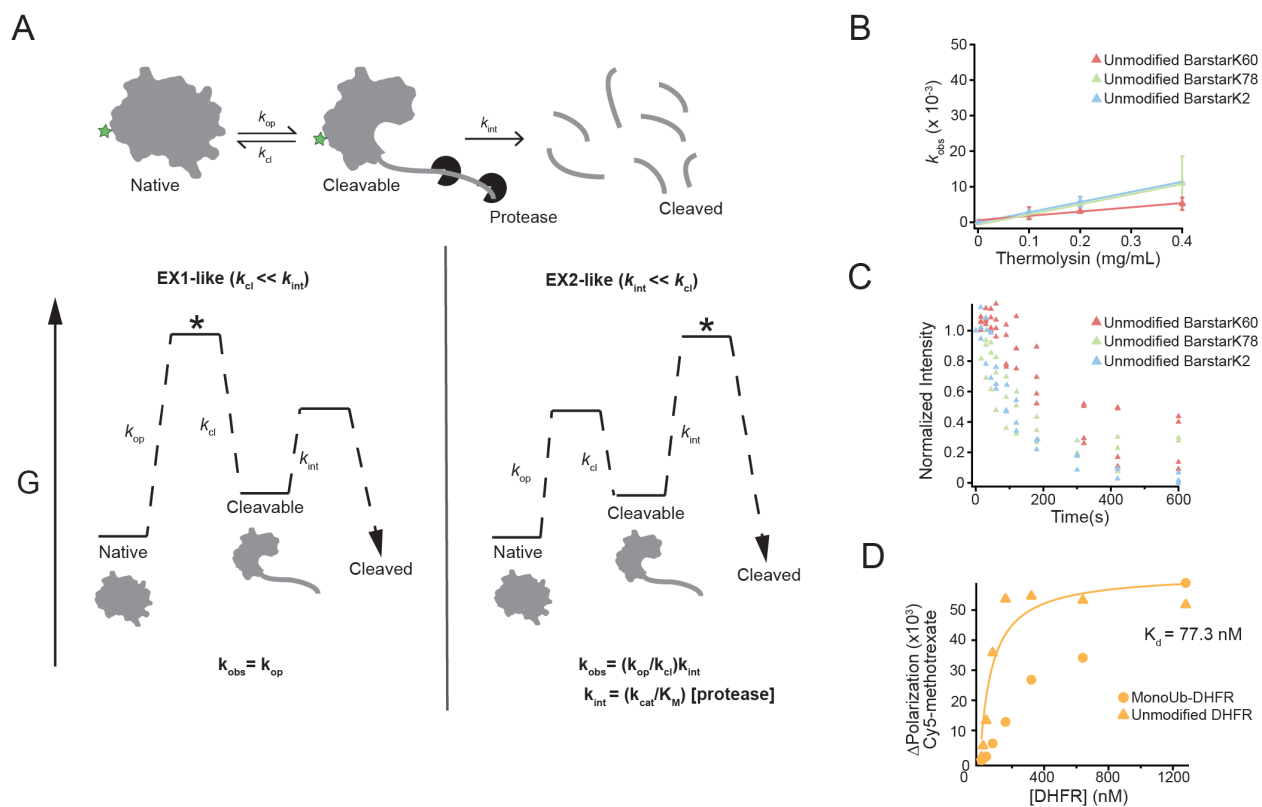
76

Figure s3.3. Explanation of native-state proteolysis for investigating the energetics of partial unfolding and validation of native-state proteolysis with these systems. (**a**) EX1 and EX2-like kinetic regimes for native-state proteolysis. In EX1-like experiments, the conformational change between the native and cleavable states is the rate-limiting step, and $k_{obs} = k_{op}$. In EX2-like experiments, as shown in Fig. 2, the proteolysis of the cleavable state is the rate-limiting step, and $k_{obs} = K_{op}(k_{cat}/K_M)$[protease]. (**b**) Fits of thermolysin concentration vs. mean k_{obs} for unmodified barstarK2 (n=3), barstarK60 (n=4), and barstarK78 (n=3) show a linear dependence within error (standard deviation). Individual data points are presented in **Fig. 2**. (**c**) Example individual data points for time courses of unmodified barstarK2 (n=3), K60 (n=4), and K78 (n=3) at 0.2 mg/mL thermolysin showing the similarity of k_{obs} for the three unmodified barstar variants. (**d**) Binding curve for unmodified *M. smegmatis* DHFR and monoUb-*M. smegmatis* DHFR to Cy5-methotrexate measured by Cy5 fluorescence polarization (n=1).
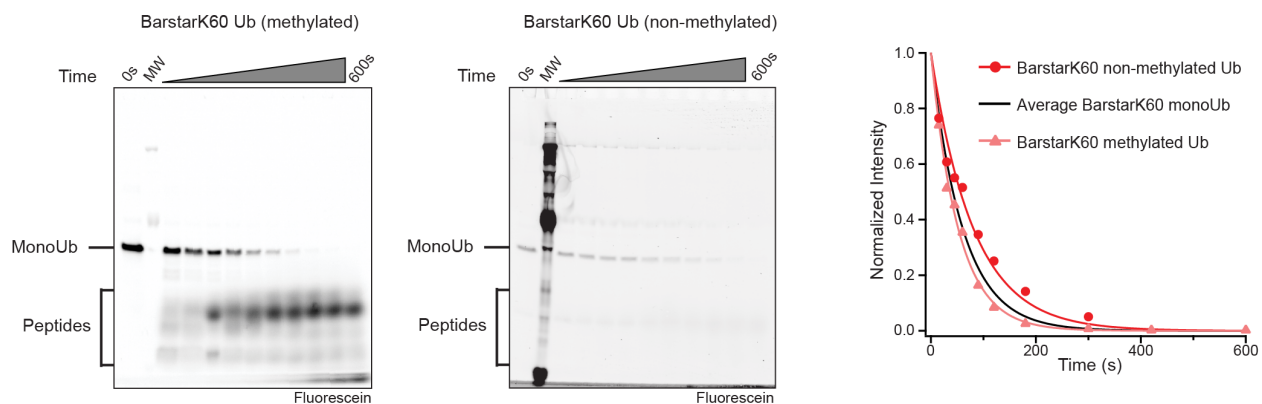
Figure s3.4. Comparison of non-methylated monoUb and methylated monoUb modifications on barstar.
Fluorescein imaged gels and quantified band intensities for native-state proteolysis of barstarK60 substrate proteins at 0.2 mg/mL
thermolysin with either methylated monoUb or non-methylated monoUb modification. Quantified band intensities were fit to
Equation 3 (n=1) and overlaid with the calculated model presented in Figure 2b (n=4).
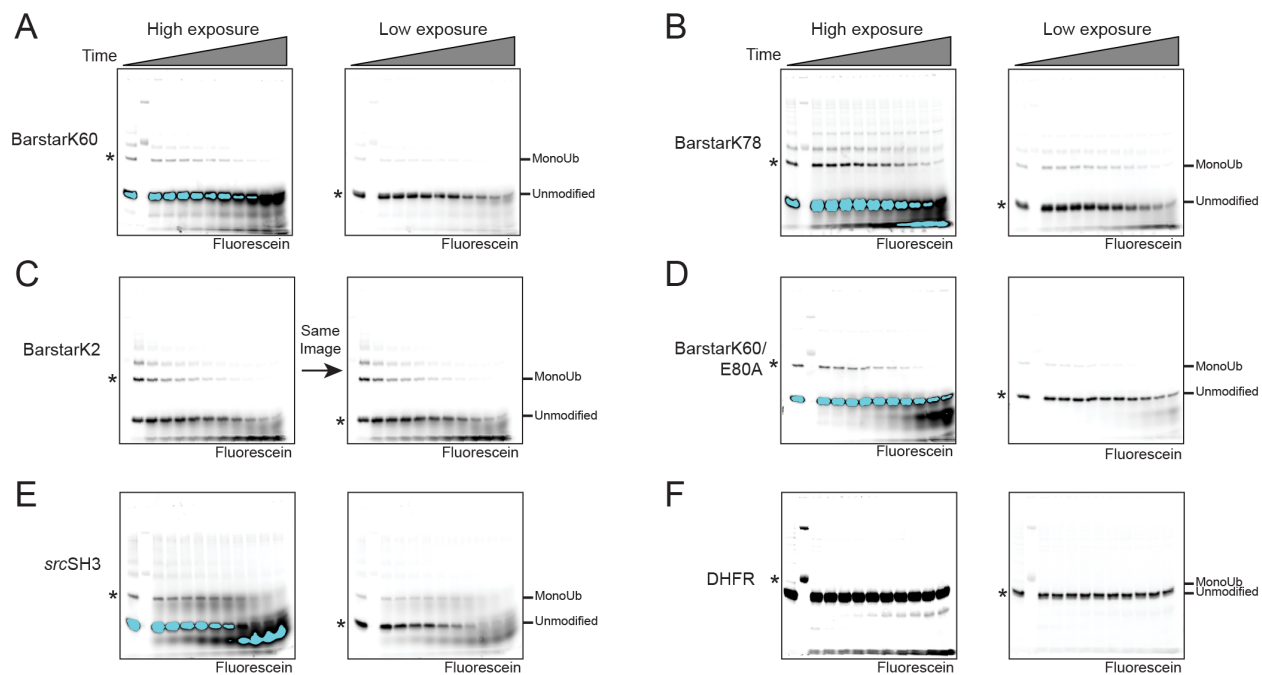

Figure s3.5. Full gel images from figure 2
Representatives of entire fluorescein-imaged gels for native-state proteolysis displayed in Figure 2 are shown at two exposures, where
necessary, for quantification of individual species indicated by "*". These experiments were repeated at least twice with similar results
(barstarK60, n=4; barstarK2, n=3; barstarK78, n=3; barstarK60/E80A, n=3; *src*SH3, n=3; DHFR, n=2).
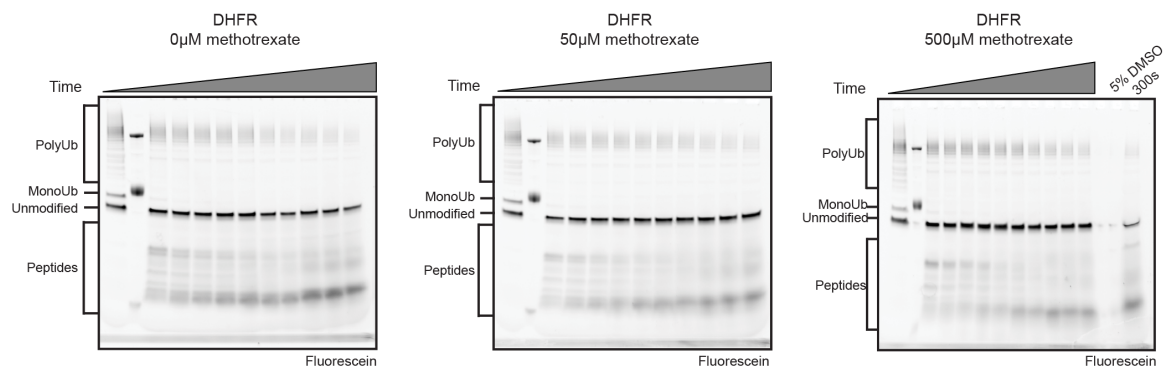
Figure s3.6. Methotrexate effect on monoUb-DHFR
Full fluorescein imaged gels for native-state proteolysis of monoUb-DHFR (0.2 mg/mL thermolysin) in the presence or absence of saturating concentrations of methotrexate (n=1).
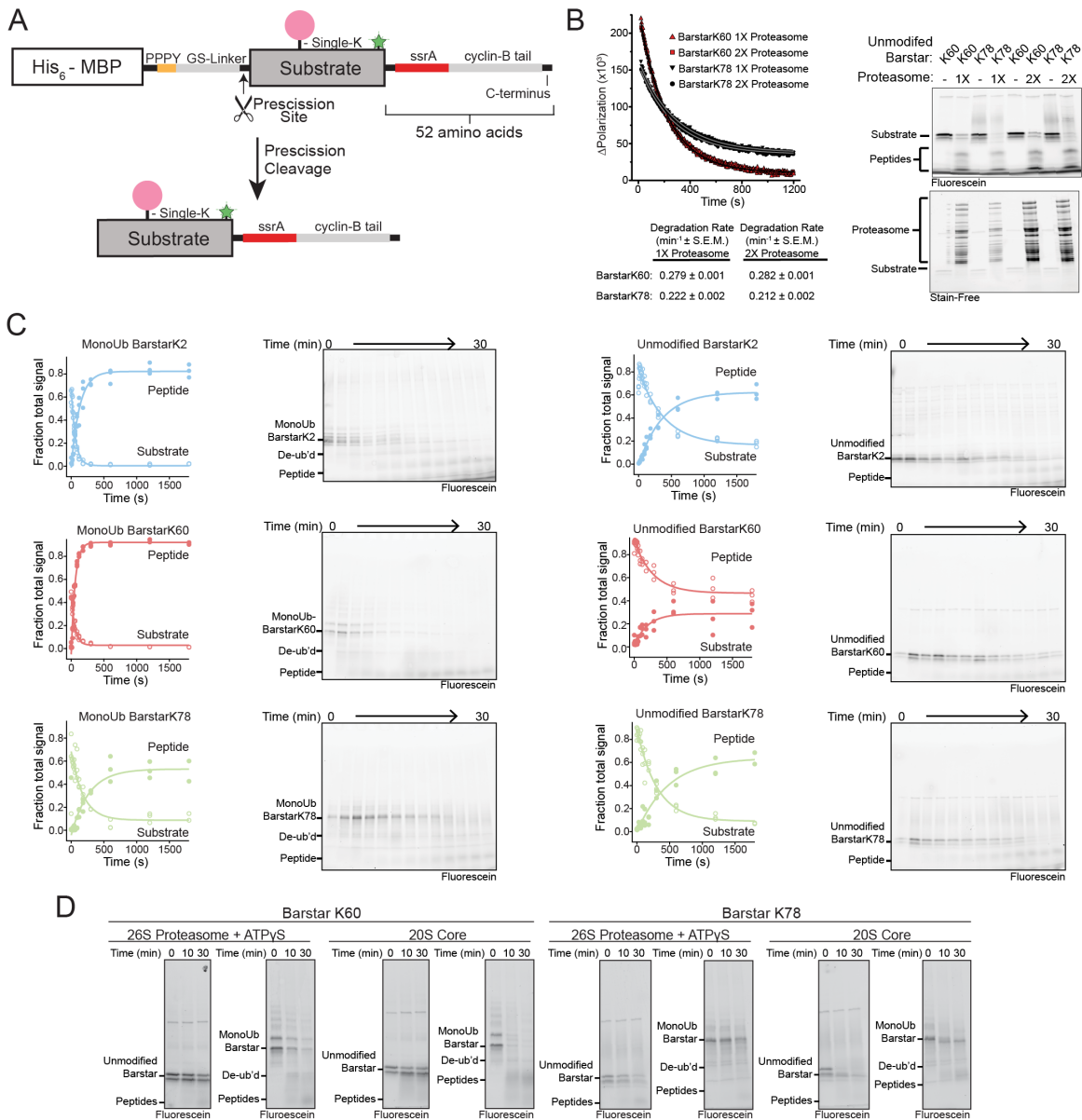
Figure s3.7. Ubiquitin-independent substrate delivery allows comparison of unmodified and mono-ubiquitinated barstar variants. (**a**) Schematic showing substrate design for ubiquitin-independent delivery. An *in vitro* ubiquitination system as in Fig. 1a is used for enzymatic ligation of methylated ubiquitin to a single lysine on barstar, which contained a C-terminal unstructured region with an ssrA tag, zero-lysine cyclin-B tail, and C-terminal zero-lysine Strep(II) tag for selection. Scaffolding was removed by Prescission (HRV3C) protease and a subtractive Ni²⁺-NTA affinity step. (**b**) Confirmation of single-turnover degradation conditions through doubling of proteasome concentration. BarstarK60 and barstarK78 degradation by proteasome at the indicated concentrations were monitored by fluorescence polarization (n=2). Observed rates are reported with S.E.M. Right, end-point SDS-PAGE gel of degradation showing conversion of barstarK60 and barstarK78 to peptides (fluorescein channel) and total protein (Stain-Free imaging, Bio-Rad). (**c**) Representative SDS-PAGE gels of ubiquitin-independent degradations with identified bands indicated at left for each variant. Quantifications and fits of substrate bands are shown left of the representative gels. "Substrate" and "Peptide" bands as a fraction of total lane intensity are presented as averages with standard deviations (n=3). (**d**) Fluorescence scans of SDS-PAGE gels from time courses of unmodified or monoUb-barstarK60 and barstarK78 degradations with proteasome in the presence of ATPγS (n=1) or with isolated core particle (n=2). Core particle replicate is presented in Supplementary Fig. 8. Identified bands are indicated.
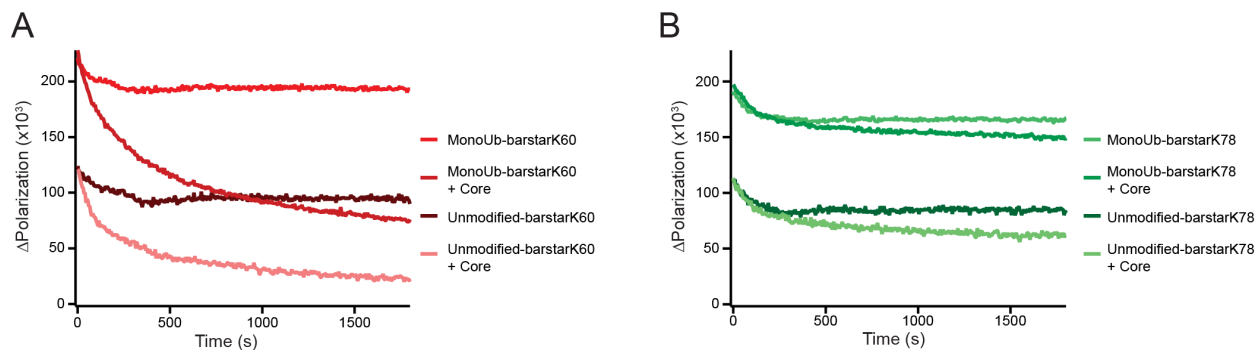
Figure s3.8. Proteolysis kinetics for ssrA-tagged barstar substrates by the 20S core particle.
Fluorescence polarization measurements of (**a**) ssrA-tagged, tailed barstarK60 or (**b**) ssrA-tagged, tailed barstarK78 with or without monoUb modification (300nM) in the presence of excess core particle (2.5 μM) displays slow, non-exponential kinetics and lower extent of proteolysis. All experiments were repeated twice with similar results, see Supplementary Fig. 7.

Figure s3.9. Altered energetics of ubiquitinated substrates mediates proteasomal engagement and degradation. (**a**) Fluorescein scans of 12% Bis-Tris Nu-PAGE (Invitrogen) SDS-PAGE gels of thermolysin proteo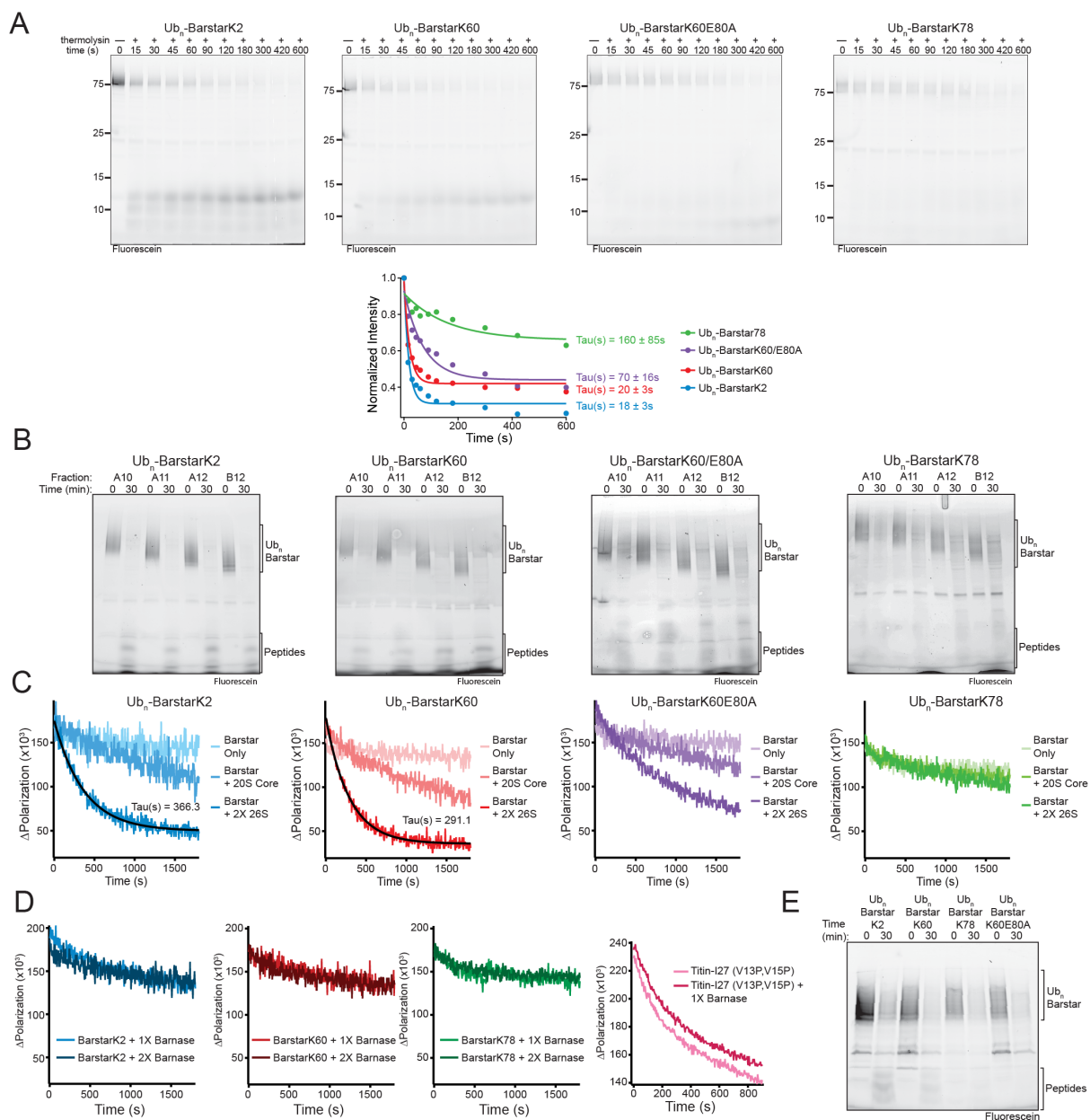lysis of Ub$_n$-barstar variants, with molecular weight standards and time points indicated (Top; n=1). Quantified gel bands were normalized and plotted against time, and time constants were calculated by fitting to Equation 3 with error representing S.E.M. for the fit. (**b**) Fluorescein scan of 4-20% TGX (Bio-Rad) SDS-PAGE gels showing the end-point samples from single-turnover degradations of fractions obtained from size exclusion chromatography of Ub$_n$-barstar variants, with poly-ubiquitinated species and peptides indicated. Fraction A12 from each gel is presented in Fig. 4 (n=1). (**c**) Fluorescence polarization of Ub$_n$-barstar substrates treated with 2X concentration of proteasome (n=1), 900 nM isolated core particle (n=1; see **e**), or untreated (n=1). Reported time constants were derived from fitting to Equation 3. (**d**) Changes in fluorescence polarization during single-turnover degradations of Ub$_n$-barstars in the presence of 20 μM (1X) or 40 μM (2X) barnase (Left). Single-turnover degradation of FAM-Titin-I27[V13PV15P] in the presence or absence of 20 μM (1X) barnase, monitored by fluorescence polarization (Right). (**e**) Fluorescence scan of 4-20% TGX (Bio-Rad) SDS-PAGE gels with end-point samples for the incubation of Ub$_n$-barstar variants (5-10 nM) with excess isolated core particle (900 nM). Peptides and Ub$_n$-barstar species are indicated. Experiments in **e** were repeated twice (see **c**).
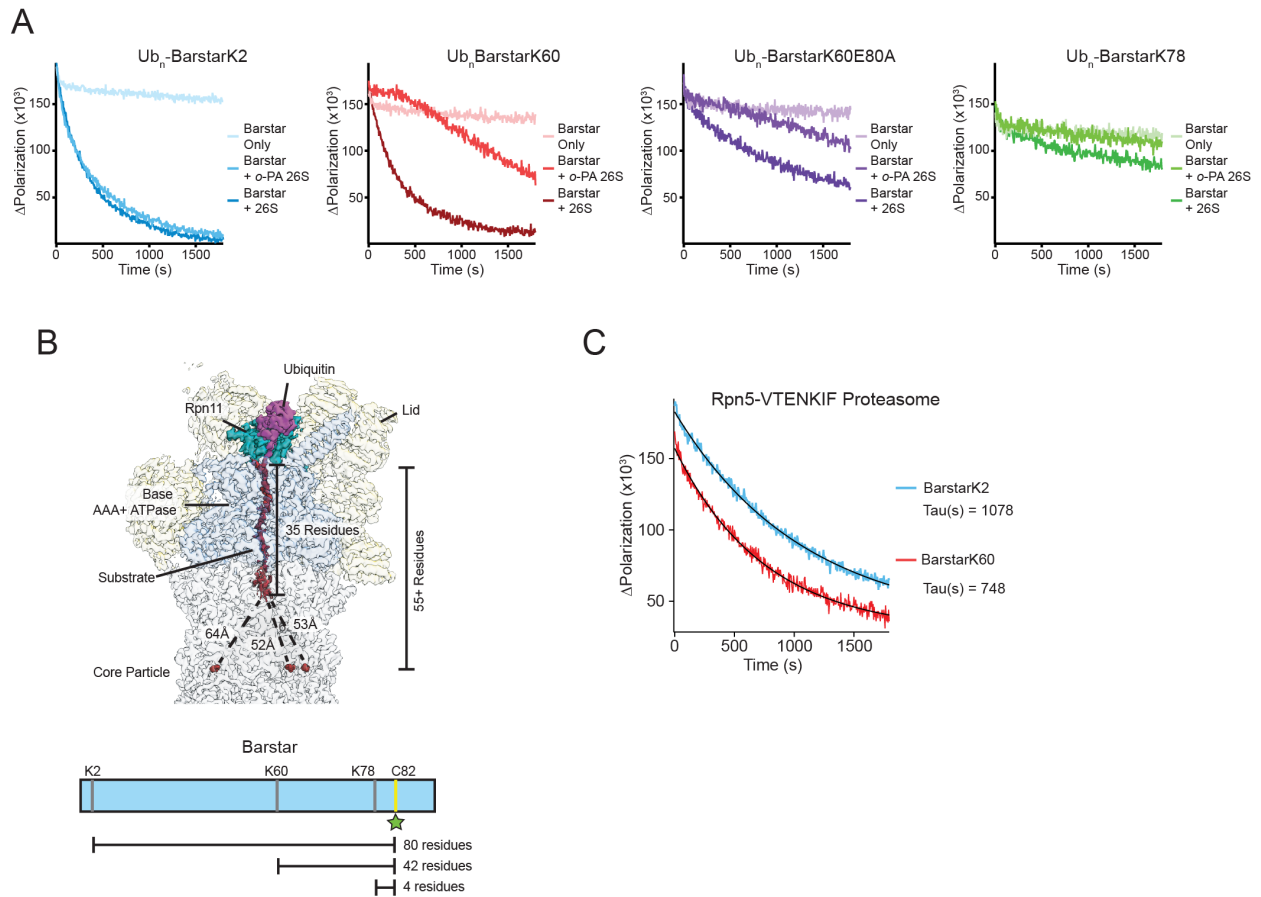
Figure s3.10. Proteasome engagement can be the rate limiting step for degradation. (**a**) Single-turnover degradations of Ub_n-barstar substrates in the presence (n=1) and absence (n=6) of an Rpn11 inhibitor o-phenanthroline monitored by fluorescence polarization. (**b**) Density for substrate-bound proteasome (EMD: 9045, PDB: 6FVW) with the lid subunits as well as Rpn1 and Rpn2 in yellow, ubiquitin in magenta, Rpn11 in dark cyan, the base AAA+ ATPase in cornflower blue, substrate polypeptide in red, and the core particle in light grey. Distances were obtained from PDB: 6FVW. Below, cartoon of barstar sequence highlighting singe lysine positions and the single, fluorescein-labeled cysteine at position 82. (**c**) Single-turnover degradations of Ub_n-barstarK2 and Ub_n-barstarK60 by Rpn5-VTENKIF proteasome and time constants calculated from fitting to Equation 3 (n=1).

Chapter 4: Toward developing a smFRET assay to track the molecular trajectory of protein unfolding by the proteasome

This work was done in collaboration with Dr. Erik Jonsson and Dr. Zaw Htet in the Martin Lab with helpful discussions and data analysis by Emma Carroll of UC Berkeley.

Introduction

Paramount to successful degradation of a protein by the proteasome is the mechanical unfolding of any encountered domains. Similar to many other AAA+ unfoldases, the proteasome transduces the chemical energy from ATP hydrolysis into conformational changes of AAA+ domains that use pore conserved loops to interact with substrate polypeptides in the central processing channel. ATP-hydrolysis-coupled vertical movement of these domains thus leads to a translocation of the substrate and application of an unfolding force when a folded domain hits the narrow entrance to the central pore. For model substrates with a single, well-folded domain and a long unstructured tail for engagement, the mechanical unfolding step poses the rate-limiting barrier to degradation (Bard et al., 2019; Carroll et al., 2020; Greene et al., 2019).

However, not all engaged substrates are destined for complete degradation. A prominent example is the transcription factor NFκB, which is only partially degraded by the proteasome, similar to other transcription factors (Fan and Maniatis, 1991; Holmberg et al., 2004; Karin and Ben-Neriah, 2000; Orian et al., 1999; Palombella et al., 1994; Piwko and Jentsch, 2006; Schrader et al., 2011; Tian et al., 2005). The model for this partial processing is that an internal degradation-stop signal, a region with low sequence complexity, reduces the grip of pore loops on the substrate polypeptide and prevents unfolding of a subsequent domain with high thermodynamic stability (Tian et al., 2005). A substrate's sequence complexity (Tomita and Matouschek, 2019), thermodynamic stability, and folding topology have been suggested to affect the ability of AAA+ unfoldases to successfully process the substrate (Lee et al., 2017; Martín et al., 2017; Sivertsson et al., 2019; Sriramoju et al., 2018, 2020). Additionally, there is a potential that different AAA+ unfoldases have variant capacity to degrade certain domains (Kardon et al., 2020; Koodithangal et al., 2009; Kraut et al., 2012) thus making comparisons between motors difficult. While substrate unfolding has been investigated in detail for bacterial AAA+ unfoldases, much less is known about proteasomal substrate unfolding. For instance, systematic analyses of multiple protein folds with diverse thermodynamic properties have so far not been conducted with the proteasome.

There are similar polypeptide translocation kinetics for ribosomal elongation and proteasomal translocation (Lu et al., 2015; Moran et al., 2010), and these rates are generally much slower than the folding/unfolding rates of many single domain proteins (Broom et al., 2015; Galzitskaya et al., 2003; Garbuzynskiy et al., 2013; Glyakina and Galzitskaya, 2020). For translation, elongation rate tuning through conserved rare synonymous codon placement has been found to induce population of productive intermediary structures that aid in protein folding (Bitran et al., 2020; Buhr et al., 2016; Chaney et al., 2017; Jacobs and Shakhnovich, 2017; Komar, 2019; Liutkute et al., 2020; Rodnina,

2016; Sharma and O'Brien, 2018; Stein and Frydman, 2019; Walsh et al., 2020; Waudby et al., 2019). Could this shared kinetic disparity between fold/unfolding rates and polypeptide translocation mean that intermediary structures of proteins should be expected for proteasomal degradation of various substrates? Indeed, previous single-molecule studies of the ClpXP protease using an optical trapping approach have shown evidence of partial unfolding and release of substrates during processing (Olivares et al., 2018). Moreover, NMR investigation of calmodulin processing by the protein unfoldase VAT (p97) uncovered a partial refolding of the substrate after release from the motor (Augustyniak and Kay, 2018). Additionally, these studies have implicated the local topology and local stability of substrate proteins at the site of initial constriction by the AAA+ pore as being important, but how generalizable is this finding to the proteasomal degradation of a subset of protein folds known to be encountered by the proteasome in vivo? In this chapter, I outline a FRET-based experimental means to assess in bulk and at the single-molecule level how the thermodynamic stability and topology of a substrate influence the proteasomal degradation process.

Results

Generalizable dual labeling of substrate for FRET-based degradation studies

In order to systematically investigate the molecular trajectory of proteasomal unfolding for various substrates, a FRET based method to monitor the folded state of protein domains was employed. In most single-domain proteins, the N- and C-terminus are proximal to each other in the folded state (Carugo, 2016; Christopher and Baldwin, 1996; Krishna and Englander, 2005). A FRET pair integrated at or near the N- and C-termini would thus produce a high-FRET signal in the folded state and low-FRET in the unfolded state. Given the vectoral nature of substrate unfolding by the proteasome, the end-to-end length of the substrate polypeptide would be extended upon unfolding and be maximal during translocation through the central channel, causing little-to-no FRET (Figure 4.1A)(Baytshtok et al., 2015; Kolygo et al., 2009) and thus allowing for the molecular trajectory of substrate unfolding to be monitored.

In order to double label a substrate, first a solubility-enhancing MBP moiety that also aids in affinity purification was fused to the N-terminus of the substrate of interest, separated by a flexible linker containing a Tobacco Etch Virus (TEV) protease cleavage. Substrate domains were engineered to contain a single cysteine residue at or near the C-terminus for labeling with maleimide-containing fluorescent dyes. The substrate's C-terminus is fused the ssrA recognition sequence and an unstructured segment of cyclin-B, known for robust engagement by the proteasome (Bard et al., 2019; Carroll et al., 2020; Greene et al. 2019). Upon TEV cleavage, an N-terminal GGG is exposed that serves as the substrate for transamidation by an engineered sortase (srtA), linking it with a fluorescently labeled LPETGG peptide (Genscript) (Theile et al., 2013). A final affinity step utilizing an additional C-terminal His_6 tag on the substrate allowed the selective purification of full-length, double labeled substrate for subsequent degradation studies.

The unfolding of protein domains within substrates harboring readily engageable unstructured initiation regions has been demonstrated to be the rate-limiting step of ubiquitin-dependent proteasome degradation (Bard et al., 2019). Additionally, this principle was extended to ubiquitin-independent degradation (Carroll et al., 2020) utilizing the SspB/ssrA interaction partners from *E.*

coli to facilitate degradation initiation by the proteasome (Bashore et al., 2015). Given the role of ubiquitin in destabilizing folded domains (Carroll et al., 2020), ubiquitin linkages impacting proteasomal activities (Bard et al., 2018; Ding et al., 2019; Dong et al., 2019), and the need for deubiquitination during degradation, the ubiquitin-independent system was employed to study the proteasomal processing in the absence of ubiquitin's multiple, potentially conflating, roles during the degradation process.

As a proof of principle, I first tested a substrate based on barstar from *Bacillus amyloliquefaciens*, the intracellular inhibitor to barnase. In vitro ubiquitin-independent proteasome degradation of barstar is known to be rate-limited by unfolding (Carroll et al., 2020). Although barstar has a length and thermodynamic stability similar to the titin I27 domain, another frequently studied in vitro substrate of the proteasome, its degradation rate (tau ~ 220 s; Carroll et al., 2020) differs significantly from that of I27 (tau ~ 45s; Bard et al., 2019; Greene et al., 2019), implicating differences in unfolding ability by the proteasome. Barstar has been described to unfold and refold via intermediates (Khurana et al., 1995; Nölting et al., 1997; Zaidi et al., 1997), and the proteasomal degradation of ubiquitinated barstar in the absence of an appended initiation region indicated a ubiquitin-dependent partial unfolding event (Carroll et al 2020). Given these documented partially unfolded states of barstar, it is possible that the slower proteasomal degradation rate originates from a transiently populated, fast refolding intermediate that extends the dwell time before global unfolding. It could also be possible that there exists a high local stability of the C-terminal β-sheet of barstar that stymies unfolding.
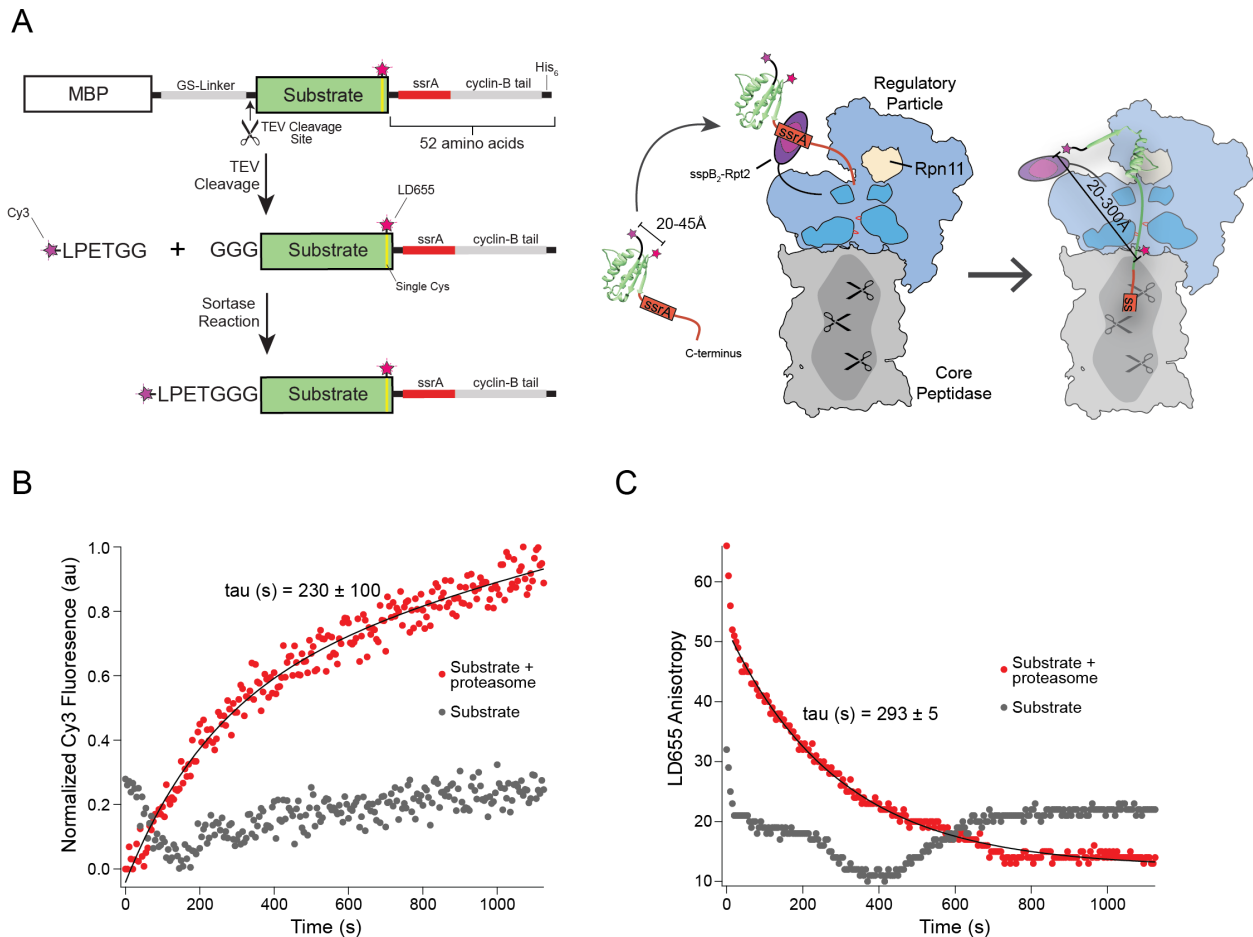
Figure 4.1. Generalizable FRET-based strategy to measure proteasome mediated unfolding and degradation. (A) Cartoon depiction of the substrate preparation for dual labeling and proteasome processing. Left: Full-length substrate labeled on its single cysteine with a maleimide LD655 could be removed from its MBP scaffold via TEV cleavage, allowing for exposure of an N-terminal GGG to be used as a substrate in subsequent sortase labeling with a Cy3 conjugated LPETGG peptide. Right: Cartoon depiction of the ubiquitin-independent proteasome delivery system with theoretical length estimates for FRET dye pairs as a function of unfolding and translocation through the proteasome. (B) Single-turnover, ubiquitin-independent degradation of barstar monitored by the increase in donor fluorescence. Tau was derived by fitting the fluorescence trace to a double-exponential model and reported as the dominant fast phase. (n=1) (C) Single-turnover, ubiquitin-independent degradation of barstar monitored by the decrease in acceptor-dye anisotropy. Tau was derived by fitting to a single-exponential model. (n=1)

Barstar was prepared as described in Figure 4.1A with Cy3 covalently attached to the N-terminus and LD655 (Lumidyne) conjugated to the single cysteine within barstar at position 82. To assess if the incorporation of this FRET pair impacted proteasome degradation rate, dual labeled barstar substrate was degraded in a ubiquitin-independent manner under single-turnover conditions, while monitoring changes in donor fluorescence (Figure 4.1B). The tau for degradation was 230 s is in good agreement with previous measurements of unlabeled barstar (Carroll et al., 2020). To further confirm this result, the degradation was repeated while monitoring the decrease in LD655 anisotropy upon substrate cleavage into small peptides (Figure 4.1C), which revealed a comparable time constant. This agreement for different probes is expected, as substrate unfolding monitored by loss of FRET is the rate limiting step of degradation for this substrate (Carroll et al., 2020) and should therefore show the same kinetics as the proteolysis monitored by the change in anisotropy. It thus confirms that the FRET pair can reliably report on barstar unfolding and degradation by the proteasome.

Single-molecule FRET measurement of substrate processing

The FRET probe described has limited use in bulk experiments tracking proteasome processing of substrates with unstructured initiation regions, as unfolding is rate-limiting and therefore the same as the degradation rate. However, single-molecule approaches offer a much higher level of detail into this dynamic process. Reconstituted, biotinylated, and SspB-containing proteasome was immobilized on a glass coverslip that was functionalized with biotin and pretreated with neutravidin (Figure 4.2A; Materials and Methods). Under Total Internal Reflection (TIRF) illumination, dual labeled substrate can be visualized when binding to the proteasomes on the coverslip surface. Measurements of both the donor and acceptor channels were acquired for 200 s (approximately 1 tau for degradation) at 100 ms increments to generate movies of degradation reactions.

Upon initial binding, substrate was found predominantly in a high-FRET state with a FRET efficiency (E_{app}) of 0.8 (Figure 4.2B). Assuming an R_0 of 60 Å, this FRET efficiency would equate a dye distance of ~40 Å, which in good agreement with the expected geometry of the double-labeled substrate, considering a ~12 Å distance between Lys1-Cα and Cys82-Cα in the native barstar structure is (PDB: 1BTA), the ~20 Å contributed by the elongated LPETGGG linker sequence (assuming 2.5 Å per residue), and the additional spacers the dye molecules themselves (approximately 8 Å each). The FRET distribution shows a small shoulder at higher efficiencies that could originate from the flexibilities of the LPETGG linker and dye spacers, bringing the fluorophores into closer proximity.
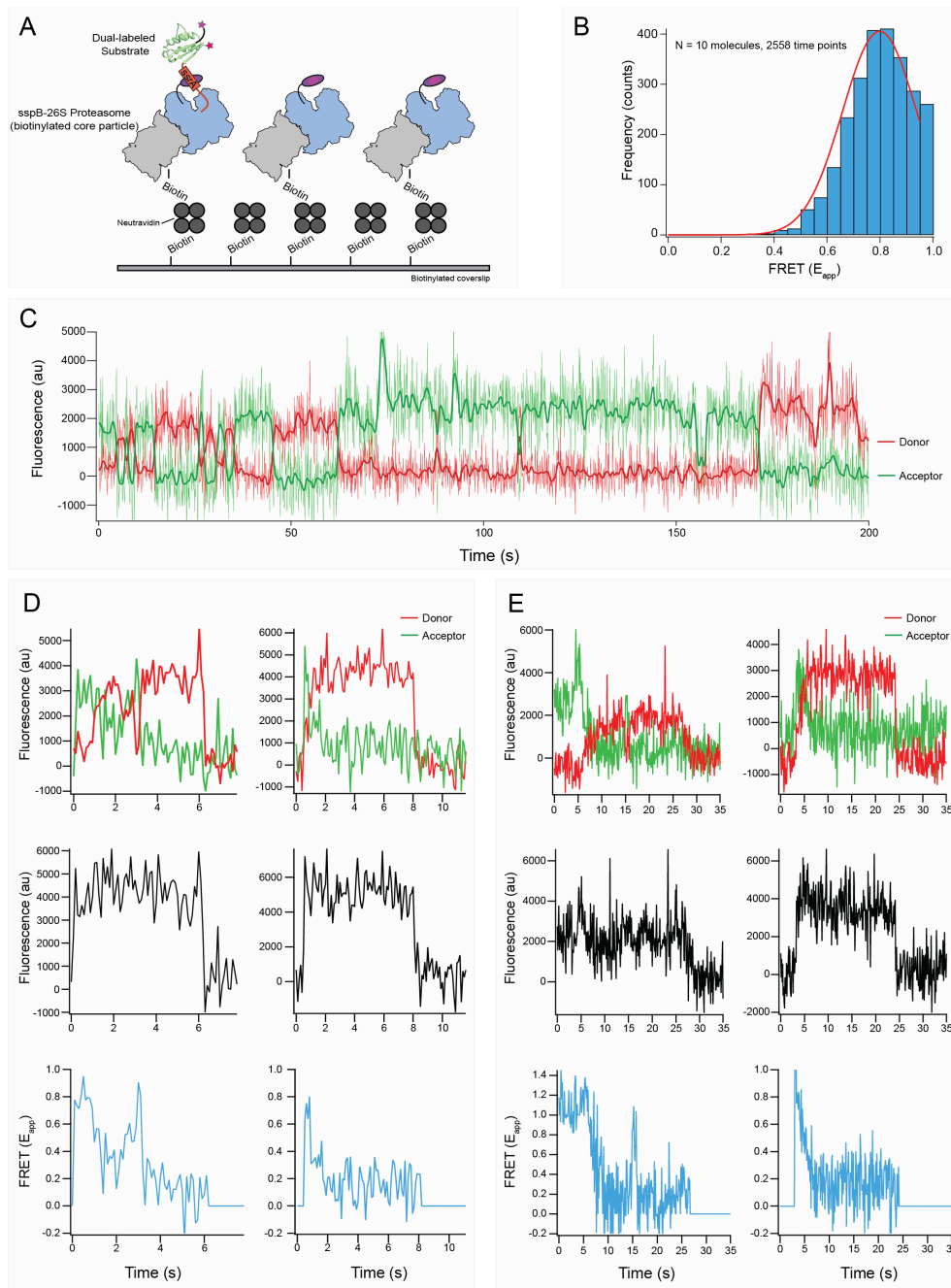
Figure 4.2. Proof-of-principle experiments for monitoring proteasomal substrate unfolding by single-molecule FRET. (A) Cartoon depiction of the smFRET slide setup. (B) FRET efficiency of the barstar substrate upon initial binding to the proteasome or surface. Ten molecules were observed for a total of 2556 time points and plotted as a histogram of distributions with a fit to a single Gaussian model. (C) Time traces for donor (red) and acceptor (green) fluorescent channels of a single substrate. Raw data were acquired every 100 ms and shown in a thin line. Smoothed data taken from every 25 measurements is displayed in a dark line. (D) Single-molecule measurements of barstar processing events show evidence of an intermediate-FRET state. Top: time traces for donor (red) and acceptor (green) fluorescent channels. Middle: total fluorescence of both donor and acceptor channels. Bottom: FRET efficiency (E_{app}) plotted against time. The left and right set of graphs represent two different proteasomes and barstar-processing events. (E) Same as D, except providing evidence for a continuous high-to-low FRET transition.

Use of the LD655 dye with longer life time (Altman et al., 2012) was necessary to avoid photobleaching during the 200 s acquisition, which is outside of the time regime typically afforded

by other dyes, like Cy5 (Roy et al., 2008). This lifetime is best illustrated in Figure 4.2C, depicting both the donor and acceptor fluorescent signal over the full 200 s acquisition, where the substrate molecule is observed to toggle between a high-FRET and low-FRET state. Most FRET traces observed demonstrated a penultimate high-to-low-FRET state transition prior to ultimate loss of fluorescence (due either to successful hydrolysis and peptide product release or due to photobleaching) which is likely indicative that observed FRET changes are due to processing by the proteasome. Importantly, the transition between high- and low-FRET states was not observed when the slowly hydrolyzable nucleotide analog, ATPγS, was preincubated with the proteasome (data not shown). This is reasonable because inhibiting ATP hydrolysis by the 26S proteasome hinders not only protein unfolding and translocation, but also substrate insertion into the central pore and engagement by the ATPase motor.

In addition to the transitions between high-FRET and low-FRET states (Figure 4.2C), the barstar substrate displayed additional FRET-change behavior. In one case, multiple traces were observed to show transition from the high-FRET state (E = 0.8) to a short-lived (~1s), intermediate-FRET state (E ~ 0.4) prior to decaying into a low FRET-state. While limited in total number of events, these data are intriguing, and merit further studies. It is possible that the intermediate-FRET originates from the (un)folding intermediate described for barstar, and investigation of the wealth of mutants that promote or disfavor intermediary structures of barstar would likely be insightful (Nölting et al., 1997).

Most observations yielded a single step high-to-low FRET transition, which could be attributed to either global unfolding (has been observed to occur in <1ms for ClpX unfolding of substrates; Olivares et al., 2018) or acceptor dye photobleaching (data not shown), but there was another case in which substrates were observed to gradually convert from the high-FRET to the low-FRET state over the course of ~5 s (Figure 4.2E). This behavior could either be due to a gradual unraveling of the barstar native structure, or could be due to a global unfolding event followed by the donor dye residing near the side of the proteasome, such that the progression of the acceptor dye through the central channel can be observed. Assuming a translocation velocity of ~15 amino acids per second (estimated by Bard et al., 2019) and that FRET would no longer be observed after translocation of ~50 residues into the central channel (assuming ~2.5 Å per residue in end-to-end length), it is possible that this latter event could occur over a ~5s time frame.

In both scenarios described by Figure 4.2D and E, there are instances after the intermediate or slow FRET decay that involve a transient return to high-FRET state. This return to high-FRET could be indicative of a slipping/refolding event, which has been observed before for other AAA+ unfoldases (Olivares et al., 2018). Alternatively, this could be due to the dye pairs coming into close physical proximity elsewhere in the trajectory (e.g. the acceptor could reside within the translocation channel and FRET with the donor that is outside the channel). Lastly, this final high-FRET event could also be due to FRET occurring between the donor on the substrate and a Cy5 placed on the core particle for localization purposes. A series of experiments without an acceptor dye on the substrate is required to aid in ruling out this third possibility.

<u>Discussion</u>

The proteasome is responsible for the majority of protein degradation in eukaryotic cells and thus, for unfolding hundreds to thousands of substrates with different protein folds (Figure 1.1A). Increasing evidence has shown that different AAA+ ATPases process substrates with differential processivities or overall efficiencies, despite relying on similar mechanisms for unfolding and translocation (Glynn et al., 2020; Kardon et al., 2020; Koodithangal et al., 2009; Kraut et al., 2012). Given the importance of the unfolding step for determining the success and rate of degradation, it was the goal of the studies presented in this chapter to establish a smFRET approach that allows monitoring the substrate-unfolding process by the proteasome and could be readily extended towards multiple substrate domains that include physiologically relevant protein folds.

In principle, the presented methods for dual labeling through cysteine and sortase-catalyzed modifications should be applicable to any folded domain that contains a single cysteine (engineered or otherwise) near the C-terminus of the protein. Where this cysteine requirement cannot be met, the use of unnatural amino acid (UAA) incorporation and "click" chemistry can be readily employed (Chin, 2017; Davis and Chin, 2012; Young and Schultz, 2018). Additionally, this labelable cysteine or UAA could be placed within different locations of a substrate to theoretically yield subdomain structural fluctuations. Given the use of a single engageable unstructured region and careful adherence to single-turnover degradation conditions in bulk measurements, comparisons between substrate degradation rates will be robust and directly correlated to the unfolding ability of the substrate by the proteasome. Additionally, there exists a wealth of literature examining the thermodynamics and kinetics of protein folding for numerous physiologically relevant proteins and protein folds, allowing more systematic analyses of degradation rates and correlation with biophysical constants.

The ability to acquire at least 200 s of smFRET data in a single movie opens up this technique to investigating substrates that are of similar and/or lower thermodynamic stability than barstar, which is processed by the proteasome with a time constant of ~ 220 s. Indeed, most eukaryotic proteins are thought to have a lower $\Delta G_{folding}$ than barstar (Walker et al., 2019). Deciphering the different interpretations of the smFRET data collected thus far will require additional experimentation (varying dye placement, sufficient repetitions for proper statistics). However, as a proof of principle, the prospects of smFRET to study protein unfolding by AAA+ unfoldases, including the proteasome, is encouraging.

Methods

Preparation of double labeled barstar

E. coli BL21 Rosetta 2 (DE3) cells were transformed with plasmid containing the substrate protein. Cells were then grown in 2 L minimal M9 media to $0.4 < OD_{600} < 0.8$ and induced with 1 mM IPTG for 3 hours at 37°C. Bacteria were pelleted and resuspended in lysis buffer (60 mM HEPES pH 7.6, 150 mM NaCl, 1 mM EDTA, and 5% glycerol and supplemented with protease inhibitors (aprotonin, pepstatinA, leupeptin, and PMSF or AEBSF), benzonase (Novagen), and 2 mg/mL lysozyme) and stored at -80°C. Resuspended cells were lysed by sonication and the lysate was clarified by centrifugation at 20,000 rcf, 4°C, 30 minutes. Barstar was first purified via affinity chromatography utilizing its N-terminal MBP and amylose resin (NEB). Lysate was flowed over the amylose resin 5 times, washed with 50 mL of lysis buffer. Barstar was eluted 15-20mLwith 60 mM HEPES pH 7.6, 150 mM NaCl, 0.5 mM EDTA, 5% glycerol, and 10 mM maltose. Eluate was further purified by Ni^{2+}-NTA affinity chromatography using a 5mL HisTrap HP (GE) column, washed with 60 mM HEPES pH 7.6, 150 mM NaCl, 20 mM imidazole, and 5% glycerol before being eluted in 60 mM HEPES pH 7.0, 150 mM NaCl, 250 mM imidazole, and 5% glycerol. Eluate was spiked with EDTA to a final concentration of 2 mM before reacting with 5 molar equivalents of LD-655 maleimide (Lumidyne) for 2 hours at RT or overnight at 4°C. Maleimide labeling reaction was quenched with 2:1 DTT to dye for 15 minutes at RT before loading onto a S200i 10/300 size exclusion column (GE) pre-equilibrated with 60 mM HEPES pH 7.6, 50mM NaCl, 50 mM KCl, 10 mM $MgCl_2$, 0.5 mM EDTA, 0.5 mM TCEP and 5% glycerol. Peak corresponding to full length protein was pooled, concentrated, and quantified by UV/vis absorption at 280nm and 646nm before being flash frozen and stored at -80°C for future use. Barstar was thawed at room temperature and cleaved with a molar excess of TEV protease for 30 minutes at room temperature. Immediately afterwards, tagless srtA (5 µM final), $CaCl_2$ (5 mM final), and Cy3-LPETGG peptide (Genscript; 100 µM final) were added and allowed to react for 30 minutes at room temperature. Barstar was purified from TEV, Cy3-LPETGG, and srtA through affinity chromatography on a His SpinTrap™ (GE) following manufacturer guidelines and eluted with 60 mM HEPES pH 7.6, 50mM NaCl, 50 mM KCl, 10 mM $MgCl_2$, 250 mM imidazole, 0.5 mM TCEP and 5% glycerol. Eluate was buffer exchanged into 60 mM HEPES pH 7.6, 50mM NaCl, 50 mM KCl, 10 mM $MgCl_2$, 0.5 mM EDTA, 0.5 mM TCEP and 5% glycerol in a Zeba™ Spin Desalting Column, 7 MWCO, 0.5 mL (ThermoFisher). Barstar was quantified by UV/vis absorption at 280nm, 555nm, and 646nm before being flash frozen and stored at -80°C.

Preparation of sspB base subcomplex, lid subcomplex, 20S core particle, and Rpn10

Preparation of these proteins were conducted exactly as described in Chapter 3.

Preparation of biotinylated, cy5 labeled core particle

An avi-tag was engineered into the Pre1 subunit containing a 3X-FLAG tag through homologous recombination. Core particle was purified as described in Chapters 2 and 3 except that the FLAG

column was eluted in 50 mM HEPES pH 8.2, 150 mM NaCl, 0.15 mg/mL 3X FLAG peptide (Genscript). The core particle was Cy5 labeled by incubation with 0.98 molar equivalents of NHS-Cy5 (Sigma) at room temperature for 1 hour before quenching with addition of TrisHCl pH 8.0 to 10 mM. Labeling efficiency of 42% was achieved. Core particle was bufferexchanged into biotinylation buffer (10 mM TrisHCl pH 8.0, 25 mM NaCl, 10 mM $MgCl_2$) using a 5mL HiTrap™ desalting column according to manufacturer protocols. Core particle was concentrated to 8 µM (6 µM final) and reacted with biotin (100 µM final), BirA (40 µM final), and ATP (10 mM final) overnight at 4°C. Reaction was loaded onto a Sup6i 10/300 size exclusion column (GE) pre-equilibrated with 60 mM HEPES pH 7.6, 50mM NaCl, 50 mM KCl, 10 mM $MgCl_2$, 0.5 mM TCEP and 5% glycerol. Peak corresponding to core particle was pooled, concentrated, and quantified by UV/vis absorption at 280nm and 646nm before being flash frozen and stored at -80°C for future use.

Single-turnover, ubiquitin independent degradation reactions

2X stocks of substrate (300 nM final) were prepared in assay buffer (60 mM HEPES pH 7.6, 50 mM NaCl, 50 mM KCl, 10 mM MgCl2, 0.5 mM TCEP, 5 mM ATP, 5% glycerol, 1 mg/ml BSA). 2X proteasome stocks were performed by reconstituting recombinant lid (5 µM final), recombinant $SspB_2$-Rpt2 base (5 µM final), recombinant Rpn10 (5 µM final), and core particle (2.5 µM final) in assay buffer with an ATP-regeneration system (creatine kinase, creatine phosphate, and 5 mM ATP) and allowed to assemble for 3 minutes at room temperature. Reactions were initiated with equivolume (2.5 µL) addition of substrate to proteasome directly within a 384-well black bottom plate (Corning) and fluorescence polarization or Cy5 fluorescence was monitored in a Synergy Neo2 multimode plate reader (BioTek). Decreased fluorescence polarization over time as substrate was processed into peptides could also be fit to a single exponential model in IgorPro7. Increased fluorescence intensity over time as substrate lost FRET during processing could be fit to a double exponential model in IgorPro7.

smFRET measurements and analysis

Measurements were acquired on a custom-built microscope equipped with Nikon TiE microscope body, Nikon 60X 1.49 NA objective-type TIRF objective, 532 nm and 633 nm laser lines, and Ixon+ electron multiplied charge coupled device (EM-CCD) camera (Andor). Prefunctionalized (biotinylated) coverslips were acquired from Microsurfaces Inc. Slides were incubated with 0.01 mg/mL neutravidin in assay buffer (60 mM HEPES pH 7.6, 50 mM NaCl, 50 mM KCl, 10 mM MgCl2, 0.5mM TCEP, 1mM ATP, 0.4X ATP regeneration system, and 5% glycerol) for 3 minutes at room temperature. sspB containing reconstituted proteasome (200 nM cy5 labeled and biotinylated core particle, 400 nM sspB base, 750 nM Rpn10, 600 nM lid, 1X ATP regeneration, 0.5 mg/mL BSA) was assembled in assay buffer for 3 minutes at room temperature before a 1:500 dilution in assay buffer to a suitable concentration for being flowed onto the slide. Proteasome was incubated on the slide for 3 minutes at room temperature before being wash with acquisition buffer (60 mM HEPES pH 7.6, 50 mM NaCl, 50 mM KCl, 10 mM MgCl2, 0.5mM TCEP, 1mM ATP (or ATPyS where applicable), 5% glycerol, 1-2 mM Trolox, 0.5 mg/mL BSA, and an oxygen scavenging system (protocatechuic acid (PCA)/protocatechuate-3,4-dioxygenase (PCD)). Substrate was diluted to 100-200 nM in acquisition buffer before being applied to slide. Data was acquired immediately after substrate was added. A single 100 ms image of the slide was obtained after excitation with the 633 nm laser in order to map the position of cy5 labeled core particle on the slide. Subsequently, the

slide was illuminated with the 533 nm laser and images were acquired after 100 ms of integration for 200 s in total (2000 images per movie).

Data were analyzed in FIJI and using custom MATLAB scripts. First images were boundary corrected for consistency. Core particle position was mapped in FIJI using the first image acquired. Then maximum acceptor intensity across each movie was calculated in FIJI to spatially map the positions of each FRET event. These events were compared to each other and events outside of a 95% confidence interval discarded. At each positively correlated FRET position, the donor intensity, acceptor intensity, total intensity, and apparent FRET efficiency was calculated. Traces were manually curated for events marked by the appearance of a substrate in a predicted high FRET state and initial low FRET states discarded.

Chapter 5. Concluding remarks

The work presented herein describes multiple modes of regulating proteasomal degradation. All evidence provided was attained through biochemical *in vitro* reconstitution and structural studies, but has likely important, physiologically relevant, implications.

In Chapter 2, I describe how the proteasome is found in an equilibrium between the s1 conformation and the s2 conformation, and address the question of whether, and if so how, this equilibrium could play a role in the degradation process. Based on a series of biochemical and structural data, I found that the conformational switching dynamics play an important role in the ability of the proteasome to engage a substrate protein. The s1 conformation is thereby not only required to allow substrate access to the central pore, it must also be populated long enough for substrate-tail insertion and engagement to occur. Substrate engagement with the pore loops then actively drives the conformational switch to non-s1 states, which commits the substrate to degradation. While multiple studies have described subtle shifts in the conformational landscape of the proteasome in response to different perturbances (Ding et al., 2017, 2019; Dong et al., 2019; Eisele et al., 2018; Greene et al., 2019; Haselbach et al., 2017; De la Peña et al., 2018; Matyskiela et al., 2013; Śledź et al., 2013; Unverdorben et al., 2014; Wehmer et al., 2017; Zhu et al., 2018), my Rpn5-VTENKIF mutant proteasome data provided the first evidence for the critical importance of conformational interconversions in controlling substrate degradation. Thus, minor shifts in the conformational population seen in other studies could present large biochemical and functional consequences dependent on these dynamics. It remains to be confirmed whether conformational dynamics can exert significant control over the degradative process, which will require experimental methods of higher molecular and temporal resolution than allowed by bulk biochemistry and cryo-EM. Additionally, though numerous factors have been proposed to shift the conformational equilibria of the proteasome away from the s1 state, it has yet to be reconciled that, *in situ*, the proteasome is found more predominantly in the s1 conformation than cryo-EM studies of purified proteasome (Asano et al., 2015; Bard et al., 2018; Greene et al., 2020), despite the likely presence of multiple substrates in the cell and even under conditions of proteotoxic stress that would substantially increase proteasomal substrate load (Guo et al., 2019) both of which that would favor non-s1 conformations. The cellular factors that bridge this divide and could be promoting the s1 conformation are as yet unknown.

In Chapter 3, I describe how ubiquitin is much more than a passive tag that allows for localization of substrate to the proteasome. Instead describing the importance of site-specificity of ubiquitination in affecting substrate thermodynamic stability, degradation rate, and commitment for degradation. We provided the first evidence that, depending on the site of ubiquitination and the resulting destabilization of the substrate fold, are sufficient to allow for population of a partially unfolding-state that is competent for proteasomal engagement. These data do not rule out that partial or complete unfolding by other cellular protein translocases, like Cdc48/p97/VAT, that also play a role

in facilitating the proteasomal degradation of substrates lacking unstructured initiation regions, but demonstrate that ubiquitination alone can be sufficient. That ubiquitination alone can be sufficient to allow degradation of well-folded proteins could help explain why directed ubiquitination of whole kinase families, characterized by an intrinsic lack of unstructured initiation regions, only allows for degradation of a particular subset (Ball et al., 2016). In addition, these data provide support for the hypothesis that lysine residues that are targets for ubiquitination could be under selective pressure to either have destabilizing effects when modified with degradative ubiquitin chains or non-destabilizing when utilized for ubiquitin-mediated regulation and trafficking. In addition to proteasome substrate selection, the energetic consequences of ubiquitin could explain the various allosteric effects observed upon ubiquitination of regulatory proteins. Elucidating the molecular mechanism(s) governing how ubiquitin is capable of these functions will be crucial to future studies. Additionally, identifying and characterizing different ubiquitination sites, using the experimental approach described, will provide insight into the extent to which ubiquitin-dependent energetic changes to substrates pervade biology.

Each proteasome within our cells is capable of degrading hundreds of proteins every day that harbor many unique energy landscapes. Though currently limited in scope, the experimental approach outlined in Chapter 4 was designed to be applicable to many different substrates and may aid in elucidating how the proteasome dismantles substrates with varied stability and unfolding pathways. Comparative studies on the proteasome and other, for instance bacterial AAA+ motors could investigate whether certain phenomena of ATP-dependent unfolding or partial degradation are conserved across domains of life.

The "resolution revolution" in cryo-EM over the past decade had a profound impact on the proteasome field, for instance through the characterization of substrate-proteasome interactions in atomic detail to provide important mechanistic insight (Dong et al., 2019; De la Peña et al., 2018) and through the quantitative analysis of conformational populations, allowing the description of conformational landscapes for the proteasome (Ding et al., 2019; Eisele et al., 2018; Unverdorben et al., 2014; Wehmer et al., 2017). In Chapter 2, I described how these high-resolution models could then be applied to low resolution negative-stain EM data in order to classify and quantitate conformational states (Figure 2.2). In Chapter 3, I described how a high-resolution structure of substrate-bound proteasome could aid in interpretation of degradation kinetics (Figure s3.10). However, the full potential of cryo-EM in illuminating the secrets of the proteasome has yet to be harvested. To date, all cryo-EM studies of the proteasome have been conducted under non-physiological pre-vitrification conditions (temperatures of 18°C or lower). Structural studies of proteins while considering physiologically-relevant temperatures has revealed further intimate details about the structure and function and can provide a potential increase in structural resolution (Chen et al., 2019). Given that several conformational states for the potentially sequential ATP-hydrolysis cycle of the heterohexameric base were lacking in all structural studies so far, it is possible that this simple experimental shift to higher temperatures could increase conformational heterogeneity of the sample and allow representation of these less-populated, but likely, conformations.

The proteasome and, more broadly, the UPS play essential roles in maintaining life. As such, misregulation of this finely tuned system can be devastating and lead to disease pathology. While the studies described herein do not speak towards any particular disease, the principles uncovered can directly inform and contribute to the study of the proteasome in disease. For instance, known ubiquitinated lysines of the critical regulatory protein Ras, are found mutated in cancers (K147N; Baker et al., 2013a, 2013b; Tate et al., 2019) and these substitutions could be under selective pressure

if this ubiquitination begets allosteric/energetic effects with functional consequences. Additionally, hundreds of amino-acid substitutions in the human population have been annotated within the proteasome (Karczewski et al., 2020) as well as many identified in cancer studies (Tate et al., 2018). Of these identified substitutions, some occur in regions known to be critical to proteasome function, such as within the nucleotide binding pocket of Rpt4 (K180T & A341G; Tate et al., 2018). Understanding the mechanisms of the proteasome in greater detail can allow for more accurate prediction of these mutational consequences and lead us closer to understanding the molecular basis of various diseases.

References

Albert, S., Schaffer, M., Beck, F., Mosalaganti, S., Asano, S., Thomas, H.F., Plitzko, J.M., Beck, M., Baumeister, W., and Engel, B.D. (2017). Proteasomes tether to two distinct sites at the nuclear pore complex. Proc. Natl. Acad. Sci. U. S. A. *114*, 13726–13731.

Altman, R.B., Terry, D.S., Zhou, Z., Zheng, Q., Geggier, P., Kolster, R.A., Zhao, Y., Javitch, J.A., Warren, J.D., and Blanchard, S.C. (2012). Cyanine fluorophore derivatives with enhanced photostability. Nat. Methods *9*, 68–71.

Asano, S., Fukuda, Y., Beck, F., Aufderheide, A., Förster, F., Danev, R., and Baumeister, W. (2015). A molecular census of 26S proteasomes in intact neurons. Science (80-.). *347*, 439–442.

Aufderheide, A., Beck, F., Stengel, F., Hartwig, M., Schweitzer, A., Pfeifer, G., Goldberg, A.L., Sakata, E., Baumeister, W., and Förster, F. (2015). Structural characterization of the interaction of Ubp6 with the 26S proteasome. Proc. Natl. Acad. Sci. U. S. A. *112*, 8626–8631.

Augustyniak, R., and Kay, L.E. (2018). Cotranslocational processing of the protein substrate calmodulin by an AAA+ unfoldase occurs via unfolding and refolding intermediates. Proc. Natl. Acad. Sci. U. S. A. *115*, E4786–E4795.

Baker, R., Wilkerson, E.M., Sumita, K., Isom, D.G., Sasaki, A.T., Dohlman, H.G., and Campbell, S.L. (2013a). Differences in the regulation of K-Ras and H-Ras isoforms by monoubiquitination. J. Biol. Chem. *288*, 36856–36862.

Baker, R., Lewis, S.M., Sasaki, A.T., Wilkerson, E.M., Locasale, J.W., Cantley, L.C., Kuhlman, B., Dohlman, H.G., and Campbell, S.L. (2013b). Site-specific monoubiquitination activates Ras by impeding GTPase-activating protein function. Nat. Struct. Mol. Biol. *20*, 46–52.

Balchin, D., Hayer-Hartl, M., and Hartl, F.U. (2016). In vivo aspects of protein folding and quality control. Science (80-.). *353*.

Ball, K.A., Johnson, J.R., Lewinski, M.K., Guatelli, J., Verschueren, E., Krogan, N.J., and Jacobson, M.P. (2016). Non-degradative Ubiquitination of Protein Kinases. PLoS Comput. Biol. *12*, 1–44.

Bard, J.A.M., and Martin, A. (2018). Recombinant Expression, Unnatural Amino Acid Incorporation, and Site-Specific Labeling of 26S Proteasomal Subcomplexes. In Methods in Molecular Biology, pp. 219–236.

Bard, J.A.M., Goodall, E.A., Greene, E.R., Jonsson, E., Dong, K.C., and Martin, A. (2018). Structure and Function of the 26S Proteasome. Annu. Rev. Biochem. *87*, 697–724.

Bard, J.A.M., Bashore, C., Dong, K.C., and Martin, A. (2019). The 26S Proteasome Utilizes a Kinetic Gateway to Prioritize Substrate Degradation. Cell *177*, 286-298.e15.

Bashore, C., Dambacher, C.M., Goodall, E.A., Matyskiela, M.E., Lander, G.C., and Martin, A. (2015). Ubp6 deubiquitinase controls conformational dynamics and substrate degradation of the 26S proteasome. Nat. Struct. Mol. Biol. *22*, 712–719.

Batey, S., Nickson, A.A., and Clarke, J. (2008). Studying the folding of multidomain proteins. HFSP J. *2*, 365–377.

Baytshtok, V., Baker, T.A., and Sauer, R.T. (2015). Assaying the kinetics of protein denaturation catalyzed by AAA+ unfolding machines and proteases. Proc. Natl. Acad. Sci. U. S. A. *112*, 5377–5382.

Beck, F., Unverdorben, P., Bohn, S., Schweitzer, A., Pfeifer, G., Sakata, E., Nickell, S., Plitzko, J.M., Villa, E., Baumeister, W., et al. (2012). Near-atomic resolution structural model of the yeast 26S proteasome. Proc. Natl. Acad. Sci. U. S. A. *109*, 14870–14875.

Beckwith, R., Estrin, E., Worden, E.J., and Martin, A. (2013). Reconstitution of the 26S proteasome reveals functional asymmetries in its AAA+ unfoldase. Nat. Struct. Mol. Biol. *20*, 1164–1173.

Bitran, A., Jacobs, W.M., Zhai, X., and Shakhnovich, E. (2020). Cotranslational folding allows misfolding-prone proteins to circumvent deep kinetic traps. Proc. Natl. Acad. Sci. U. S. A. *117*, 1485–1495.

Bondeson, D.P., Smith, B.E., Burslem, G.M., Buhimschi, A.D., Hines, J., Jaime-Figueroa, S., Wang, J., Hamman, B.D., Ishchenko, A., and Crews, C.M. (2018). Lessons in PROTAC Design from Selective Degradation with a Promiscuous Warhead. Cell Chem. Biol. *25*.

Broom, A., Gosavi, S., and Meiering, E.M. (2015). Protein unfolding rates correlate as strongly as folding rates with native structure. Protein Sci. *24*, 580–587.

Buel, G.R., Chen, X., Chari, R., O'Neill, M.J., Ebelle, D.L., Jenkins, C., Sridharan, V., Tarasov, S.G., Tarasova, N.I., Andresson, T., et al. (2020). Structure of E3 ligase E6AP with a proteasome-binding site provided by substrate receptor hRpn10. Nat. Commun. *11*, 1–15.

Buhr, F., Jha, S., Thommen, M., Mittelstaet, J., Kutz, F., Schwalbe, H., Rodnina, M. V., and Komar, A.A. (2016). Synonymous Codons Direct Cotranslational Folding toward Different Protein Conformations. Mol. Cell *61*, 341–351.

Carrion-Vazquez, M., Li, H., Lu, H., Marszalek, P.E., Oberhauser, A.F., and Fernandez, J.M. (2003). The mechanical stability of ubiquitin is linkage dependent. Nat. Struct. Biol. *10*, 738–743.

Carroll, E.C., Greene, E.R., Martin, A., and Marqusee, S. (2020). Site-specific ubiquitination affects protein energetics and proteasomal degradation. Nat. Chem. Biol.

Carugo, O. (2016). Protein Termini. Curr. Protein Pept. Sci. *18*, 211–216.

Chaney, J.L., Steele, A., Carmichael, R., Rodriguez, A., Specht, A.T., Ngo, K., Li, J., Emrich, S., and Clark, P.L. (2017). Widespread position-specific conservation of synonymous rare codons within coding sequences. PLoS Comput. Biol. *13*, 1–19.

Chao, C.C.K. (2014). Mechanisms of p53 degradation. Clin. Chim. Acta *438*, 139–147.

Chaugule, V.K., and Walden, H. (2016). Specificity and disease in the ubiquitin system. Biochem. Soc. Trans. *44*, 212–227.

Chen, L., and Madura, K. (2002). Rad23 Promotes the Targeting of Proteolytic Substrates to the Proteasome. Mol. Cell. Biol. *22*, 4902–4913.

Chen, C.Y., Chang, Y.C., Lin, B.L., Huang, C.H., and Tsai, M.D. (2019). Temperature-Resolved Cryo-EM Uncovers Structural Bases of Temperature-Dependent Enzyme Functions. J. Am. Chem. Soc. *141*, 19983–19987.

Chen, S., Wu, J., Lu, Y., Ma, Y.B., Lee, B.H., Yu, Z., Ouyang, Q., Finley, D.J., Kirschner, M.W., and Mao, Y. (2016). Structural basis for dynamic regulation of the human 26S proteasome. Proc. Natl. Acad. Sci. U. S. A. *113*, 12991–12996.

Chin, J.W. (2017). Expanding and reprogramming the genetic code. Nature *550*, 53–60.

Chojnacki, M., Mansour, W., Hameed, D.S., Singh, R.K., El Oualid, F., Rosenzweig, R., Nakasone, M.A., Yu, Z., Glaser, F., Kay, L.E., et al. (2017). Polyubiquitin-Photoactivatable Crosslinking Reagents for Mapping Ubiquitin Interactome Identify Rpn1 as a Proteasome Ubiquitin-Associating Subunit. Cell Chem. Biol. *24*.

Christopher, J.A., and Baldwin, T.O. (1996). Implications of N and C-Terminal Proximity for Protein Folding protein structure; minimization. J. Mol. Biol *257*, 175–187.

Cordova, J.C., Olivares, A.O., Shin, Y., Stinson, B.M., Calmat, S., Schmitz, K.R., Aubin-Tam, M.E., Baker, T.A., Lang, M.J., and Sauer, R.T. (2014). Stochastic but highly coordinated protein unfolding and translocation by the ClpXP proteolytic machine. Cell *158*, 647–658.

Cundiff, M.D., Hurley, C.M., Wong, J.D., Boscia, J.A., Bashyal, A., Rosenberg, J., Reichard, E.L., Nassif, N.D., Brodbelt, J.S., and Kraut, D.A. (2019). Ubiquitin receptors are required for substrate-mediated activation of the proteasome's unfolding ability. Sci. Rep. *9*, 1–17.

Dambacher, C.M., Worden, E.J., Herzik, M.A., Martin, A., and Lander, G.C. (2016). Atomic structure of the 26S proteasome lid reveals the mechanism of deubiquitinase inhibition. Elife *5*, 1–17.

Davis, L., and Chin, J.W. (2012). Designer proteins: Applications of genetic code expansion in cell biology. Nat. Rev. Mol. Cell Biol. *13*, 168–182.

Debelouchina, G.T., Gerecht, K., and Muir, T.W. (2017). Ubiquitin utilizes an acidic surface patch to alter chromatin structure. Nat. Chem. Biol. *13*, 105–110.

Ding, Z., Fu, Z., Xu, C., Wang, Y., Wang, Y., Li, J., Kong, L., Chen, J., Li, N., Zhang, R., et al. (2017). High-resolution cryo-EM structure of the proteasome in complex with ADP-AlFx. Cell Res. *27*, 373–385.

Ding, Z., Xu, C., Sahu, I., Wang, Y., Fu, Z., Huang, M., Wong, C.C.L., Glickman, M.H., and Cong, Y. (2019). Structural Snapshots of 26S Proteasome Reveal Tetraubiquitin-Induced Conformations. Mol. Cell *73*.

Dong, Y., Zhang, S., Wu, Z., Li, X., Wang, W.L., Zhu, Y., Stoilova-McPhie, S., Lu, Y., Finley, D., and Mao, Y. (2019). Cryo-EM structures and dynamics of substrate-engaged human 26S proteasome. Nature *565*, 49–55.

Eddins, M.J., Varadan, R., Fushman, D., Pickart, C.M., and Wolberger, C. (2007). Crystal Structure and Solution NMR Studies of Lys48-linked Tetraubiquitin at Neutral pH. J. Mol. Biol. *367*, 204–211.

Eisele, M.R., Reed, R.G., Rudack, T., Schweitzer, A., Beck, F., Nagy, I., Pfeifer, G., Plitzko, J.M., Baumeister, W., Tomko, R.J., et al. (2018). Expanded Coverage of the 26S Proteasome Conformational Landscape Reveals Mechanisms of Peptidase Gating. Cell Rep. *24*, 1301-1315.e5.

Elsasser, S., Chandler-Mitilello, D., Müller, B., Hanna, J., and Finley, D. (2004). Rad23 and Rpn10 serve as alternate ubiquitin receptors for the proteasome. J. Biol. Chem. *279*, 26817–26822.

Elsasser, S., Schmidt, M., and Finley, D. (2005). Characterization of the proteasome using native gel electrophoresis. Methods Enzymol. *398*, 353–363.

Erales, J., Hoyt, M.A., Troll, F., and Coffino, P. (2012). Functional asymmetries of proteasome translocase pore. J. Biol. Chem. *287*, 18535–18543.

Erzberger, J.P., and Berger, J.M. (2006). Evolutionary relationships and structural mechanisms of AAA+ proteins. Annu. Rev. Biophys. Biomol. Struct. *35*, 93–114.

Estrin, E., Lopez-Blanco, J.R., Chacon, P., and Martin, A. (2013). Formation of an intricate helical bundle dictates the assembly of the 26S proteasome lid. Structure *21*, 1624–1635.

Faggiano, S., and Pastore, A. (2014). The Challenge of Producing Ubiquitinated Proteins for Structural Studies. Cells *3*, 639–656.

Fan, C.M., and Maniatis, T. (1991). Generation of p50 subunit of NF-kappa B by processing of p105 through an ATP-dependent pathway. Nature *354*, 395–398.

Fang, N.N., Chan, G.T., Zhu, M., Comyn, S.A., Persaud, A., Deshaies, R.J., Rotin, D., Gsponer, J.,

and Mayor, T. (2014). Rsp5/Nedd4 is the main ubiquitin ligase that targets cytosolic misfolded proteins following heat stress. Nat. Cell Biol. *16*, 1227–1237.

Finley, D., and Prado, M.A. (2020). The proteasome and its network: Engineering for adaptability. Cold Spring Harb. Perspect. Biol. *12*.

Finley, D., Chen, X., and Walters, K.J. (2016). Gates, Channels, and Switches: Elements of the Proteasome Machine. Trends Biochem. Sci. *41*, 77–93.

Da Fonseca, P.C.A., He, J., and Morris, E.P. (2012). Molecular Model of the Human 26S Proteasome. Mol. Cell *46*, 54–66.

Frickey, T., and Lupas, A.N. (2004). Phylogenetic analysis of AAA proteins. J. Struct. Biol. *146*, 2–10.

Funakoshi, M., Tomko, R.J., Kobayashi, H., and Hochstrasser, M. (2009). Multiple Assembly Chaperones Govern Biogenesis of the Proteasome Regulatory Particle Base. Cell *137*, 887–899.

Galzitskaya, O. V., Garbuzynskiy, S.O., Ivankov, D.N., and Finkelstein, A. V. (2003). Chain length is the main determinant of the folding rate for proteins with three-state folding kinetics. Proteins Struct. Funct. Genet. *51*, 162–166.

Garbuzynskiy, S.O., Ivankov, D.N., Bogatyreva, N.S., and Finkelstein, A. V. (2013). Golden triangle for folding rates of globular proteins. Proc. Natl. Acad. Sci. U. S. A. *110*, 147–150.

Gavrilov, Y., Hagai, T., and Levy, Y. (2015). Nonspecific yet decisive: Ubiquitination can affect the native-state dynamics of the modified protein. Protein Sci. *24*, 1580–1592.

Glickman, M.H., Rubin, D.M., Coux, O., Wefes, I., Pfeifer, G., Cjeka, Z., Baumeister, W., Fried, V.A., and Finley, D. (1998a). A subcomplex of the proteasome regulatory particle required for ubiquitin-conjugate degradation and related to the COP9-signalosome and eIF3. Cell *94*, 615–623.

Glickman, M.H., Rubin, D.M., Fried, V.A., and Finley, D. (1998b). The Regulatory Particle of the Saccharomyces cerevisiae Proteasome. Mol. Cell. Biol. *18*, 3149–3162.

Glickman, M.H., Rubin, D.M., Coux, O., Wefes, I., Pfeifer, G., Cjeka, Z., Baumeister, W., Fried, V.A., and Finley, D. (1998c). A subcomplex of the proteasome regulatory particle required for ubiquitin-conjugate degradation and related to the COP9-signalosome and elF3. Cell *94*, 615–623.

Glyakina, A. V., and Galzitskaya, O. V. (2020). How quickly do proteins fold and unfold, and what structural parameters correlate with these values? Biomolecules *10*, 1–14.

Glynn, S.E., Kardon, J.R., Mueller-Cajar, O., and Cho, C. (2020). AAA+ proteins: converging mechanisms, diverging functions. Nat. Struct. Mol. Biol. *27*, 515–518.

Godderz, D., Heinen, C., Marchese, F.P., Kurz, T., Acs, K., and Dantuma, N.P. (2015). Cdc48-independent proteasomal degradation coincides with a reduced need for ubiquitylation. Sci. Rep. *5*, 1–8.

Goldberg, A.L. (2003). Protein degradation and protection against misfolded or damaged proteins. Nature *426*, 895–899.

Goldstein, A.L., and McCusker, J.H. (1999). Three new dominant drug resistance cassettes for gene disruption in Saccharomyces cerevisiae. Yeast *15*, 1541–1553.

Greene, E.R., Goodall, E.A., De La Peña, A.H., Matyskiela, M.E., Lander, G.C., and Martin, A. (2019). Specific lid-base contacts in the 26S proteasome control the conformational switching required for substrate degradation. Elife *8*, 1–27.

Greene, E.R., Dong, K.C., and Martin, A. (2020). Understanding the 26S proteasome molecular machine from a structural and conformational dynamics perspective. Curr. Opin. Struct. Biol. *61*, 33–41.

Groll, M., Ditzel, L., Löwe, J., Stock, D., Bochtler, M., Bartunik, H.D., and Huber, R. (1997). Structure of 20S proteasome from yeast at 2.4 Å resolution. Nature *386*, 463–471.

Groll, M., Bajorek, M., Köhler, A., Moroder, L., Rubin, D.M., Huber, R., Glickman, M.H., and Finley, D. (2000). A gated channel into the proteasome core particle. Nat. Struct. Biol. *7*, 1062–1067.

Gruber, R., Levitt, M., and Horovitz, A. (2017). Sequential allosteric mechanism of ATP hydrolysis by the CCT/TRiC chaperone is revealed through Arrhenius analysis. Proc. Natl. Acad. Sci. U. S. A. *114*, 5189–5194.

Guo, Q., Lehmer, C., Martínez-Sánchez, A., Rudack, T., Beck, F., Hartmann, H., Pérez-Berlanga, M., Frottin, F., Hipp, M.S., Hartl, F.U., et al. (2018). In Situ Structure of Neuronal C9orf72 Poly-GA Aggregates Reveals Proteasome Recruitment. Cell *172*, 696-705.e12.

Hagai, T., and Levy, Y. (2010). Ubiquitin not only serves as a tag but also assists degradation by inducing protein unfolding. Proc. Natl. Acad. Sci. U. S. A. *107*, 2001–2006.

Hagai, T., Azia, A., Tóth-Petróczy, Á., and Levy, Y. (2011). Intrinsic disorder in ubiquitination substrates. J. Mol. Biol. *412*, 319–324.

Haselbach, D., Schrader, J., Lambrecht, F., Henneberg, F., Chari, A., and Stark, H. (2017). Long-range allosteric regulation of the human 26S proteasome by 20S proteasome-targeting cancer drugs. Nat. Commun. *8*, 1–8.

Hersko, A., and Ciechanover, A. (1998). The ubiquitin system. Annu. Rev. Biochem. *67*, 425–479.

Holmberg, C.I., Staniszewski, K.E., Mensah, K.N., Matouschek, A., and Morimoto, R.I. (2004). Inefficient degradation of truncated polyglutamine proteins by the proteasome. EMBO J. *23*, 4307–4318.

Huang, H.T., Dobrovolsky, D., Paulk, J., Yang, G., Weisberg, E.L., Doctor, Z.M., Buckley, D.L., Cho, J.H., Ko, E., Jang, J., et al. (2018). A Chemoproteomic Approach to Query the Degradable Kinome Using a Multi-kinase Degrader. Cell Chem. Biol. *25*, 88-99.e6.

Huang, X., Luan, B., Wu, J., and Shi, Y. (2016). An atomic structure of the human 26S proteasome. Nat. Struct. Mol. Biol. *23*, 778–785.

Husnjak, K., Elsasser, S., Zhang, N., Chen, X., Randles, L., Shi, Y., Hofmann, K., Walters, K.J., Finley, D., and Dikic, I. (2008). Proteasome subunit Rpn13 is a novel ubiquitin receptor. Nature *453*, 481–488.

Iyer, L.M., Leipe, D.D., Koonin, E. V, and Aravind, L. (2004). Evolutionary history and higher order classification of AAA+ ATPases. J Struct Biol *146*, 11–31.

Jacobs, W.M., and Shakhnovich, E.I. (2017). Evidence of evolutionary selection for cotranslational folding. Proc. Natl. Acad. Sci. U. S. A. *114*, 11434–11439.

Kachroo, A.H., Laurent, J.M., Yellman, C.M., Meyer, A.G., Wilke, C.O., and Marcotte, E.M. (2015). Systematic humanization of yeast genes reveals conserved functions and genetic modularity. Science (80-.). *348*, 921–926.

Kamadurai, H.B., Qiu, Y., Deng, A., Harrison, J.S., MacDonald, C., Actis, M., Rodrigues, P., Miller, D.J., Souphron, J., Lewis, S.M., et al. (2013). Mechanism of ubiquitin ligation and lysine prioritization by a HECT E3. Elife *2*, 1–26.

Karczewski, K.J., Francioli, L.C., Tiao, G., Cummings, B.B., Alföldi, J., Wang, Q., Collins, R.L., Laricchia, K.M., Ganna, A., Birnbaum, D.P., et al. (2020). The mutational constraint spectrum quantified from variation in 141,456 humans. Nature *581*, 434–443.

Kardon, J.R., Moroco, J.A., Engen, J.R., and Baker, T.A. (2020). Mitochondrial clpx activates an essential biosynthetic enzyme through partial unfolding. Elife *9*, 1–20.

Karin, M., and Ben-Neriah, Y. (2000). Phosphorylation meets ubiquitination: the control of NF-[kappa]B activity. Annu Rev Immunol *18*, 621–663.

Kenniston, J.A., Burton, R.E., Siddiqui, S.M., Baker, T.A., and Sauer, R.T. (2004). Effects of local protein stability and the geometric position of the substrate degradation tag on the efficiency of ClpXP denaturation and degradation. J. Struct. Biol. *146*, 130–140.

Khurana, R., Hate, A.T., Nath, U., and Udgaonkar, J. (1995). pH dependence of the stability of barstar to chemical and thermal denaturation. Protein Sci. *4*, 1133–1144.

Kim, H.C., Steffen, A.M., Oldham, M.L., Chen, J., and Huibregtse, J.M. (2011). Structure and function of a HECT domain ubiquitin-binding site. EMBO Rep. *12*, 334–341.

Kim, I., Mi, K., and Rao, H. (2004). Multiple Interactions of Rad23 Suggest a Mechanism for Ubiquitylated Substrate Delivery Important in Proteolysis. Mol. Biol. Cell *15*, 3357–3365.

Kolygo, K., Ranjan, N., Kress, W., Striebel, F., Hollenstein, K., Neelsen, K., Steiner, M., Summer, H., and Weber-Ban, E. (2009). Studying chaperone-proteases using a real-time approach based on FRET. J. Struct. Biol. *168*, 267–277.

Komander, D., and Rape, M. (2012). The Ubiquitin Code. Annu. Rev. Biochem. *81*, 203–229.

Komar, A.A. (2019). Synonymous Codon Usage—a Guide for Co-Translational Protein Folding in the Cell. Mol. Biol. *53*, 777–790.

Koodithangal, P., Jaffe, N.E., Kraut, D.A., Fishbain, S., Herman, C., and Matouschek, A. (2009). ATP-dependent proteases differ substantially in their ability to unfold globular proteins. J. Biol. Chem. *284*, 18674–18684.

Kraut, D.A., Israeli, E., Schrader, E.K., Patil, A., Nakai, K., Nanavati, D., Inobe, T., and Matouschek, A. (2012). Sequence- and species-dependence of proteasomal processivity. ACS Chem. Biol. *7*, 1444–1453.

Krishna, M.M.G., and Englander, S.W. (2005). The N-terminal to C-terminal motif in protein folding and function. Proc. Natl. Acad. Sci. U. S. A. *102*, 1053–1058.

De la Peña, A.H., Goodall, E.A., Gates, S.N., Lander, G.C., and Martin, A. (2018). Substrate-engaged 26S proteasome structures reveal mechanisms for ATP-hydrolysis–driven translocation. Science (80-.). *362*.

Lander, G.C., Estrin, E., Matyskiela, M.E., Bashore, C., Nogales, E., and Martin, A. (2012). Complete subunit architecture of the proteasome regulatory particle. Nature *482*, 186–191.

Lasker, K., Förster, F., Bohn, S., Walzthoeni, T., Villa, E., Unverdorben, P., Beck, F., Aebersold, R., Sali, A., and Baumeister, W. (2012). Molecular architecture of the 26S proteasome holocomplex determined by an integrative approach. Proc. Natl. Acad. Sci. U. S. A. *109*, 1380–1387.

Lee, C., Schwartz, M.P., Prakash, S., Iwakura, M., and Matouschek, A. (2001). ATP-dependent proteases degrade their substrates by processively unraveling them from the degradation signal. Mol. Cell *7*, 627–637.

Lee, Y.T.C., Chang, C.Y., Chen, S.Y., Pan, Y.R., Ho, M.R., and Hsu, S.T.D. (2017). Entropic stabilization of a deubiquitinase provides conformational plasticity and slow unfolding kinetics beneficial for functioning on the proteasome. Sci. Rep. *7*, 1–14.

Liu, T., Whitten, S.T., and Hilser, V.J. (2006). Ensemble-based signatures of energy propagation in proteins: A new view of an old phenomenon. Proteins Struct. Funct. Genet. *62*, 728–738.

Liutkute, M., Samatova, E., and Rodnina, M. V. (2020). Cotranslational folding of proteins on the ribosome. Biomolecules *10*.

Livneh, I., Kravtsova-Ivantsiv, Y., Braten, O., Kwon, Y.T., and Ciechanover, A. (2017). Monoubiquitination joins polyubiquitination as an esteemed proteasomal targeting signal. BioEssays *39*, 1–7.

Longtine, M.S., McKenzie, A., Demarini, D.J., Shah, N.G., Wach, A., Brachat, A., Philippsen, P., and Pringle, J.R. (1998). Additional modules for versatile and economical PCR-based gene deletion and modification in Saccharomyces cerevisiae. Yeast *14*, 953–961.

Lu, Y., Lee, B.H., King, R.W., Finley, D., and Kirschner, M.W. (2015). Substrate degradation by the proteasome: A single-molecule kinetic analysis. Science (80-.). *348*, 183–184.

Lu, Y., Wu, J., Dong, Y., Chen, S., Sun, S., Ma, Y.B., Ouyang, Q., Finley, D., Kirschner, M.W., and Mao, Y. (2017). Conformational Landscape of the p28-Bound Human Proteasome Regulatory Particle. Mol. Cell *67*, 322-333.e6.

Luan, B., Huang, X., Wu, J., Mei, Z., Wang, Y., Xue, X., Yan, C., Wang, J., J. Finley, D., Shi, Y., et al. (2016). Structure of an endogenous yeast 26S proteasome reveals two major conformational states. Proc. Natl. Acad. Sci. U. S. A. *113*, 2642–2647.

Maki, C.G., Huibregtse, J.M., and Howley, P.M. (1996). In vivo ubiquitination and proteasome-mediated degradation of p53. Cancer Res. *56*, 2649–2654.

Mallik, S., and Kundu, S. (2018). Topology and Oligomerization of Mono- and Oligomeric Proteins Regulate Their Half-Lives in the Cell. Structure *26*, 869-878.e3.

Martin, A., Baker, T.A., and Sauer, R.T. (2008). Protein unfolding by a AAA+ protease is dependent on ATP-hydrolysis rates and substrate energy landscapes. Nat. Struct. Mol. Biol. *15*, 139–145.

Martin, J.L., Ishmukhametov, R., Spetzler, D., Hornung, T., and Frasch, W.D. (2018). Elastic coupling power stroke mechanism of the F1-ATPase molecular motor. Proc. Natl. Acad. Sci. U. S. A. *115*, 5750–5755.

Martín, Á.S., Rodriguez-Aliaga, P., Molina, J.A., Martin, A., Bustamante, C., and Baez, M. (2017). Knots can impair protein degradation by ATP-dependent proteases. Proc. Natl. Acad. Sci. U. S. A. *114*, 9864–9869.

Martinez-Fonts, K., Davis, C., Tomita, T., Elsasser, S., Nager, A.R., Shi, Y., Finley, D., and Matouschek, A. (2020). The proteasome 19S cap and its ubiquitin receptors provide a versatile recognition platform for substrates. Nat. Commun. *11*.

Matyskiela, M.E., Lander, G.C., and Martin, A. (2013). Conformational switching of the 26S proteasome enables substrate degradation. Nat. Struct. Mol. Biol. *20*, 781–788.

Moran, U., Phillips, R., and Milo, R. (2010). SnapShot: Key numbers in biology. Cell *141*, 1–2.

Morimoto, D., Walinda, E., Fukada, H., Sou, Y.S., Kageyama, S., Hoshino, M., Fujii, T., Tsuchiya, H., Saeki, Y., Arita, K., et al. (2015). The unexpected role of polyubiquitin chains in the formation of fibrillar aggregates. Nat. Commun. *6*, 1–3.

Morimoto, D., Walinda, E., Fukada, H., Sugase, K., and Shirakawa, M. (2016). Ubiquitylation Directly Induces Fold Destabilization of Proteins. Sci. Rep. *6*, 1–9.

Murata, S., Yashiroda, H., and Tanaka, K. (2009). Molecular mechanisms of proteasome assembly. Nat. Rev. Mol. Cell Biol. *10*, 104–115.

Myers, J.K., Nick Pace, C., and Martin Scholtz, J. (1995). Denaturant m values and heat capacity changes: Relation to changes in accessible surface areas of protein unfolding. Protein Sci. *4*, 2138–2148.

Myers, N., Olender, T., Savidor, A., Levin, Y., Reuven, N., and Shaul, Y. (2018). The Disordered Landscape of the 20S Proteasome Substrates Reveals Tight Association with Phase Separated Granules. Proteomics *18*, 1–9.

Nager, A.R., Baker, T.A., and Sauer, R.T. (2011). Stepwise unfolding of a β barrel protein by the AAA+ ClpXP protease. J. Mol. Biol. *413*, 4–16.

Nemec, A.A., Peterson, A.K., Warnock, J.L., Reed, R.G., and Tomko, R.J. (2019). An Allosteric Interaction Network Promotes Conformation State-Dependent Eviction of the Nas6 Assembly Chaperone from Nascent 26S Proteasomes. Cell Rep. *26*, 483-495.e5.

Nguyen, A.T., Prado, M.A., Schmidt, P.J., Sendamarai, A.K., Wilson-Grady, J.T., Min, M., Campagna, D.R., Tian, G., Shi, Y., Dederer, V., et al. (2017). UBE2O remodels the proteome during terminal erythroid differentiation. Science (80-.). *357*.

Nölting, B., Golbik, R., Neira, J.L., Soler-Gonzalez, A.S., Schreiber, G., and Fersht, A.R. (1997). The folding pathway of a protein at high resolution from microseconds to seconds. Proc. Natl. Acad. Sci. U. S. A. *94*, 826–830.

Nowak, R.P., Deangelo, S.L., Buckley, D., He, Z., Donovan, K.A., An, J., Safaee, N., Jedrychowski, M.P., Ponthier, C.M., Ishoey, M., et al. (2018). Plasticity in binding confers selectivity in ligand-induced protein degradation article. Nat. Chem. Biol. *14*, 706–714.

Oh, E., Akopian, D., and Rape, M. (2018). Principles of Ubiquitin- Dependent Signaling. Annu. Rev. Cell Dev. Biol. *34*, 137–162.

Olivares, A.O., Baker, T.A., and Sauer, R.T. (2018). Mechanical Protein Unfolding and Degradation. Annu. Rev. Physiol. *80*, 413–429.

Olszewski, M.M., Williams, C., Dong, K.C., and Martin, A. (2019). The Cdc48 unfoldase prepares well-folded protein substrates for degradation by the 26S proteasome. Commun. Biol. *2*.

Opoku-Nsiah, K.A., and Gestwicki, J.E. (2018). Aim for the Core:Suitability of the ubiquitin-independent 20S proteasome as a drug target in neurodegeneration. Transl. Resour. *198*, 48–57.

Orian, A., Schwartz, A.L., Israel, A., Whiteside, S., Kahana, C., and Ciechanover, A. (1999). Structural motifs involved in ubiquitin-mediated processing of the NF-kappaB precursor p105: roles of the glycine-rich region and a downstream ubiquitination domain. Mol Cell Biol *19*, 3664–3673.

Orlowski, M., and Wilk, S. (2000). Catalytic activities of the 20 S proteasome, a multicatalytic proteinase complex. Arch. Biochem. Biophys. *383*, 1–16.

Ovchinnikov, S., Kamisetty, H., and Baker, D. (2014). Robust and accurate prediction of residue-residue interactions across protein interfaces using evolutionary information. Elife *2014*, 1–21.

Palombella, V.J., Rando, O.J., Goldberg, A.L., and Maniatis, T. (1994). The ubiquitin-proteasome pathway is required for processing the NF-kappa B1 precursor protein and the activation of NF-kappa B. Cell *78*, 773–785.

Park, C. (2014). Probing transient partial unfolding in proteins by native-state proteolysis. Biodesign *2*, 117–128.

Park, C., and Marqusee, S. (2004). Probing the high energy states in proteins by proteolysis. J. Mol. Biol. *343*, 1467–1476.

Peth, A., Kukushkin, N., Bossé, M., and Goldberg, A.L. (2013). Ubiquitinated proteins activate the proteasomal ATPases by binding to Usp14 or Uch37 homologs. J. Biol. Chem. *288*, 7781–7790.

Piwko, W., and Jentsch, S. (2006). Proteasome-mediated protein processing by bidirectional degradation initiated from an internal site. Nat. Struct. Mol. Biol. *13*, 691–697.

Prakash, S., Tian, L., Ratliff, K.S., Lehotzky, R.E., and Matouschek, A. (2004). An unstructured initiation site is required for efficient proteasome-mediated degradation. Nat. Struct. Mol. Biol. *11*, 830–837.

Rabl, J., Smith, D.M., Yu, Y., Chang, S.C., Goldberg, A.L., and Cheng, Y. (2008). Mechanism of Gate Opening in the 20S Proteasome by the Proteasomal ATPases. Mol. Cell *30*, 360–368.

Raschke, T.M., Kho, J., and Marqusee, S. (1999). Confirmation of the hierarchical folding of RNase H: A protein engineering study. Nat. Struct. Biol. *6*, 825–830.

Reichard, E.L., Chirico, G.G., Dewey, W.J., Nassif, N.D., Bard, K.E., Millas, N.E., and Kraut, X.D.A. (2016). Substrate ubiquitination controls the unfolding ability of the proteasome. J. Biol. Chem. *291*, 18547–18561.

Rennie, M.L., Chaugule, V.K., and Walden, H. (2020). Modes of allosteric regulation of the ubiquitination machinery. Curr. Opin. Struct. Biol. *62*, 189–196.

Rodnina, M. V. (2016). The ribosome in action: Tuning of translational efficiency and protein folding. Protein Sci. *25*, 1390–1406.

Roy, R., Hohng, S., and Ha, T. (2008). A practical guide to single-molecule FRET. Nat. Methods *5*, 507–516.

Rubin, D.M., Glickman, M.H., Larsen, C.N., Dhruvakumar, S., and Finley, D. (1998). Active site mutants in the six regulatory particle ATPases reveal multiple roles for ATP in the proteasome. EMBO J. *17*, 4909–4919.

Saeki, Y., and Tanaka, K. (2012). Assembly and function of the proteasome. Methods Mol Biol *832*, 315–337.

Saeki, Y., Isono, E., and Toh, E.A. (2005). Preparation of ubiquitinated substrates by the PY motif-insertion method for monitoring 26S proteasome activity. Methods Enzym. *399*, 215–227.

Sakamoto, K.M., Kim, K.B., Kumagai, A., Mercurio, F., Crews, C.M., and Deshaies, R.J. (2001). Protacs: Chimeric molecules that target proteins to the Skp1-Cullin-F box complex for ubiquitination and degradation. Proc. Natl. Acad. Sci. U. S. A. *98*, 8554–8559.

Sala, A.J., Bott, L.C., and Morimoto, R.I. (2017). Shaping proteostasis at the cellular, tissue, and organismal level. J. Cell Biol. *216*, 1231–1241.

Schauber, C., Chen, L., Tongaonkar, P., Vega, I., Lambertson, D., Potts, W., and Madura, K. (1998). Rad23 links DNA repair to the ubiquitin/proteasome pathway. Nature *391*, 715–718.

Schrader, E.K., Harstad, K.G., Holmgren, R.A., and Matouschek, A. (2011). A Three-part signal governs differential processing of Gli1 and Gli3 proteins by the proteasome. J. Biol. Chem. *286*, 39051–39058.

Schweitzer, A., Aufderheide, A., Rudack, T., Beck, F., Pfeifer, G., Plitzko, J.M., Sakata, E., Schulten, K., Förster, F., and Baumeister, W. (2016). Structure of the human 26S proteasome at a resolution of 3.9 Å. Proc. Natl. Acad. Sci. U. S. A. *113*, 7816–7821.

Sen, M., Maillard, R.A., Nyquist, K., Rodriguez-Aliaga, P., Pressé, S., Martin, A., and Bustamante, C. (2013). XThe ClpXP protease unfolds substrates using a constant rate of pulling but different gears. Cell *155*, 636.

Sharma, A.K., and O'Brien, E.P. (2018). Non-equilibrium coupling of protein structure and function to translation–elongation kinetics. Curr. Opin. Struct. Biol. *49*, 94–103.

Shi, Y., Chen, X., Elsasser, S., Stocks, B.B., Tian, G., Lee, B.H., Shi, Y., Zhang, N., De Poot, S.A.H., Tuebing, F., et al. (2016). Rpn1 provides adjacent receptor sites for substrate binding and deubiquitination by the proteasome. Science (80-.). *351*.

Sivertsson, E.M., Jackson, S.E., and Itzhaki, L.S. (2019). The AAA+ protease ClpXP can easily degrade a 3 1 and a 5 2 -knotted protein. Sci. Rep. *9*, 1–14.

Śledź, P., Unverdorben, P., Beck, F., Pfeifer, G., Schweitzer, A., Förster, F., and Baumeister, W. (2013). Structure of the 26S proteasome with ATP-γS bound provides insights into the mechanism of nucleotide-dependent substrate translocation. Proc. Natl. Acad. Sci. U. S. A. *110*, 7264–7269.

Smith, B.E., Wang, S.L., Jaime-Figueroa, S., Harbin, A., Wang, J., Hamman, B.D., and Crews, C.M. (2019). Differential PROTAC substrate specificity dictated by orientation of recruited E3 ligase. Nat. Commun. *10*, 1–13.

Smith, D.M., Chang, S.C., Park, S., Finley, D., Cheng, Y., and Goldberg, A.L. (2007). Docking of the Proteasomal ATPases' Carboxyl Termini in the 20S Proteasome's α Ring Opens the Gate for Substrate Entry. Mol. Cell *27*, 731–744.

Sone, T., Saeki, Y., Toh-E, A., and Yokosawa, H. (2004). Sem1p Is a novel subunit of the 26 S proteasome from Saccharomyces cerevisiae. J. Biol. Chem. *279*, 28807–28816.

Sonnhammer, E.L.L., and Östlund, G. (2015). InParanoid 8: Orthology analysis between 273 proteomes, mostly eukaryotic. Nucleic Acids Res. *43*, D234–D239.

Sousa, R., and Lafer, E.M. (2019). The physics of entropic pulling: A novel model for the Hsp70 motor mechanism. Int. J. Mol. Sci. *20*.

Sriramoju, M.K., Chen, Y., Lee, Y.T.C., and Hsu, S.T.D. (2018). Topologically knotted deubiquitinases exhibit unprecedented mechanostability to withstand the proteolysis by an AAA+ protease. Sci. Rep. *8*, 1–9.

Sriramoju, M.K., Chen, Y., and Hsu, S.T.D. (2020). Protein knots provide mechano-resilience to an AAA+ protease-mediated proteolysis with profound ATP energy expenses. Biochim. Biophys. Acta - Proteins Proteomics *1868*, 140330.

Stein, K.C., and Frydman, J. (2019). The stop-and-go traffic regulating protein biogenesis: How translation kinetics controls proteostasis. J. Biol. Chem. *294*, 2076–2084.

Swatek, K.N., and Komander, D. (2016). Ubiquitin modifications. Cell Res. *26*, 399–422.

Takeuchi, J., Chen, H., and Coffino, P. (2007). Proteasome substrate degradation requires association plus extended peptide. EMBO J. *26*, 123–131.

Tate, J.G., Bamford, S., Jubb, H.C., Sondka, Z., Beare, D.M., Bindal, N., Boutselakis, H., Cole, C.G., Creatore, C., Dawson, E., et al. (2019). COSMIC: The Catalogue Of Somatic Mutations In Cancer. Nucleic Acids Res. *47*, D941–D947.

Theile, C.S., Witte, M.D., Blom, A.E.M., Kundrat, L., Ploegh, H.L., and Guimaraes, C.P. (2013). Site-specific N-terminal labeling of proteins using sortase-mediated reactions. Nat. Protoc. *8*, 1800–1807.

Tian, G., Park, S., Lee, M.J., Huck, B., McAllister, F., Hill, C.P., Gygi, S.P., and Finley, D. (2011). An asymmetric interface between the regulatory and core particles of the proteasome. Nat. Struct. Mol. Biol. *18*, 1259–1267.

Tian, L., Holmgren, R.A., and Matouschek, A. (2005). A conserved processing mechanism regulates the activity of transcription factors Cubitus interruptus and NF-𝜘B. Nat. Struct. Mol. Biol. *12*, 1045–1053.

Tomita, T., and Matouschek, A. (2019). Substrate selection by the proteasome through initiation regions. Protein Sci. *28*.

Tomko, R.J., and Hochstrasser, M. (2011). Order of the Proteasomal ATPases and Eukaryotic Proteasome Assembly. Cell Biochem. Biophys. *60*, 13–20.

Tomko, R.J., Funakoshi, M., Schneider, K., Wang, J., and Hochstrasser, M. (2010). Heterohexameric Ring Arrangement of the Eukaryotic Proteasomal ATPases: Implications for Proteasome Structure and Assembly. Mol. Cell *38*, 393–403.

Tomko, R.J., Taylor, D.W., Chen, Z.A., Wang, H.W., Rappsilber, J., and Hochstrasser, M. (2015). A Single α Helix Drives Extensive Remodeling of the Proteasome Lid and Completion of Regulatory Particle Assembly. Cell *163*, 432–444.

Tomko Jr., R.J., and Hochstrasser, M. (2011). Incorporation of the Rpn12 subunit couples completion of proteasome regulatory particle lid assembly to lid-base joining. Mol Cell *44*, 907–917.

Toste Rêgo, A., and da Fonseca, P.C.A. (2019). Characterization of Fully Recombinant Human 20S and 20S-PA200 Proteasome Complexes. Mol. Cell *76*, 138-147.e5.

Tsuchiya, H., Ohtake, F., Arai, N., Kaiho, A., Yasuda, S., Tanaka, K., and Saeki, Y. (2017). In Vivo Ubiquitin Linkage-type Analysis Reveals that the Cdc48-Rad23/Dsk2 Axis Contributes to K48-Linked Chain Specificity of the Proteasome. Mol. Cell *66*, 488-502.e7.

Twomey, E.C., Ji, Z., Wales, T.E., Bodnar, N.O., Ficarro, S.B., Marto, J.A., Engen, J.R., and Rapoport, T.A. (2019). Substrate processing by the Cdc48 ATPase complex is initiated by ubiquitin

unfolding. Science (80-.). *365*, 502–513.

Unverdorben, P., Beck, F., Sledz, P., Schweitzer, A., Pfeifer, G., Plitzko, J.M., Baumeister, W., and Förster, F. (2014). Deep classification of a large cryo-EM dataset defines the conformational landscape of the 26S proteasome. Proc. Natl. Acad. Sci. U. S. A. *111*, 5544–5549.

Varadan, R., Walker, O., Pickart, C., and Fushman, D. (2002). Structural properties of polyubiquitin chains in solution. J. Mol. Biol. *324*, 637–647.

Verma, R., Aravind, L., Oania, R., McDonald, W.H., Yates, J.R., Koonin, E. V., and Deshaies, R.J. (2002). Role of Rpn11 metalloprotease in deubiquitination and degradation by the 26S proteasome. Science (80-.). *298*, 611–615.

VerPlank, J.J.S., and Goldberg, A.L. (2017). Regulating protein breakdown through proteasome phosphorylation. Biochem. J. *474*, 3355–3371.

VerPlank, J.J.S., Lokireddy, S., Zhao, J., and Goldberg, A.L. (2019). 26S Proteasomes are rapidly activated by diverse hormones and physiological states that raise cAMP and cause Rpn6 phosphorylation. Proc. Natl. Acad. Sci. U. S. A. *116*, 4228–4237.

Volker, C., and Lupas, A.N. (2002). Molecular evolution of proteasomes. Curr. Top. Microbiol. Immunol. *268*, 1–22.

Walker, E.J., Bettinger, J.Q., Welle, K.A., Hryhorenko, J.R., and Ghaemmaghami, S. (2019). Global analysis of methionine oxidation provides a census of folding stabilities for the human proteome. Proc. Natl. Acad. Sci. U. S. A. *116*, 6081–6090.

Walsh, I.M., Bowman, M.A., Soto Santarriaga, I.F., Rodriguez, A., and Clark, P.L. (2020). Synonymous codon substitutions perturb cotranslational protein folding in vivo and impair cell fitness. Proc. Natl. Acad. Sci. U. S. A. *117*, 3528–3534.

Waudby, C.A., Dobson, C.M., and Christodoulou, J. (2019). Nature and Regulation of Protein Folding on the Ribosome. Trends Biochem. Sci. *44*, 914–926.

Wehmer, M., Rudack, T., Beck, F., Aufderheide, A., Pfeifer, G., Plitzko, J.M., Förster, F., Schulten, K., Baumeister, W., and Sakata, E. (2017). Structural insights into the functional cycle of the ATPase module of the 26S proteasome. Proc. Natl. Acad. Sci. U. S. A. *114*, 1305–1310.

Wendler, P., Ciniawsky, S., Kock, M., and Kube, S. (2012). Structure and function of the AAA+ nucleotide binding pocket. Biochim. Biophys. Acta - Mol. Cell Res. *1823*, 2–14.

Wenzel, T., and Baumesiter, W. (1995). Conformational constraints in protein degradation by the 20S proteasome. Nat. Struct. Biol. *2*, 199–204.

Worden, E.J., Padovani, C., and Martin, A. (2014). Structure of the Rpn11-Rpn8 dimer reveals mechanisms of substrate deubiquitination during proteasomal degradation. Nat. Struct. Mol. Biol. *21*, 220–227.

Worden, E.J., Dong, K.C., and Martin, A. (2017). An AAA Motor-Driven Mechanical Switch in Rpn11 Controls Deubiquitination at the 26S Proteasome. Mol. Cell *67*, 799-811.e8.

Xin, F., and Radivojac, P. (2012). Post-translational modifications induce significant yet not extreme changes to protein structure. Bioinformatics *28*, 2905–2913.

Yao, T., and Cohen, R.E. (2002). A cryptic protease couples deubiquitination and degradation by the proteasome. Nature 419, 403–407. Molecular. Nature *419*, 406–407.

Yau, R.G., Doerner, K., Castellanos, E.R., Haakonsen, D.L., Werner, A., Wang, N., Yang, X.W., Martinez-Martin, N., Matsumoto, M.L., Dixit, V.M., et al. (2017). Assembly and Function of Heterotypic Ubiquitin Chains in Cell-Cycle and Protein Quality Control. Cell *171*, 918-933.e20.

Young, D.D., and Schultz, P.G. (2018). Playing with the Molecules of Life. ACS Chem. Biol. *13*, 854–870.

Yu, H., and Matouschek, A. (2017). Recognition of Client Proteins by the Proteasome. Annu. Rev. Biophys. *46*, 149–173.

Zaidi, F.N., Nath, U., and Udgaonkar, J. (1997). Multiple intermediates and transition states during protein unfolding. Nat. Struct. Biol. *4*, 1016–1024.

Zhou, J., Xu, Y., Lin, S., Guo, Y., Deng, W., Zhang, Y., Guo, A., and Xue, Y. (2018). IUUCD 2.0: An update with rich annotations for ubiquitin and ubiquitin-like conjugations. Nucleic Acids Res. *46*, D447–D453.

Zhu, Y., Wang, W.L., Yu, D., Ouyang, Q., Lu, Y., and Mao, Y. (2018). Structural mechanism for nucleotide-driven remodeling of the AAA-ATPase unfoldase in the activated human 26S proteasome. Nat. Commun. *9*, 1–12.